STUDY OF RBC SHAPE TRANSITIONS INDUCED BY NANOPARTICLES

André Eduardo Carneiro Dias

UNIVERSITAT ROVIRA i VIRGILI

Study of RBC shape transitions induced by nanoparticles

André Eduardo Carneiro Dias

DOCTORAL THESIS
2019

UNIVERSITAT ROVIRA I VIRGILI
STUDY OF RBC SHAPE TRANSITIONS INDUCED BY NANOPARTICLES
André Eduardo Carneiro Dias

André Eduardo Carneiro Dias

Study of RBC shape transitions induced by nanoparticles

Doctoral Thesis

Supervised by Dr. Vladimir A. Baulin

Departament d'Enginyeria Química

Molecular Simulation Group

UNIVERSITAT
ROVIRA i VIRGILI

Tarragona, 2019

i

UNIVERSITAT ROVIRA i VIRGILI

Departament d'Enginyeria Química

Av. Països Catalans, 26
43007 Tarragona
Tel.: +34 977 55 8675
Fax.: +34 977 55 9621

I STATE that the present study, entitled "Study of RBC shape transitions induced by nanoparticles", presented by André Eduardo Carneiro Dias for the award of the degree of Doctor, has been carried out under my supervision at the Department d'Enginyeria Química of this university.

Tarragona, April 08, 2019

Doctoral Thesis Supervisor/s

Dr. Vladimir A. Baulin

Acknowledgments

First of all, I would like to thank my supervisor, Dr. Vladimir A. Baulin, for giving me a chance to complete my Ph.D. in his group, and the FP7-funded ITN-SNAL, which I have been a part of as an Early Stage Researcher and which has funded my Ph.D. I have learnt a lot in this process, which would not be possible other wise.

I would also like to thank Dr. Kevin Ward, from BPS, and Dr. Jean-Baptiste Fleury, from Saarlandes University, both who I collaborated with during this Ph.D. in a very fruitful manner. I hope to continue working with you.

Next, I would like to thank my co-workers, Anna, Adrien and Berardo for the interesting discussions, the coffee breaks, and their friendship. I have learnt a lot from you and each has contributed one way or another towards the outcome of this Ph.D.

Finally, I would like to thank my family for all the support I could require even when things seemed darker. I would especially like to thank my father, who was an unbreakable pillar at all times. You were there for me when this journey began. You were there when I needed you the most, and, even now, I know you are still supporting me no matter what, even if I cannot reach you. This thesis is dedicated to you, know that you will always be in my heart.

Summary

This thesis describes the study of the properties of extracellular medium on the cryopreservation of red blood cells and the potential application of silica nanoparticles as co-agents for the intracellular delivery of trehalose, a natural cryoprotectant. The first part of the study focused on the freezing and thawing conditions, and on the properties of the extracellular medium for freezing. Different properties were analysed according to their influence on the survival rate of red blood cells as assessed by hemolysis assay and the effect of freezing was analysed by morphological analysis of images of red blood cells. The second part of the study investigates the interaction of differently charged silica nanoparticles with red blood cells for future application as co-agent for trehalose delivery. Silica nanoparticle toxicity was determined by hemolysis assay and their spatial distribution was studied by imaging freely floating red blood cells using laser scanning confocal microscopy (LSCM). A novel high-throughput 3D visualization method was developed and applied to LSCM images in order to correct the drift throughout the z-stack allowing the analysis of the images. Results were confirmed by interacting the silica nanoparticles with giant unilamellar vesicles (GUV) as an experimental model system.

Contents

1. Introduction

## 1.1.	Historical background

In the past centuries, Medicine has made significant progress towards understanding our circulatory system. William Harvey demonstrated how the circulatory system works back in the 16th century[1]. After that, scientist became interested in blood transfusion. In the 1660's, Richard Lower[2] performed the first transfusion between two dogs, and then went on to pioneer new devices for transfusions, much like modern syringes and catheters. Animal blood was also attempted to be transfused into humans. However, and despite some initial evidence of patients surviving the procedure[3] (likely due to small volumes of blood transfused, allowing the patients to overcome the allergic reaction), these commonly resulted in the patient's death.

It was in 1818, that Dr. James Blundell successfully performed the first human-to-human blood transfusion to treat post-partum hemorrhage[4]. Blundell used a syringe to extract blood from the patient's husband and transfuse it into his wife. He then went on to continue the practice and develop new instruments for blood transfusion. Still, early blood transfusions were regarded as a risky and dubious practice. It was not until the 20th century, that Karl Landsteiner made significant advances in the field with the discovery that when incompatible blood types are mixed an immune response is triggered, causing red blood cells (RBC's) to clot[5]. His work laid the foundation of the ABO blood groups and much safer transfusions.

The discovery that addition of anticoagulants, and refrigeration of the blood allowed for it to be kept for longer periods opened the way to the development of blood banks, while the First World War acted as a catalyst[6]. Oswald Hope Robertson established the precursors for blood banks in preparation for the Third battle of Ypres. Sodium citrate was used as an anticoagulant and blood was stored at casualty clearing stations to allow treatment of injured soldiers[7]. In 1943, acid-citrate-dextrose solution was proposed as a preservative solution allowing for storage up to three weeks[6]. Phosphate was later introduced, in 1957, further increasing shelf life up to four weeks[8],. After that, in 1979, citrate phosphate dextrose adenine (CPDA-1 and CPDA-2) were licensed, improving storage conditions, and allowing an increase in the blood supply and facilitating sharing between different facilities[6].

In the 1950s, Carl Walter and W.P. Murphy proposed the use of plastic bags for blood collection[6,9]. The use of a close system allowed reducing bacterial contamination and air exposure, reducing the weight, improving shock resistance and ease of storage.

By 1940, blood fractionation techniques were starting to develop. At the onset of World War II, liquid plasma was required in Britain. As a way of transporting it from New York, a dried plasma package was developed[10]. This package contained two bottles, one with distilled water to reconstitute the dry plasma. Plasma could be used up to 4 hours after reconstitution.

Separation of the different blood components became more relevant as different components can be applied separately and can be stored under optimized conditions. The first additive solution developed for red blood cell (RBC) concentrates was sodium-adenine-glucose (SAG)[11]. Later, in order to reduce end-storage haemolysis, mannitol was also added (becoming SAGM). At present, RBC concentrates can be stored up to 42-49 days at 4°C. However, and despite the fact that aged RBC's do not show increase of toxicity in transfusions[12], at end-storage, they exhibit alterations of protein activity and even of morphologic properties[13,14].

Despite the advances performed in the last century, the limited shelf time of refrigerated RBC concentrates hampers their distribution in the event of a shortage of blood. Also, it is not uncommon for blood banks to run short of rarer blood types[15]. Improving storage conditions is still in high demand.

Early attempts at freezing mammalian cells date back to the 19th century[15], but it was not until the discovery of the protective action of glycerol, in 1949, that cryopreservation techniques started to be developed[16]. Upon addition of glycerol, it is internalized by the cells, preventing shrinkage and keeping cell structure. Soon after, in 1950, the successful cryopreservation of RBC's in glycerol was reported[16,17], followed by the successful transfusion of frozen RBC's[18]. However, the high concentrations of glycerol that are required for efficient cryoprotection can also cause osmotic lysis upon transfusion. As such, it must be removed after thawing. process which can be damaging for the cells[15].

In 1984, Fahy suggested very rapid cooling, termed vitrification as a method to avoid ice formation[19]. However, due to scaling issues, this approach has been less applicable. Freezing at -80 °C in high glycerol concentration became the standard approach due to the development of mechanical freezers and semi-automatic cell washers. At present, frozen RBC products rely on glycerol as a cryoprotectant and are approved for use up to 10 years of storage, although this is only an administrative limit[15].

Other cryoprotectants have also been attempted. Dimethylsulfoxide (DMSO) is a highly used cryoprotectant in cell biology[20],however it is also a highly toxic component, yielding worse results than glycerol when applied in humans. A natural cryoprotectant in plants, trehalose, has also been proposed as an efficient cryoprotectant[21-23] , but its scarcity made it not a viable alternative until the 21st century when it became possible to synthetize it at an industrial scale.

1.2. Cryopreservation of RBC's

The freezing of RBC's aims at surpassing the shelf life limitation of standard refrigerated RBCs as well as storage lesions occurring due to age. Nonetheless, the freezing step by itself is quite harmful for the cells.

The formation of intracellular ice crystals is the primary source of damage during the freezing step. Furthermore, as water is removed from solution under the form of ice, it causes significant osmotic changes leading to cell dehydration and affecting both the intracellular compartment and the membrane[24]. Studies performed in liposomes have shown that depending on the membrane composition, different consequences can arise, including vesicle and micelle formation[25].

Extra- and intracellular medium freeze at approximately -20 °C and -45°C due to high salt content. Fast cooling rates (e.g. immersion in liquid nitrogen) are usually associated with the formation of intracellular ice crystals. On the other hand, slower cooling rates allows extracellular ice crystals to grow, causing an increasing concentration of solutes in the extracellular medium, which in turns leads to water loss via osmosis[24].

One of the most used cryoprotectant is glycerol. It acts by entering the cell, preventing shrinkage and protecting its structure throughout the freezing process[24]. Two main cryopreservation strategies have been approved: slow freezing using high concentrations of glycerol, and fast freezing using low concentrations of glycerol[15,24]. Still, as mentioned before, the presence of glycerol may cause an osmotic lysis upon transfusion, requiring it to be removed using specific equipment, increasing the processing time of the samples and not enabling their use in poorly equipped facilities, such as in 3rd world countries[15]. Other alternatives have been proposed. Due to being a biocompatible sugar, trehalose has been acquiring attention in this regard[21-24].

Up to 1929, trehalose was considered a rare sugar because it could only be isolated in relatively large amounts from the resurrection plant (1.5%, w/w) and trehala manna (20–25%, w/w), both plants with low supply. Initial protocols to extract trehalose from yeast allowed easier access to it, however not in a large scale. It was not until 1999, that large scale production methods were established, increasing the availability of trehalose and decreasing its cost. This explains why despite the knowledge of its cryoprotective effect, only now trehalose is being seriously considered as an alternative for the use of glycerol

Trehalose's mechanism of action as a cryoprotectant is not clear, though it has been suggested it binds to the membrane stabilizing it[27] or that it acts by causing the solution to vitrify instead of crystalizing while freezing[28].

However, its low permeability through the membrane leads to a reduced efficacy when applied to cells. Different strategies have been attempted to bypass this issue, namely by inducing endocytosis[29] or by applying different co-agents in order to permeabilize the membrane[22,23].

Lynch et al have used pH-dependent membrane-disruptive polymers to permeabilize the RBC membrane for trehalose to permeate through[22]. In particular, the use of PP-50, a poly- L-lysine-iso-phthalamide (PLP) polymer grafted with L-phenylalanine, proved the most effective for trehalose internalization, and, as later shown, for cryosurvival of RBCs. The authors also describe the mechanism in which the polymer attaches to the membrane, and when triggered by an acidification of the medium, changes conformation, destabilizing the membrane and allowing trehalose to permeate into the RBCs.

Stefanic *et al* have reported the use of apatite nanoparticles as an alternative co-agent to enhance the permeation of trehalose (Figure 1)[23]. They show that NPs adhere to the membrane creating transient pores which can be used for the sugar to enter the cell (Figure 2). These pores are open for short periods, not causing large or permanent injuries to the cell. Furthermore, the nanoparticles (NPs) attach to the membrane, not being able to permeate through nor inducing toxicity by interacting with internal components of the RBCs, in a reversible manner.
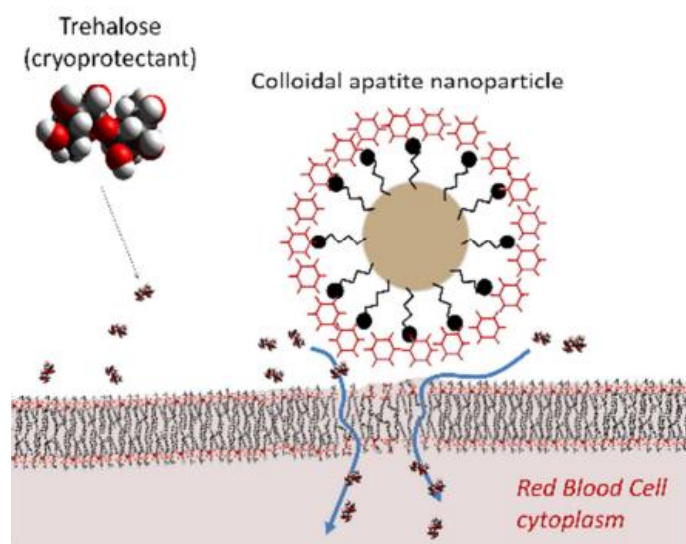
Figure 1. Schematic of the effect of a nanoparticle allowing the permeation of trehalose molecules through the cell membrane in its vicinity[23].

This new strategy opens the door to new materials, of similar size and properties, which may induce a similar behavior. Silica nanoparticles (SiNPs) are an example of such a material,

especially as their surface properties can be easily controlled via functionalization steps. SiNPs have been shown to interact strongly to the lipid bilayer, while showing little toxicity at high concentrations. These properties make SiNPs an ideal candidate to act as a co-agent for the internalization of trehalose.
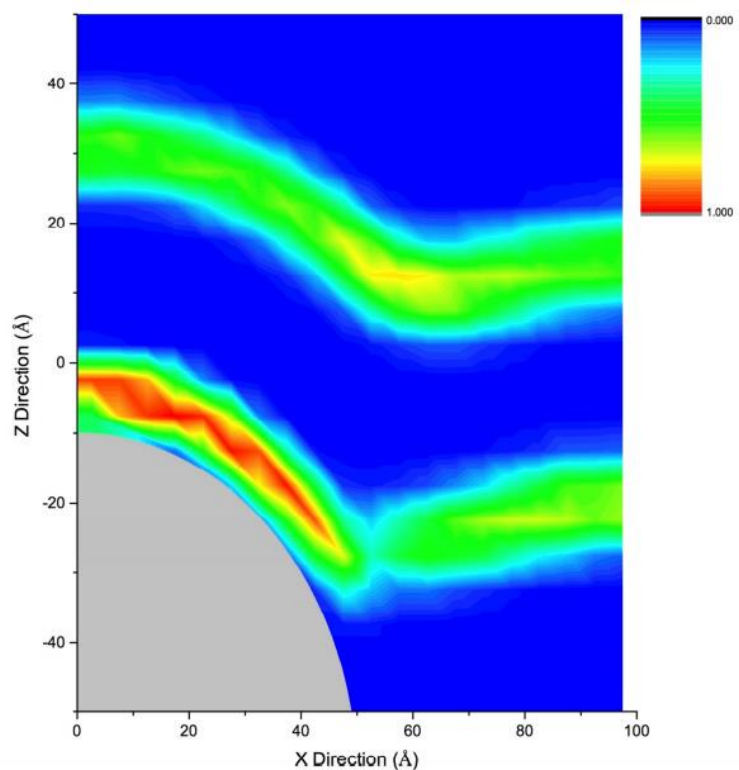
Figure 2. Single Chain Mean Field Theory calculation of interaction between an apatite NP (hydrophilic) and the lipid bilayer. NP attracts the heads of lipids (density of heads is shown in color: red – high volume fraction, blue – low volume fraction) and destabilizes the lipid bilayer making it more permeable.

1.3.   Lyophilization of RBCs

While cryopreserved RBCs can answer most of the long-term storage presented by refrigerated RBC's (i.e. the high energy consumption and limited time of storage), it still requires specialized equipment for storage and transportation. It is hard to storage these packs in places with poor conditions, as well as in a military setting during war periods. To facilitate these points, lyophilization, or freeze-drying has been suggested[15,24].

As the name implies, freeze-drying, or lyophilization, is a multi-step process where the sample is first frozen and then the solvent is removed via sublimation, a direct phase change between solid and gaseous phases. As can be seen on the phase diagram of water (Figure 3), the melting point varies with pressure, and once this is below the triple point value, it is possible to achieve this phase change[30].
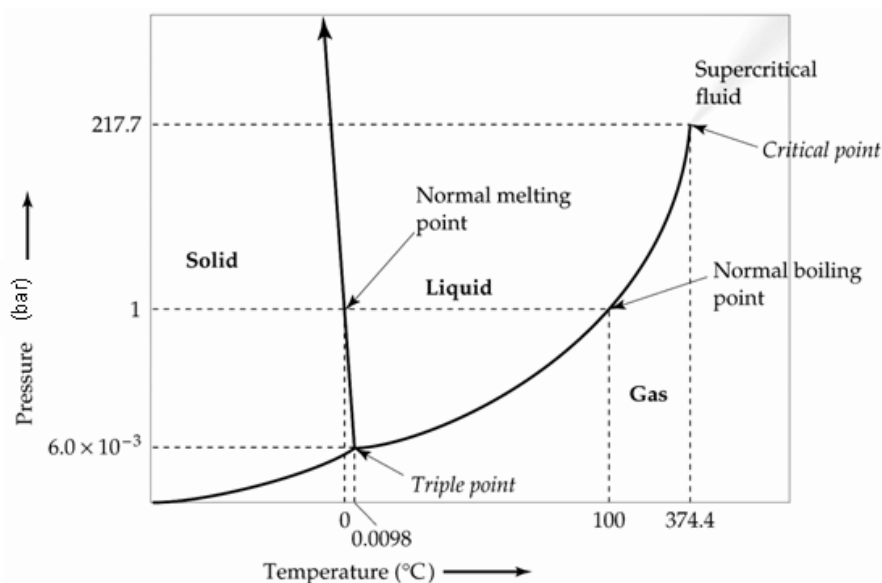
Figure 3. Phase diagram of water. In Introduction to Freeze-Drying. V. 2.1[30].

Freeze-drying gained importance during the Second World War, when it was used to deliver plasma and penicillin into the battlefields[10]. This process allowed plasma and penicillin to be rendered chemically stable and viable without requiring refrigeration. It has since been applied to other products not only in the pharmaceutical industry (vaccines, tablets, etc.), but also in the food industry as a mean to preserve the products. Other applications have been suggested, but these two industries remain the primary users of this technique.

In regard to RBCs, lyophilization promises the possibility of a compact, lightweight and stable product at room temperature[31]. This would eliminate the costs for refrigeration and difficulties of transport. Early work on lyophilizing RBC's dates back to the 1960's by Meryman[32,33]. While removal of the water content was successful, RBC membrane became too

fragile and resulted in significant lysis post-rehydration, which lead to the efforts being abandoned.

In 1992, Goodrich et al reported successful rehydration of RBCs[34,35], however further examination revealed damages to the membrane and a loss of surface area cause by vesiculation[36]. They also reported the most promising lyophilization solutions as containing membrane stabilizing agents. Nonetheless, it should be noted that attempts at reproducing these results proved fruitless[37].

1.4.　　NP interactions with living cells

NPs are usually uptaken by cells via endocytosis. Other processes can also result in particle uptake, such as phagocytosis (usually observed in monocytes or giant cells) or pinocytosis (fluid uptake, sometimes occurring for small NPs), however clathrin- and caveolae- mediated endocytosis are by far the most common[38,39]. Particle uptake is usually a two-step process: binding to the cell membrane, followed by internalization. The first step is defined mainly by the physico-chemical characteristics of the NPS. RBC's differ from most cells as they lack endocytosis mechanisms and their interaction with NPs will be looked in more details in chapter 1.6. Still it is important to understand the general knowledge on the interaction of NPs with biological systems.

Surface charge seems the most important parameter defining cell-NP interaction. Multiple observations were reported that the positively charged NPs show a higher uptake efficiency than neutral or negatively charged NPs[40,41]. This trend is not dependent on the NPs bulk composition (gold, silica, iron oxide, etc.) or cell type. While not exactly the same, surface charge and zeta (ζ) – potential are often coupled together, with the ζ-potential being used as an indication of the surface charge. When in solution, NPs are surrounded by a layer of ions (from the electrolyte solvents) strongly attached to the NP, forming the Stern layer (Figure 4). This is usually formed by protonation/deprotonation of the groups on the NP surface or by ionic interactions the ions in solution. A second, more mobile, layer is formed by the ions attracted to the surface via the Coulomb force or Brownian motion, acting to screen the Stern layer. These ions are not anchored to the NP and can move into the bulk solution. ζ-potential is defined as the electric potential between the second layer, the slipping or diffuse layer, and the Stern layer[40] (Figure 4).

Other parameters also affect NP uptake. For example, gold nanospheres have been reported to possess a higher uptake potential than gold nanorods or other polymeric shapes of NPs[42,43], showing that the shape also plays in role in promoting NP uptake. NP size is also an important factor. NPs usually exhibit an optimal size for cellular uptake, this being around 50 nm for gold[42] and silica NPs[44] and 37 nm for iron oxide NPs[45]. This optimal size may be related to the mechanism of wrapping, where particles of this size allow for single particle wrapping, but smaller particles require clustering before internalization. For larger NPs, the decreased cellular uptake can be explained by a longer wrapping time, due to a slower receptor diffusion kinetics. It has also been shown in vitro that very small nanoparticles are able to permeate the lipid bilayer, bypassing the endocytosis mechanism and directly entering the cell[39]. However, this rarely observed in favor of other internalization pathways[46].
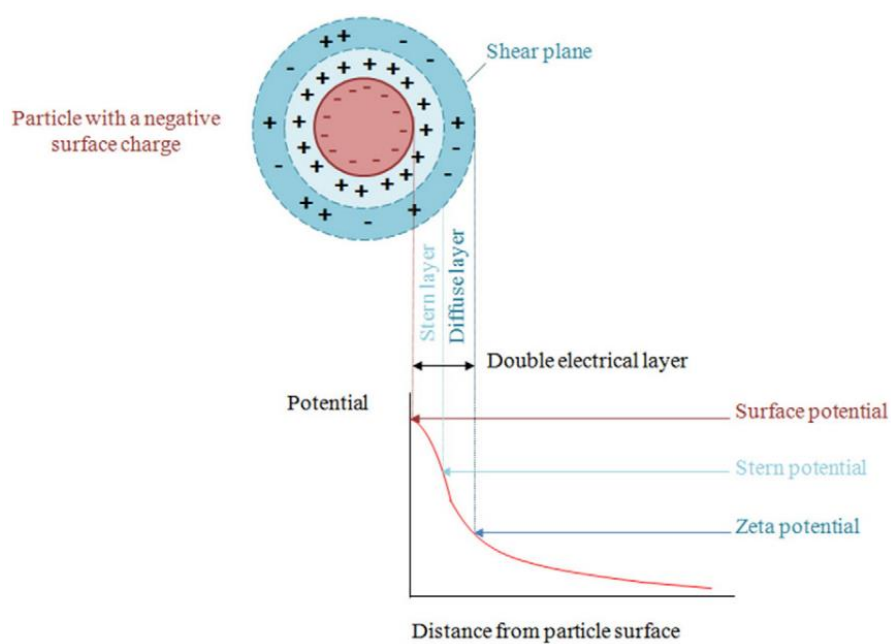
Figure 4. Double electrical layer formation at the particle surface leading to the definition of different charge potentials. Adapted from Forest and Pourchez[40].

1.5.   NP-induced toxicity

When interacting with unintended components, NPs may cause detrimental side-effects, resulting in hazards to the human health. The most common side effect reported is an increased production of reactive oxygen species (ROS) which may ultimately induce apoptosis or necrosis[39,47]. An increased production of ROS also affects various metabolic pathways, hampering the normal function of the cells.

NPs have also been reported to interact with the cytoskeleton, a structure responsible for maintaining the cell morphology and mechanical properties. In fact, several types of NPs, including SiNPs[48], iron oxide NPs[49], or carbon nanotubes[50] are known to cause structural reorganization of the cytoskeleton and/or increase of membrane stiffness.

Regarding proliferation, SiNPs are able to induce proliferation and differentiation to osteoblast-like cells[51]. Other types of NPs, like gold NPs[52], iron oxide NPs[53], or carbon nanotubes[54] also present a similar trend, however there are contradicting reports showing a negative influence on cell proliferation[55].

NP toxicity is highly concentration-dependent. Also, due the NPs' size and their difficulty of clearance, cumulative effects over increasing number of doses can also be observed[39,56]. And. even NPs which are usually considered biocompatible can induce toxicity at high enough concentrations or after several dosages.

Different cell types also exhibit different NP uptake and tolerance profiles. SiNPs have been reported to inhibit proliferation of human hepatoma HEPG2 cells, while their effect is negligible in human hepatic L-02 cells[57]. It should also be noted that up to early 21st century, the cell lines used in most of these studies were either derived from cancer cells or immortalized cell lines, rather than primary cells, directly taken from humans[56]. While these results offer valuable information, especially regarding cellular mechanisms, the information regarding dosages and toxicological parameters may not be fully accurate.

1.6.   NPs interactions with RBCs

RBCs, or erythrocytes, make up about 40% of the blood volume, and are responsible for delivering oxygen (O_2) to the body tissues, and removing excess CO_2, via the action of hemoglobin. In mammals, RBCs lose their nucleus and other organelles during their development cycle as a mean to accumulate hemoglobin. They are usually described as biconcave disks with flattened area in the center[58]. Their size varies amongst different species. For humans, RBC's are about 6-8 µm long whereas sheep RBC's have a diameter of 4-5 µm. Other shapes can also be found in certain species as llamas, who possess ovaloid RBCs, however these do not constitute the norm[58].

The RBCs' membrane is their main structural constituent. Its main function is to preserve the cell contents while allowing the cell to deform in order to transverse through capillaries and interfacing with immune cells. The RBC membrane is composed of 3 different layers: the glycocalyx, an external layer rich in carbohydrates; the lipid bilayer, composed of a mixture of proteins and lipids; and the membrane skeleton, a structural protein network located on the inner side of the lipid bilayer.

Despite the extensive knowledge of nanoparticle uptake mechanisms and the fact that NPs are in contact with RBCs in one of the main administration routes, not much is known about this interaction and how it affects RBC's. Mainly, RBC's lack endocytosis mechanisms, contradicting the knowledge obtained from different cell types, and enhancing the importance of possible interactions with the membrane[58]. As previously mentioned, Stefanic *et al*[23] suggest that upon approaching NPs, lipid heads get attracted towards the NP, causing a deformation of the membrane in its vicinity. This mechanism explains how small molecules which would normally not permeate the membrane, such as trehalose, can do so in the presence of NPs.

Attachment of NPs to the RBCs' membrane helps NPs avoiding uptake by the immune system, further increasing their circulation time and improving their delivery rate[59]. In turn, NPs have been shown to induce toxicity to RBCs in a dose-dependent manner[60]. Previous studies have shown that NPs distribute randomly over the cell surface[23,60,61]. However, these studies required cells to be immobilized, even though their natural state is in suspension, and did not investigate possible alterations to the RBCs. Herein, I analyze how fluorescent SiNPs adsorb onto freely floating RBCs, using laser scanning confocal microscopy and a novel post-processing method to allow for the high-throughput 3D reconstruction and visualization of fluorescently-labelled RBCs[61].

1.7.　　Goals and research overview

Cryopreservation of blood is an important tool to preserve rare blood types or to preserve viable units for transfusion in situations where keeping fresh units is not feasible. Current RBC cryopreservation techniques involve the use of glycerol, which later needs to be removed using specialized equipment, and storage at $-80°C$ for long storage periods, again requiring specialized equipment and high energy consumption[15,24]. These two problems lead to two main scientific gaps in the field:

1. <u>There is the need for new cryopreservation methods which are not as toxic and do not require long processing time after thawing;</u>
2. There is the need for new preservation strategies which allow for long storage periods at room temperature.

In this project, I set out to address mainly the 1st scientific gap, while keeping in mind possible alternatives addressing the 2nd scientific gap. As such, the following objectives were set in the beginning of the work:

1. Development of image analysis techniques to assess RBC structure.
2. Analysis of buffer composition on RBC cryopreservation.
3. Application of SiNPs as a co-agent for trehalose delivery.

The first objective aimed at supporting the analysis required to support the remaining goals. For this, different techniques were established: incorporation of pixel intensity analysis for the determination of freezing and melting points, 2-dimensional shape analysis of RBC images obtained using a freeze-drying microscope, and high-throughput 3-dimensional shape analysis of freely floating RBC images obtained using a laser scanning confocal microscope.

The tasks to complete the second objective are described in chapter 3 and aimed at identifying key parameters affecting RBC cryopreservation. This task looks at the action of trehalose alone as a basis for future optimization of cryopreservation protocols, especially upon addition of the co-agents. After determination of the freezing and melting points, which acted as a basis for establishing freeze-thawing protocols, osmolarity, salt and sugar molecules, and pH were analyzed according to the survival of RBCs after thawing.

Finally, in chapter 4 is described the analysis of the interactions of SiNPs with different surface charges using laser scanning confocal microscopy (LSCM). Dose-dependent SiNP toxicity was assessed using an hemolysis assay, and the interaction of SiNPs with RBCs was studied using the technique developed as part of objective 1. Herein, I analyzed the number of SiNP clusters

adsorbed onto RBCs according to the concentration and surface charge and possible morphological changes arising from this.

2. Visualization techniques for cryopreservation

2.1. Absorbance and Fluorescence

When materials are heated in flames, put in electrical discharges or irradiated at certain wavelengths, they are able to emit heat or light at well-defined frequencies. These phenomena constitute the basis of absorbance and fluorescence, and while known in the mid-19th century, their current understanding is due to the advent of quantum physics[62].

Upon irradiation from a light source, a material is able to absorb part of the energy (the remaining energy can be reflected or transmitted), entering an electronic excited state[63] (Figure 5-1). This transition is defined, requiring the exact energy to occur. In practice, this leads to the occurrence of peaks in the absorption or excitation spectra (Figure 6).

Excited samples usually remain in this state for a period of time, during which conformational changes occur and allowing for interactions with the environment. This results in a relaxed excited state due to dissipation of the energy[63] (Figure 5-2).

When the return to the ground state is accompanied by the emission of a photon, it is defined as a radiative process (Figure 5-3). When this transition occurs between the same type of states (singlet-singlet transition), it is defined as fluorescence. Due to the energy dissipation during the excited lifetime of the material, the emitted photon has lower energy than the excitation photon, phenomenon defined as the Stokes shift, resulting in the shift of the emission spectrum relatively to the excitation or absorbance spectra[63].
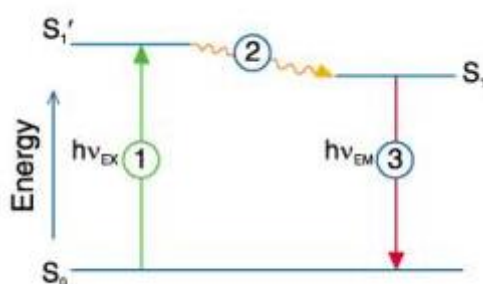
Figure 5. Jablonski diagram illustrating the processes involved in the creation of an excited electronic singlet state by optical absorption and subsequent emission of fluorescence. The labeled stages 1, 2 and 3 are explained in the text. Image retrieved from The Molecular Probes Handbook[63].

While absorbance and fluorescence are both related to the interactions of light with the sample, their measurement is fundamentally different. In the case of fluorescence measurements (fluorescence emission, excitation spectrum, and emission spectrum), sample emission is directly detected by placing the detector in such a manner that the irradiated light is not captured[62] (in standard fluorospectrometers, it is placed at 90° relatively to the light source and the sample). These measurements are usually unitless as fluorescence emission is

dependent on several parameters, such as intensity of irradiated light, fluorescence quantum yield and concentration of fluorophore and irradiated wavelengths. In the specific case of excitation and emission spectra, they are measured by fixing the emission or excitation wavelengths, respectively, and measuring the fluorescence emission as the counterpart wavelength varies[63].
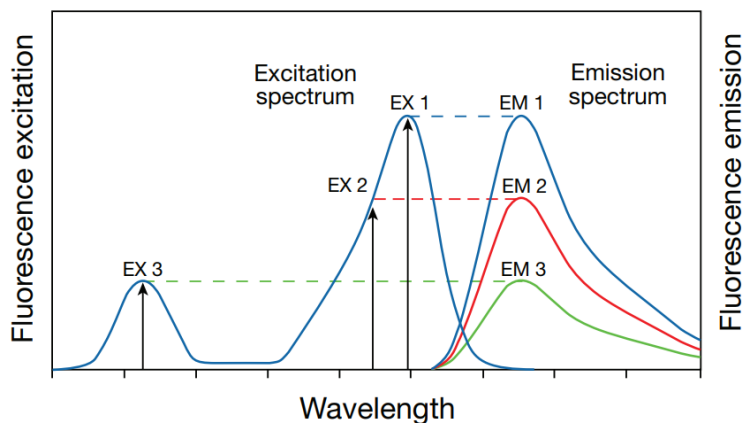
Figure 6. Excitation of a fluorophore at three different wavelengths (EX 1, EX 2, EX 3) does not change the emission profile but does produce variation in fluorescence emission intensity (EM 1, EM 2, EM 3) that corresponds to the amplitude of the excitation spectrum. Image retrieved from The Molecular Probes Handbook[63].

In the case of absorbance measurements, we're detecting the intensity of the transmitted light (I) and relating it to the irradiated light (I_0), relationship defined as transmittance (T). Absorbance (A) is then defined as:

$$A = -\log T = -\log \frac{I}{I_0} = \log \frac{I_0}{I}$$

Absorbance is usually used over transmittance as it is dependent on the concentration of solute (c), and the length of optical pathway (l) as described by the Bouguer-Lambert-Beer law:

$$A = c\, \varepsilon\, l$$

Where ε is the solute's molar extinction coefficient, a constant specific for each molecule and for a specific wavelength. As the length of the optical pathway is fixed for all samples, the solute's concentration can be easily determined once the absorbance is known[62].

2.2. Brightfield Microscopy

The advent of microscopy as a field of science was brought by the publication of the book "Micrographia" by Robert Hooke[64]. In this book, Hooke showed drawings of his observations with the microscope making the microcosm available for the general audience, while until then observations with a microscope were considered a hobby for the rich. It was also in this work that Robert Hook coined the term "cell" initially referring to the microscopical enclosures he found on cork. For his observations, Hooke used a compound microscope designed by Cristopher Cock, further improved by adding an oil lamp as an illumination source and a glass filled with water to focus the light on the sample[64]. While rudimentary, the design by Robert Hooke contains the main components which still make modern microscopes. Similarly to Hooke's design, modern microscopes possess a lamp as illumination source, a condenser to focus the light on the specimen, an objective to capture the light and magnify the image and an ocular to allow visualization[65,66](Figure 7). Alternatively, the image can be captured using a camera. The intensity of illumination and orientation of light pathways throughout the microscope can be controlled with strategically placed diaphragms, mirrors, prisms, beamsplitters, and other optical elements to achieve the desired degree of brightness and contrast in the specimen.
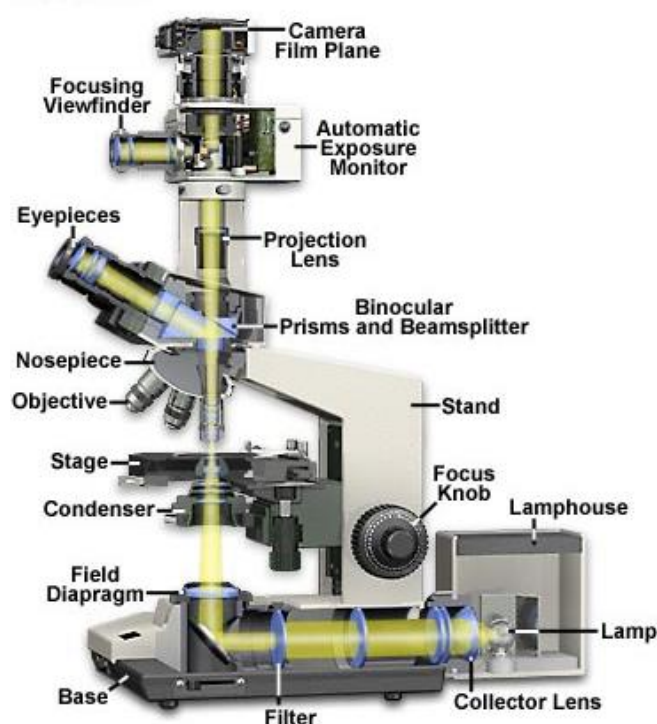
Figure 7. Diagram of the components of a modern brightfield microscope. Image adapter from Olympus website[65].

Since the time of Robert Hooke, there were many contributions to the development of microscope lenses, improving image quality and magnifying power, but the most important

contribution was that of Ernst Abbe[64]. While working for Zeiss Optical Works, in addition to several important contributions to improve lenses quality (p.e. the invention of apochromatic lenses), Abbe described the resolution limit of the microscope, resulting in the equation:

$$d = \frac{\lambda}{2NA}$$

Where d is the smallest resolvable distance between two objects, λ is the imaging wavelength and NA is the Numerical aperture[65,66]. This equation holds true for modern techniques such as LSCM and it's understanding is important to improve image quality.

While it is important to understand how to achieve the highest possible resolution, it is often the case that image quality is too low to distinguish two objects. This was often the case in classical brightfield microscopy, where the background signal hid details from the sample. With this in mind several dyes were developed in order to increase contrast between the labelled structures and the background[67]. This idea of increasing contrast is also present in different microscopy techniques such as phase contrast microscopy, which makes use of phase shifts in the light as it crosses the sample to increase contrast., or, ultimately, epifluorescence microscopy, which highlights the labeled structures amidst of a dark background.

2.3. Freeze-drying microscopy

Freeze-drying microscopy is a fundamental part of the development cycle of a new lyophilization formulation or protocol. This technique allows the determination of the eutectic temperature (temperature at which the solute melts, preventing the formation of any structure upon removal of the solvent) and collapse temperature (temperature at which the material softens to the point of not being able to support its structure)[30].

Freeze-drying microscopy analysis is performed by reducing the temperature until the sample is frozen, followed by reducing the pressure inside the chamber. This leads to sublimation of the solvent and subsequent drying of the sample. The collapse temperature is determined by slowly increasing the temperature during the drying process, until the dried sample no longer maintains its structure (Figure 8)[30].

Freeze-drying microscopy is performed using a Lyostat (Figure 9), a microscope developed by Biopharma Technology Ltd in collaboration with Linkam. The Lyostat varies from standard brightfield microscopes by possessing a temperature and pressure-controlled chamber, and by using polarized light to visualize variances in the crystal structure of the frozen sample. The temperature- and pressure-controlled chamber allows the microscope to reproduce a small scale freeze drier while also allowing the visualization of the sample in real time[68].
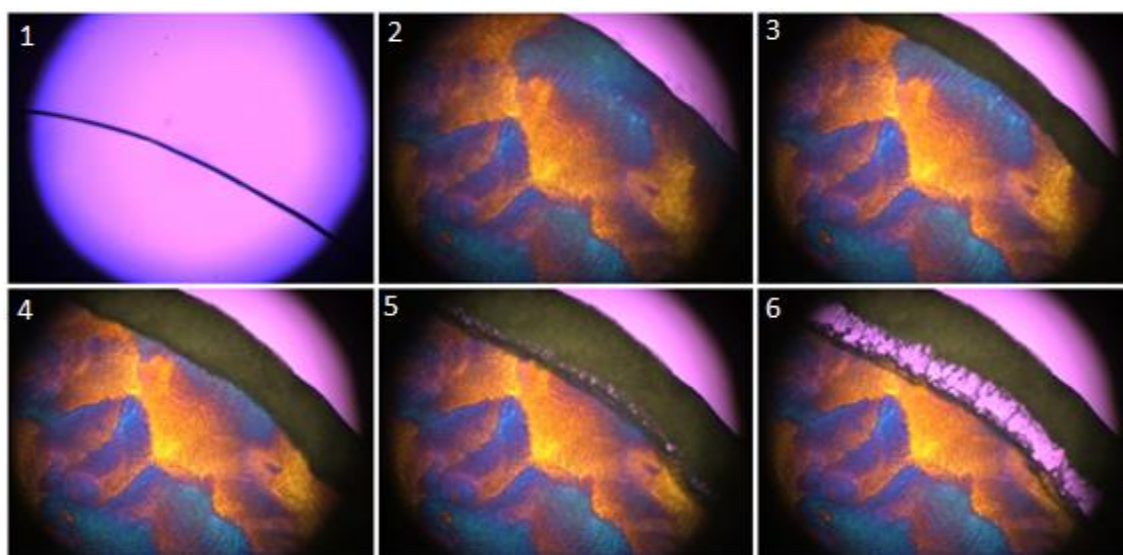
Figure 8. Example of a development cycle for the determination of the collapse temperature in freeze-drying microscopy. The sample is placed on the holder (1) and temperature is decreased until the sample is frozen (2). Afterwards, the pressure inside the chambed is decreased, via an air pump, and temperature is slowly increased, causing the sample to dry(3-4). Once temperature reaches the sample's collapse temperature, a loss of structure becomes apparent(5-6). Adapted from biopharma.co.uk[68].
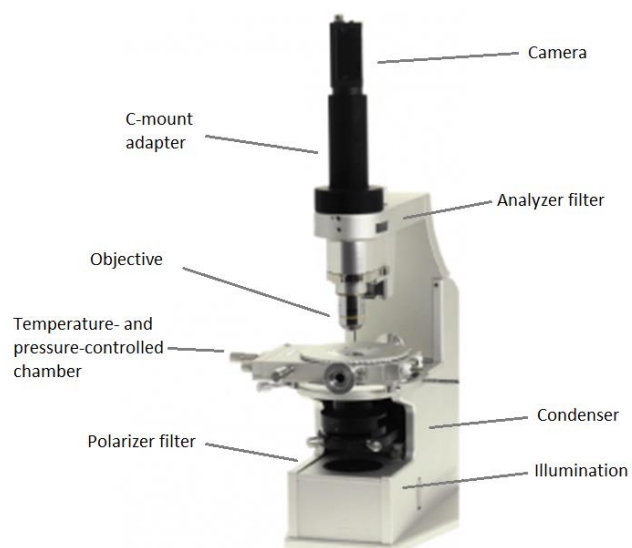
Figure 9. Diagram of the components of a Lyostat for freeze-drying microscopy. Adapted from biopharma.co.uk[68].

2.4.　　Laser Scanning Confocal Microscopy

Laser Scanning Confocal Microscopy (LSCM) has proved one of the most important advances for cell biology. The basic idea behind LSCM is the use of spatial filtering techniques to eliminate out-of-focus light in specimens thicker than the plane of focus[67].

Truth be told, comparing to widefield fluorescence microscopy, LSCM offers marginal improvements in resolution[66]. Its main improvement relies on the exclusion of emission light originating form area outside the focal plane.

Coherent light immitted by the laser system passes through a pinhole which is aligned with the scanning point- As the laser light is reflected by a dichroic mirror to excite the sample, fluorescence light emitted it travels back across the dichroic mirror and are focused on the detection pinhole (Figure 10). While emission still occurs at points above and below the focal plane, it is largely excluded by the pinhole barrier, where only light originating from the focal plane is able to cross the aperture[67].
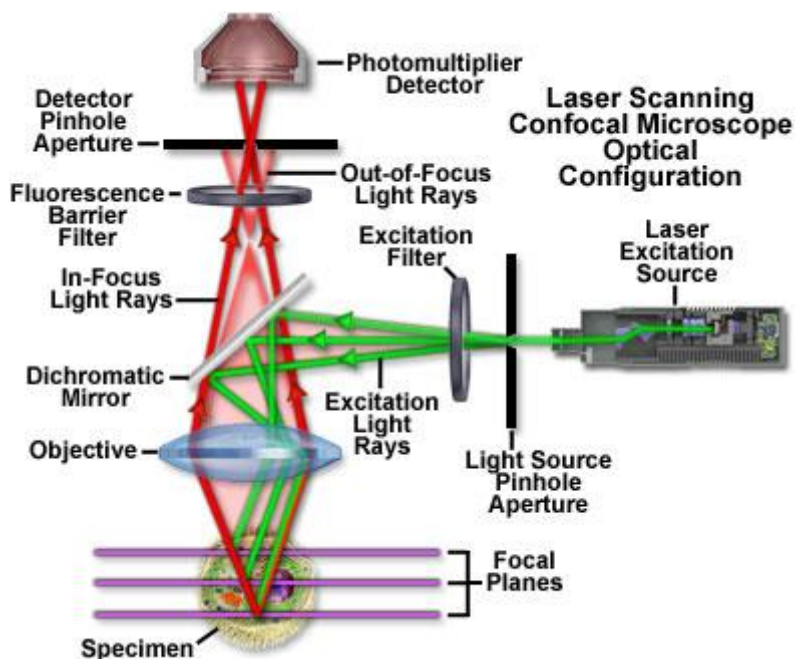
Figure 10. Diagram of the working principle behind a LSCM microscope[67].

The second difference to widefield fluorescence microscopy is the light source. Whereas traditionally the sample is illuminated by a mercury or xenon lamp and the image can be visualized on the ocular or camera, LSCM uses one or several lasers as excitation sources, a scan head with optical and electronic components, an electronic detector (usually photomultiplier tubes), and a computer for processing and displaying the image[67]. Thus, the mechanism of image formation in LSCM is fundamentally different from traditional microscopes.

In LSCM, the image is generated by scanning the sample across a defined area in a raster pattern, i.e. the beam is moved from the left to the right along the x axis, and once it reaches the end, it is transported back and shifted along the y-axis. The process can be repeated at the end of each line or each frame in order to improve image quality by averaging different measurements. After acquisition of each frame, the sample can be moved along the z-axis via a stepper motor effectively achieving a 3d image reconstruction[67].

3. Image Analysis Techniques for Cryopreservation

As previously mentioned, the determination of fusion point and collapse temperature is amongst the first steps of the development cycle of a new freeze-drying formulation[30]. Current state-of-the-art methods rely on direct visualization of the sample during a freeze-drying cycle using a freeze-drying microscope. Incorporation of image analysis tools during the process can easily provide more accurate measurements without requiring expensive hardware upgrades.

3.1. Determination of the fusion and melting points of blood

In the particular case of blood, it is a highly complex mixture, composed not only of dissolved solutes in solution, but also of undissolved components, i.e. erythrocytes, leucocytes, platelets and other. These components add an additional layer of complexity to the process as maintaining their structure and function is during the freeze-drying cycle, storage and reconstitution is of high importance. The complexity of the sample has often resulted in its degradation during the freeze-drying-reconstitution process. However, due to the extreme conditions required during the drying process, it is not possible to analyze the sample after each step, to understand what is not working as intended. In this chapter, I show a post-processing method to specifically analyze the freezing and melting points of blood using freeze-drying microscopy.

The standard approach for determination of the freezing and thawing points required looking at individual images until a visual change is detected[30]. Herein, I show a method to analyze change in image intensity profile throughout time while relating it to the chamber temperature. As the sample solidifies, diffraction increases and not allowing light to be transmitted through the sample. The opposite happens during the thawing process, increasing the intensity of transmitted light.

After acquisition of a freeze-thawing cycle, individual images are exported and stacked as a time-lapse movie for analysis (Figure 11). A Region of Interest (ROI) is selected (Figure 11) and an intensity profile is measured throughout the time-lapse movie (Figure 12A). Intensity (I) can then be plotted against the temperature measurements taken at the same time of the images. The results can then be further analyzed by plotting the variance of intensity (dI) versus the temperature ($dI = I_n - I_{n-1}$), as shown in Figure 12B.
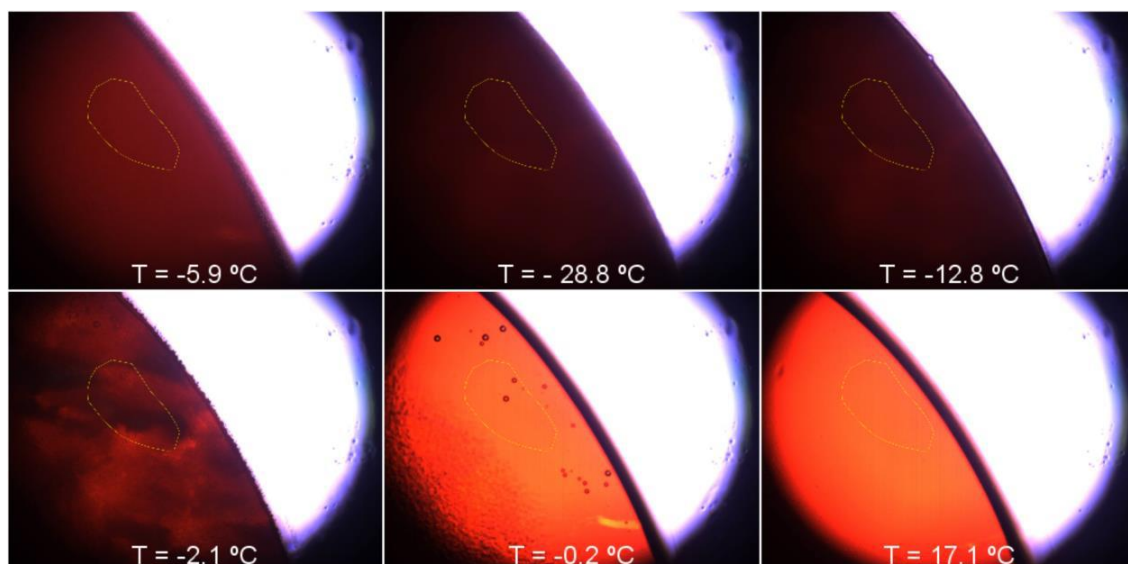
Figure 11. Example of a time-lapse video acquired of the freeze-thawing cycle of sRBCs in PBS. The temperature was reduced allowing the sample to freeze and then slowly increased until 37°C. Similar videos were acquired for sRBC's suspended in different media. The yellow line delimits the selected ROI.

Using the intensity variation profile (Figure 12C), it is possible to determine the freezing point according to the peak in the freezing curve. The fact that the peak is so pronounced is indicative of a fast transition from liquid to solid state. As the chamber temperature remains below the freezing temperature the sample is still cooling further down, causing a decrease of intensity even if the chamber is warming up. The moment this tendency is inverted is indicative of the sample starting to melt. As such, we can determine the sample's melting point according to the minimum in the thawing curve of the intensity profile against the temperature (Figure 12B). The melting process is slower as energy transfer only occurs via conduction at the contact surfaces of the frozen core.

After the phase transition is completed, it is noticeable a much higher intensity than before the freeze-thawing process. Damage to the RBC's resulting from the state transitions creates a more homogeneous solution. As RBC's lose their structure and become unnoticeable in solution, they no longer diffract light, allowing it to be transmitted through the sample and causing an increase in the detected intensity.

Determination of the freezing and thawing points for RBC's suspensions in different solvents shows the freezing and thawing points are very close (Table 1), suggesting the fast freezing observed is not due to a supercooling event, and the RBC's may be acting as a nucleation core to start the phase transition. It should also be noted that freeze-thawing cycle causes damage to the RBC's. As such, even if a cryoprotectant is used, repeated cycles should be avoided under penalty of damaging the sample.
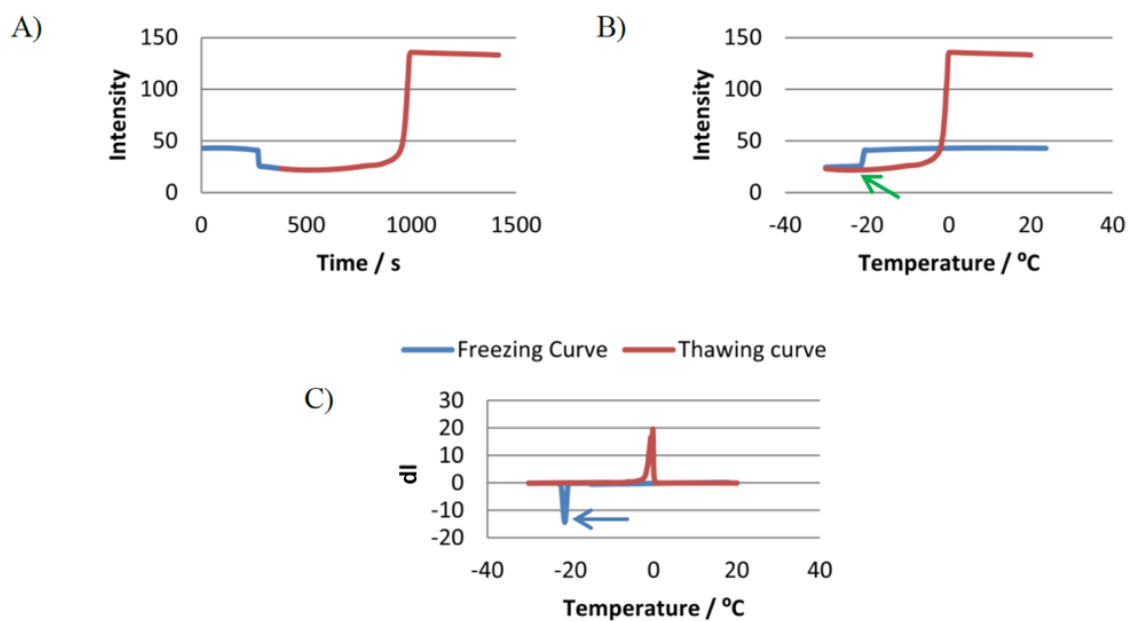
Figure 12. Intensity profiles of the freezing and thawing curves of sRBC's suspended in PBS plotted against time (A) and temperature (B), and intensity variation profile (C). The blue arrow indicates the freezing point and the green arrow indicates the thawing point. **d**

Table 1. Freezing and thawing points of sRBC's suspension in different solvents.

Solvent	Freezing point / °C	Thawing point / °C
PBS	-22	-23
0,5M Trehalose in PBS	-21	-20
3x PBS	-21	-23

3.2.   RBC's survival rate after cryopreservation

As previously mentioned, standard blood cryopreservation protocols aim at either slowly cooling the sample, forcing water to exit the cells via osmosis, or rapidly freezing the sample in liquid nitrogen, whilst promoting vitrification as a mean to avoid crystal formation. As for thawing, samples are usually thawed at 37ºC to decrease the period of time they remain at low temperatures. Still, even though the combination of these protocols is known to produce favorable results, the influence of each freezing and thawing conditions or buffer composition is not fully understood. In order to further understand the influence of the freezing and thawing rates as well as sample composition, different combinations of all freezing and thawing protocols were tested, followed by testing different buffer compositions using the optimal procedure.

Freezing conditions were tested as follows: slow cooling, at -0.5 °C / min in the freeze drier; medium cooling, by inserting the sample into the freeze-drier after it had been cooled down to -40 °C; and flash freeze, by immersing the samples in liquid N_2. Each cooling condition was coupled with different thawing conditions as follows: immersion in 37 °C water bath with constant shaking; kept at room temperature; at 0.5 °C/min in the freeze drier; and kept in the 4°C fridge overnight. All conditions were tested for RBCs suspensions in different solvents: 0.5 M trehalose; 3x PBS; and PBS. 3x PBS was selected due to possessing the same osmolarity as the trehalose solution.

RBC's survival in PBS was very low across all freeze-thawing conditions applied, not being possible to detect any remaining hemoglobin. For sRBC's suspensions in 3x PBS and trehalose solution the best conditions seem to be medium freezing coupled with either incubation at room temperature, incubation at 4 °C, or 0.5 °C/min in the freeze-drier for thawing or flash-freeze coupled with thawing at 37 °C water bath (Figure 13). For the remaining conditions, RBC's survival was very low for the samples suspended in 3x PBS, while trehalose seems to still possess a small protective effect for the samples frozen under slow freezing and medium freezing conditions.

Opposing to freezing in 3x PBS, Trehalose is able to offer some protection when freezing the RBCs at slow cooling rates. However, it remains unclear why certain combinations of freezing and thawing conditions much more effective at protecting the cells from freezing damage. Additionally, the fact that the 3x PBS solution is able to protect the RBCs through the freeze-thawing cycle suggests that osmolarity plays a role in this effect. Medium cooling likely reaches an acceptable ice crystal growth rate, promoting a local upconcentration of the solvent and further pressuring water out of the cells via osmosis. On the other hand, slow cooling likely

results in larger crystals which end up damaging the cells. Regarding the flash-freezing approach, it is interesting that only when thawed at 37°C samples retain their viability, while all other thawing approaches resulted in the degradation of the sample. These results are opposite to what is observed for medium cooling suggesting an alternative preservation method. In fact, due to sample size and the fast cooling rate, it is possible that instead of crystalizing into ice the solution undergoes a vitrification process. Regarding the thawing rate, it is important to remember that all these processes are dynamic, and vitrification requires the temperature to decrease abruptly allowing the sample to bypass the glass transition temperature without formation of ice. Slow thawing methods may allow molecules to restructure into ice crystals resulting in damage to the cells.
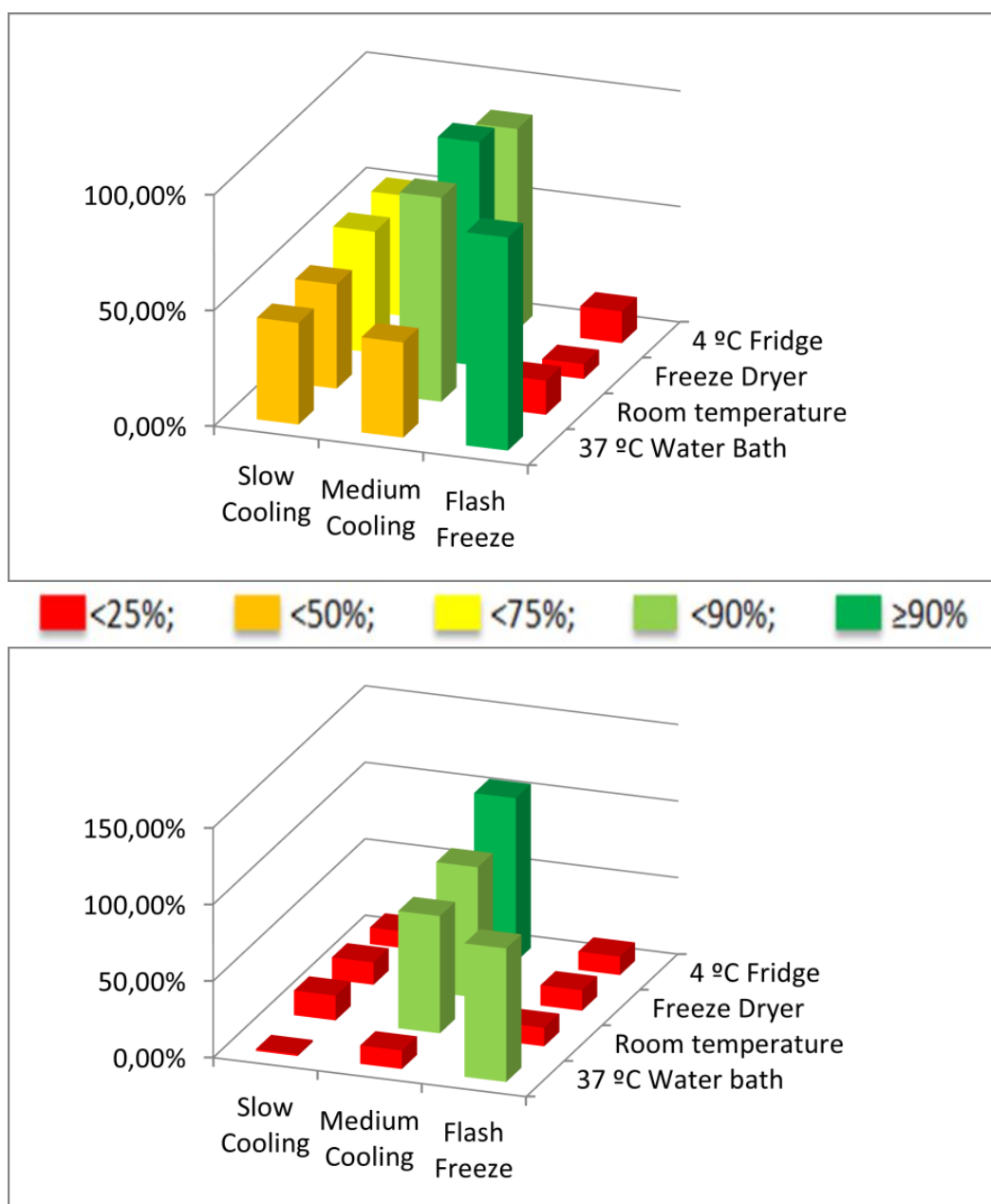
Figure 13. sRBC's survivability upon freeze-thawing in 0.5 M trehalose (A) and 3xPBS (B).

Using medium cooling coupled with thawing at 4ºC, several properties were studied in order to assess their influence on RBC survival after freeze-thawing: Osmolarity, using different concentration of PBS; salt balance, by comparing isotonic solutions of 3x PBS, and KCl in PBS; pH, by using either PBS or 0.36 M trehalose in PBS at pH 7.4, 7.05 and 6.5; and sugar molecule, using either trehalose, sucrose or glucose solutions (0.36 M in PBS)(Figure 14).

All tested parameters seem to play a role on RBC survival. In regards to osmolarity, hypotonic and isotonic solutions resulted in most RBCs dying during the freeze-thawing cycle; however there is little variation between 2x PBS and 3x PBS solutions. The higher survivability of the latter can be explained by crenation of the RBCs. RBCs immersed in a hypertonic solution will undergo crenation due to water leaving the cell via osmosis. Thus, there isn't enough water available during freezing to form harmful ice crystals inside the cells. The lower survivability between the 3x PBS solution as compared to the previous experiment can be related to the age of the sample. While not directly tested, a trend could be noticed where sample age is directly correlated to the freezing damage suffered by the sample. Salt balance also seems to contribute towards RBCs survival, as the excess of K$^+$ ions mays affect the membrane potential across the cell membrane and may lead to freezing damage. As far as pH goes, the fact that the solvent is hypertonic and contains trehalose seems to have a higher contribution to RBC survival, however, amongst different trehalose solutions, data obtained confirms previous results[23] where a slightly acidic environment helps to protect the cells. Lastly, amongst the different sugars tested trehalose has a higher protective effect, confirming previous observations[24]. While it is not fully understood the mechanism which causes trehalose to be more effective than other sugars, it has been suggest it can act vitrification of the solvent[28] or by replacing water molecules around and inside the cells[27].
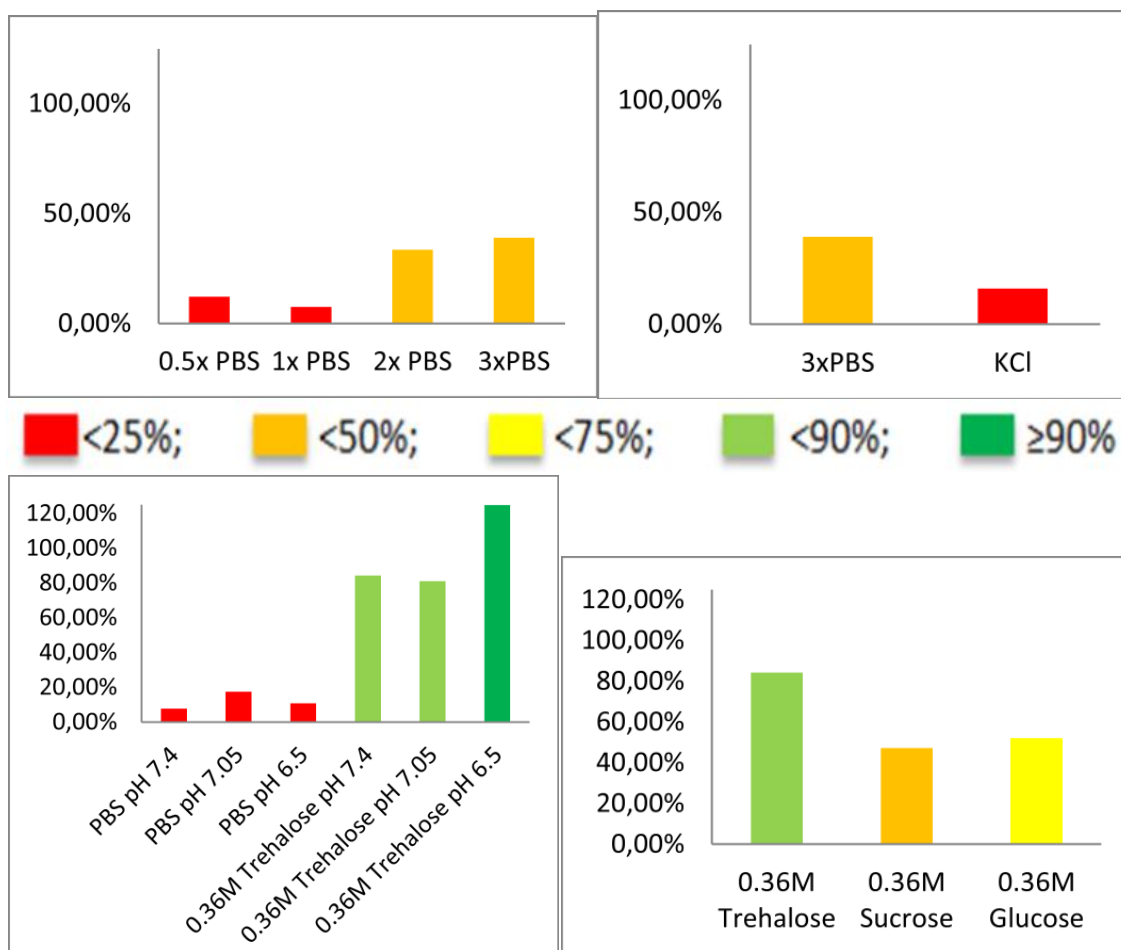
Figure 14. Effect of osmolarity (A), salt balance (B), pH (C), and sugar molecule (D) of the solvent during the freeze-thawing cycle on sRBC survival.

3.3.   RBCs population analysis

To further understand the influence of the different parameters, the RBC samples were prepared as smears and imaged with a freeze-drying microscope adapted as a brightfield microscope. RBC's were individually analysed according to their morphology (Figure 15). After correcting the background, individual cells were selected by creating a mask using a "mean" automatic threshold filter available in the FIJI distribution of ImageJ and adjacent cells were separated by applying a watershed algorithm also available in the package. Individual cells were then selected based on their size (objects too small are excluded as they likely constitute debris and objects too large are excluded as they might correspond to multiple cells) and measured for the area occupied. This sequence of actions was automated via a custom ImageJ script, allowing the analysis of multiple files in rapid sequence. Results were then plotted as an histogram and a gaussian curve was fitted. Using this approach provides a more accurate description of the analysis compared to directly analyzing the extracted results as it takes into account the distribution of the cells, predicting size distributions which are not possible to include in the analysis. By considering the RBCs as circular, it is possible to determine the average diameter of the population based on the area occupied. Results for the cells in a isotonic solution (PBS) show the average diameter is within the expected range for sheep RBCs (4-5 µm)(Table 2), validating this method.

As expected, hypertonic solutions result in smaller RBC's (Table 2) due to crenation of the cells. It should be noted that even though the 0.5M trehalose and 3x PBS solution were isotonic in relation to each other, RBC's population differ in size suggesting that osmotic flow is not the only factor affecting cell size and that trehalose has some effect on cell morphology.
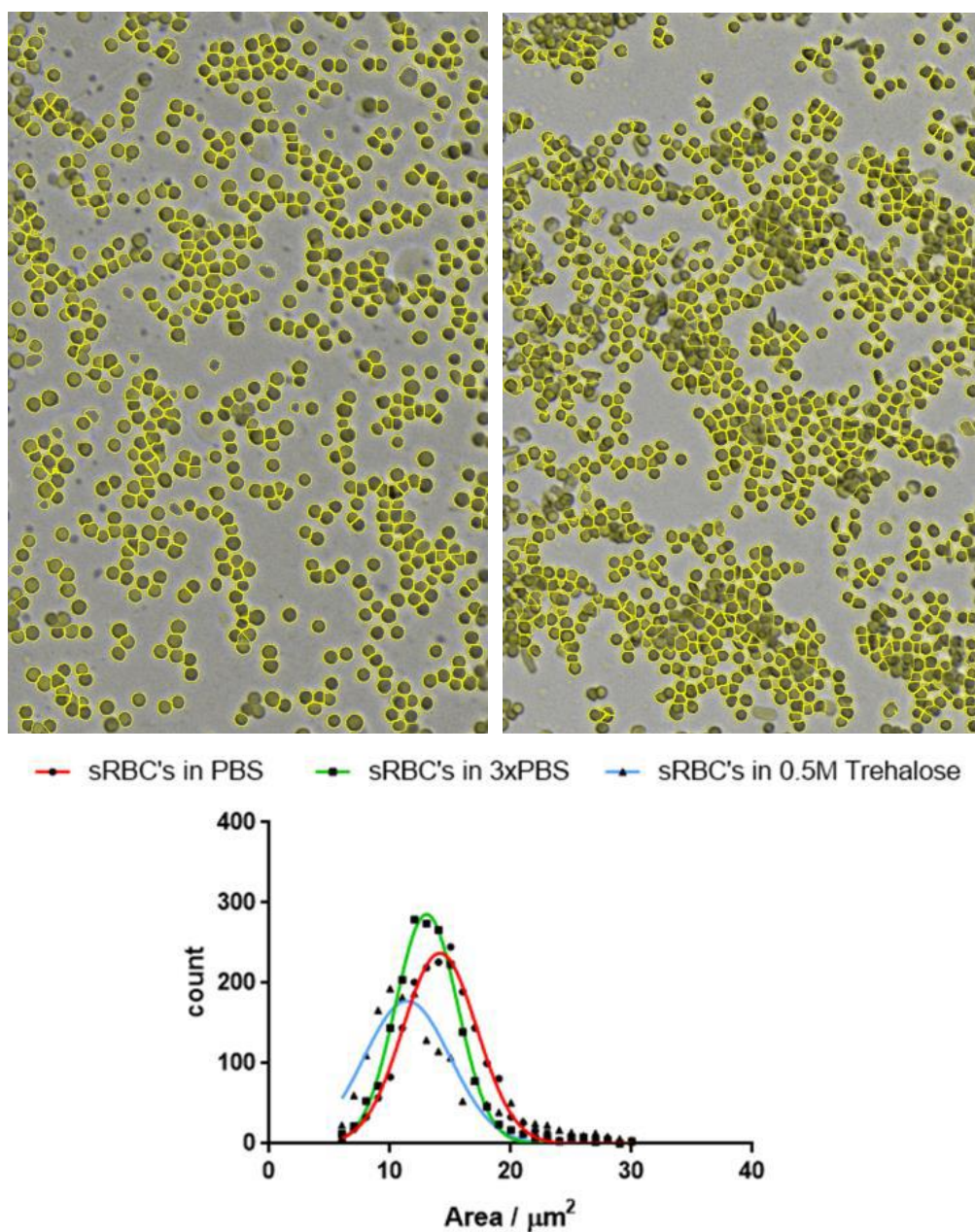
Figure 15. Examples of micrographs of sRBC's suspended in PBS (A) and in 0.5 M trehalose (B) overlayed with the threshold result. And sRBC's population analysis from sRBC's suspended in different media. Population analysis was performed from at least 3 individual images taken in different regions from a single sample.

Table 2. sRBC's population description when suspended in different solvents. Diameter is calculated by assuming RBC shape as circle.

	sRBCs in PBS	sRBCs in 3xPBS	sRBCs in Trehalose
Average / μm^2	14.12	13.02	11.41
std dev / μm^2	3.062	2.569	3.564
SEM / μm^2	0.06563	0.04755	0.2613
Diameter / μm	4.24	4.07	3.81

Analysis of sRBC's population after freeze-thawing in different solvents shows an increase of sRBC's size after treatment (Table 3). This could be an indication of cell damage due to sample

freezing. Alternatively, the size increase could be related to an aging process, as the control sample had been imaged one week prior. More data needs to be acquired to identify the process behind this increase in size.

Table 3. sRBC's population description before and after a freeze-thawing cycle in different solvents. All samples were imaged in PBS. Diameter is calculated by assuming RBC shape as circle.

	Before Freeze-Thaw	FT in 3xPBS	FT in 0.36M Trehalose	FT in Trehlalose pH 7.05	FT in Trehalose pH 6.5	FT in Glucose	FT in Sucrose
Average / μm^2	14.12	17.88	15.58	15.45	16.29	16.13	16.55
std dev / μm^2	3.062	2.145	2.225	2.002	2.439	1.819	2.695
SEM / μm^2	0.066	0.182	0.057	0.099	0.170	0.054	0.133
Diameter / μm	4.24	4.77	4.45	4.44	4.55	4.53	4.59

3.4.   Lyophilization of RBCs

Freeze-drying, or lyophilization, is an innovative approach to preserve blood samples. While potentially, it can offer several improvements by allowing samples to be preserved at room temperature, so far researchers have not found a viable strategy to restore the sample without it having suffered any damage.

Herein, in order to try to preserve the RBC's in dry conditions, RBC's suspensions, in different solvents as described for the freeze-thawing cycles, were frozen in liquid N_2 and dried by reducing the pressure in the freeze-drier chamber until the samples were fully dry (~ 2days).

Other freezing conditions showed problems with sample freezing as sample position in the freeze-dryer affects the sample temperature, causing variances within the same batch. Ultimately, it caused some of the samples to collapse during the freeze-drying cycle.

By freezing the samples in liquid N_2, it was possible to acquire homogeneous "cakes", indicating the sample was fully dry (Figure 16). The samples were reconstituted with PBS to avoid local hypotonic regions during the reconstitution process. Still, after reconstitution, samples exhibited a cherry color indicative of the oxidation of hemoglobin (Figure 17). After centrifugation, there was no pellet formed, indicating the treatment caused the destruction of the RBC's.
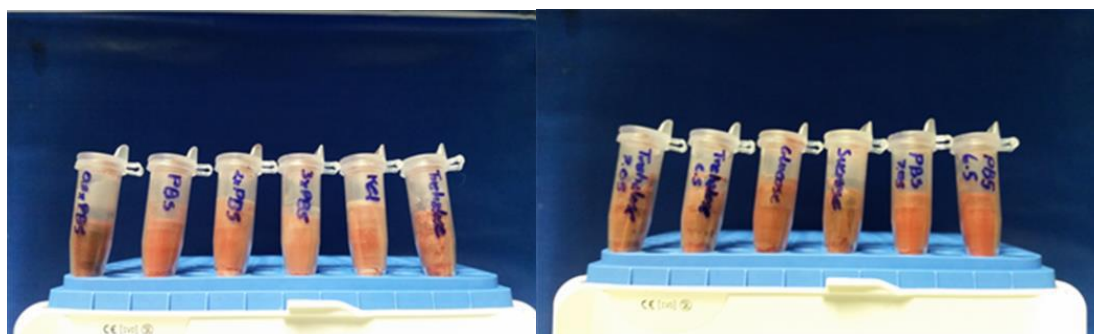
Figure 16. sRBC's suspensions in different solvents after freeze-drying.

Figure 17. Freeze-dried RBC's samples after reconstitution with PBS.

By imaging the powder obtained after freeze drying, it is visible that spherical structures are still present, however completely enclosed in a crystalline structure (Figure 18). For some of the spherical structures, the crystalline structure surrounding is not very developed, however a thin crystalline layer can still be observed (Figure 18B). This suggests RBC's can act as a nucleation core for salt crystals during the drying process.
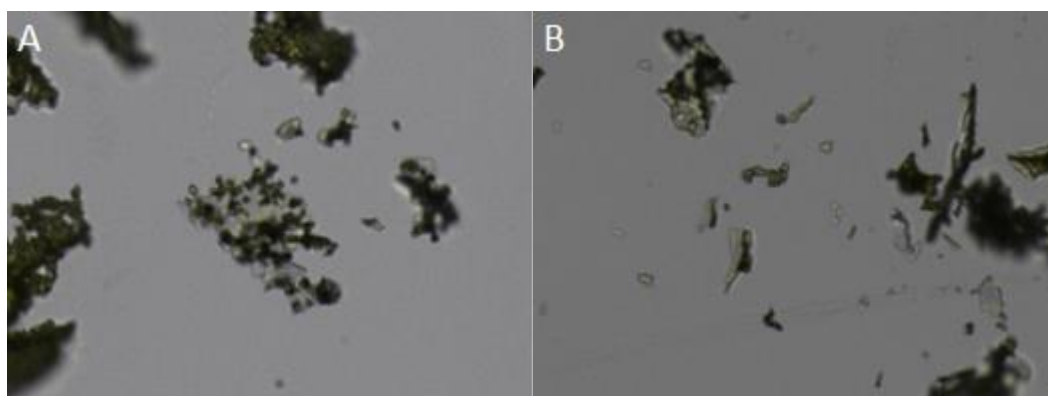
Figure 18. Micrographs of RBC's samples after freeze-drying. The powder obtained was crushed to separate individual crystals. Spherical structures can be found usually surrounded by a developed crystalline structure (A) or, occasionally by a thin crystalline layer (B, indicated by the green arrow).

4. Interactions of SiNPs with RBC membrane

4.1. SiNPs toxicity

When fluorescent SiNPs are mixed with a suspension of RBCs, SiNPs are able to attach to the membrane of the RBCs. This process depends on the surface properties of the SiNPs and may affect the viability of the RBCs. To study the influence of the surface properties on the adsorption to membrane and ultimately how it affects the RBCs, three types of SiNPs with different negative charge at physiological pH were tested (Table 4)

Table 4. ζ-potential measurements of SiNPs employed in this study.

Plain-SiNPs	COOH-SiNPs	NH$_2$-SiNPs
-54.8 mV (±7)	-63.7 mV (±7)	-39.5 mV (±7)

RBC's survivability was measured with a hemolysis assay. In order to more accurately quantify hemoglobin concentration using the absorbance spectra, the contributions of each species of hemoglobin was taken into account. Plain and highly negative charges present similar hemolysis values and are able to disrupt RBCs at concentrations higher than 1 mg mL^{-1} (Figure 19). Comparing with the literature, similar size NPs show similar hemolysis rate at high concentration (~20%) however, the least negatively charged NH$_2$-SiNPs show higher toxicity (~40%) which is likely associated with a stronger attachment to the membrane. These observations are in accordance to the concentration of SiNPs attached to the RBCs. While the surface charge helps particles attach to the membrane, their toxicity seems to be driven not by charge, but by the amount of particles adsorbed.
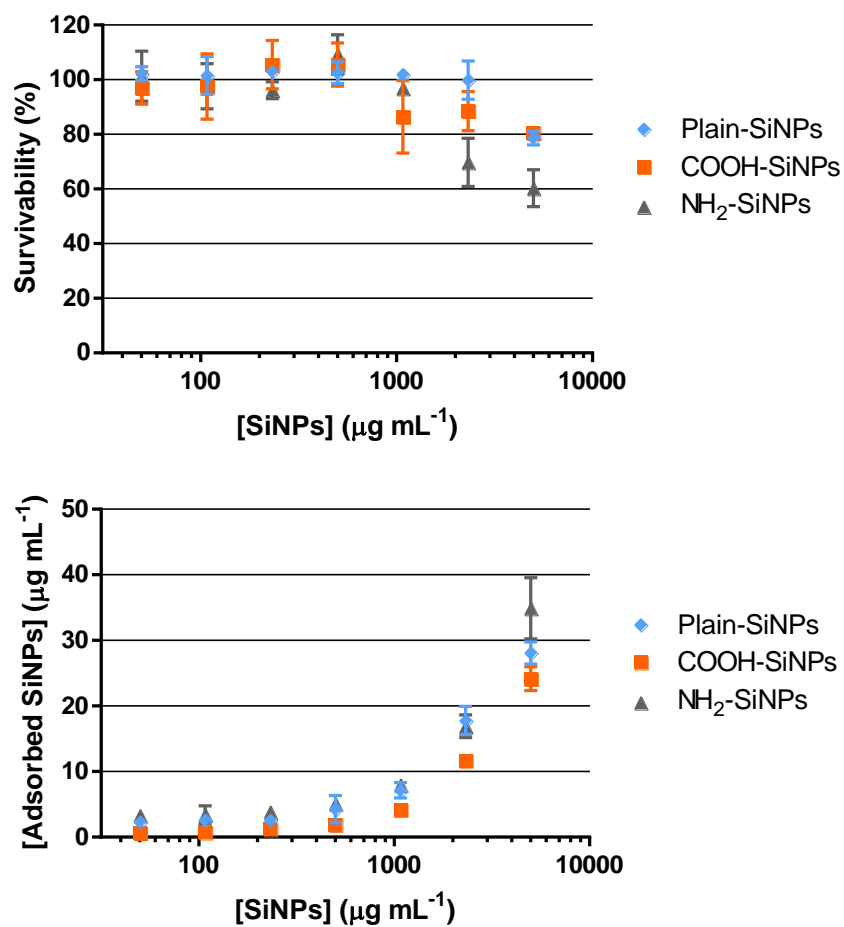
Figure 19. Toxicity of differently coated 200 nm SiNPs on RBCs. (A) Red blood cell survivability at different concentrations of SiNPs. Only concentrations above 1 mg mL-1 show a decrease of RBC survivability. (B) Relation between the number of SiNPs attached to the RBCs and the concentration of SiNPs applied.

4.2.   Population analysis of RBCs interacting with SiNPs

To further understand how the interaction affects the cells, RBCs were mixed with the highest (COOH- SiNPS) and lowest negatively charged nanoparticles (NH$_2$-SiNPs) and imaged using brightfield microscopy. A monolayer of RBCs was created by compressing a droplet in between a quartz slide and a glass slide and cells were imaged once they became immobile on the surface (Figure 20).
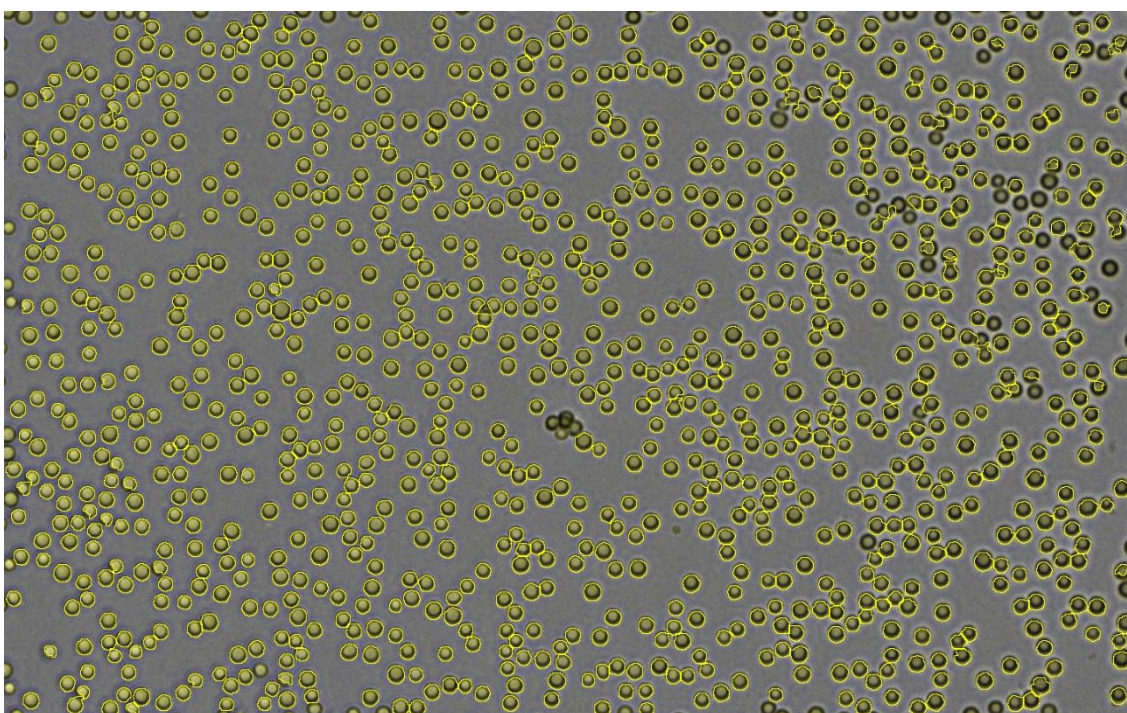
Figure 20. Example image of RBCs mixed with SiNPs and imaged via brightfield microscopy. The yellow outline represents the measurements of individual RBCs for this image.

Each experimental set resulted in agreeing data points within the same set but varied between both sets. This difference still holds for the control samples prepared in the absence of SiNPs, indicating a problem with the imaging setup. As the imaging microscope was adjusted from a freeze-drying microscope, it became apparent that small changes in the sample position and/or position of the objectives likely caused a drift of the focal plane and changed the image calibration. Due to the sensitivity of the imaging system and the necessity to visualize the SiNPs, which was impossible using brightfield microscopy, it was decided to image the samples with LSCM.

Due to being based on fluorescence emission, LSCM has a much higher signal-to-ratio than brightfield microscopy, allowing the user to attain higher resolution images. It also allows 3D

imaging of samples immobilized on a surface. Initial strategy for sample preparation aimed at immobilizing RBCs on a glass slide using methanol fixation. Even though it is a standard method for analysis of blood smears in histopathology, methanol fixation causes RBCs to loosen their 3D conformation and become flat (Figure 21). Other fixation methods also risked hampering RBC morphology and elasticity and were, therefore, excluded. Ultimately, to avoid hampering cell morphology, cells were imaged in standard imaging media, while the cells remained suspended in solution.
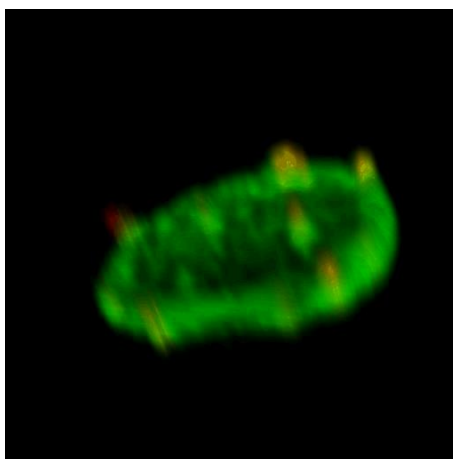
Figure 21. Example of a 3D reconstruction of a RBC after fixation with methanol. RBC membrane was labelled in green, while SiNPs-are labelled in red.

As RBC's are non-adherent cells, introduction of shear flow in the imaging chamber causes cells to continuously drift, which, in turn, causes distortions in the acquired image (**Error! Reference source not found.**). Other approaches to 3D imaging of moving objects usually aim at increasing scanning speed to cancel the object's movement[69]. Herein, I present a high-throughput post-processing method which can be applied to any confocal microscope and computer hardware[70].

In order to reconstruct the RBCs, a mask for each object is first created considering only the channel which depicts the labelled RBCs. Images are first filtered using a "median" filter, and a mask is created using a "moments" algorithm. The resulting mask is then expanded and filled via "dilate" and "fill holes" functions, respectively, available in ImageJ. Small objects present in the mask are excluded under the assumption that they constituted mainly debris. All previous steps are applied to each individual frame across the entire z-stack. 3D objects are connected and identified via overlapping sections in neighboring z-steps, using 3D object counter[71]. Individual objects are then considered sequentially by removing the remaining information from the mask and applying it to the original image. This results in a z-stack containing a single object (this may contain either single cells, or multiple adjacent cells).
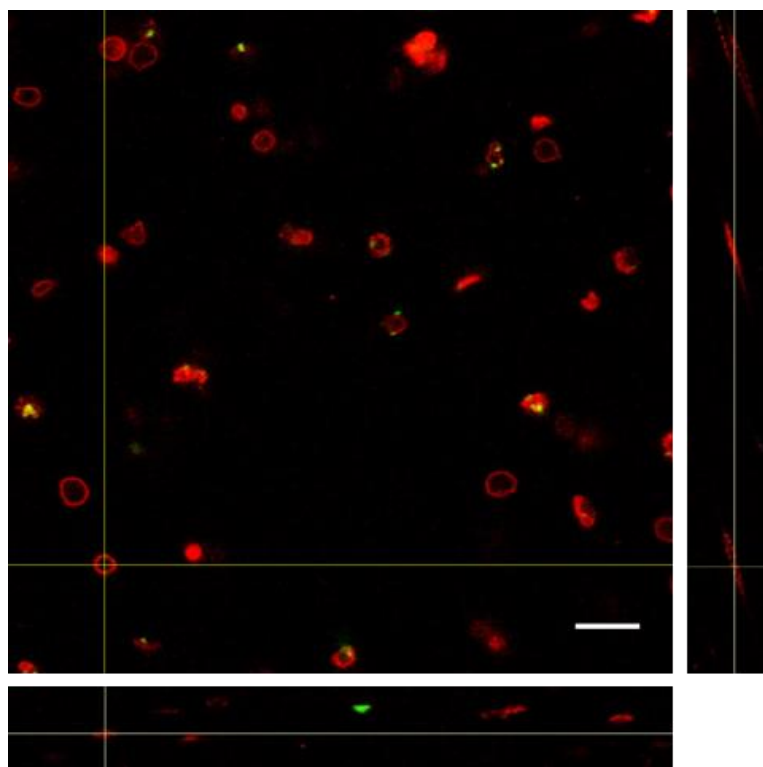
Figure 22. Orthogonal view of a raw acquisition of 3D stack of RBCs with SiNPs. XZ and YZ views show distortion of the cell caused by their movement. Cell membrane is labelled in red, while SiNPs are labelled in green. Error bar represents a 10 μm distance.

Upon attaining the image containing a single object, the z-dimension is defined as time, allowing the image to be aligned via the "correct 3D drift" plugin. Application of the plugin is only possible at this point due to previous steps limiting the amount of data present in the image. Upon realignment, the original dimensions are restored resulting in the aligned 3D stack containing a single object, which can then be analysed using 3D object counter, and exported to other software for further analysis.

In summary, using the previous described method (Figure 23), it was possible to reconstruct the 3D structure of single cells slowly drifting in solution during the acquisition of fluorescent images using a combination of (1) identification of the 3D object along the z-axis and (2) correction for the flow of the center of mass of the object (Figure 24). This method can be applied to each imaged cell automatically and, as such, it is able to provide accurate statistics to describe the population(s) of RBC's. As a result of the analysis, 3D reconstructed RBC's with and without fluorescent SiNPs have been obtained. To achieve a successful reconstruction, a cell has to move less than a radius (from its starting position) in between scanning steps. In this case, this was obtained when a cell was moving at less than 0.15 μm s^{-1}. This limitation highlights the importance of optimizing the imaging settings not just for image quality but also for acquisition speed, as faster acquisitions will allow the reconstruction of faster moving RBCs, whereas slowing the acquisition speed will likely improve image quality. .
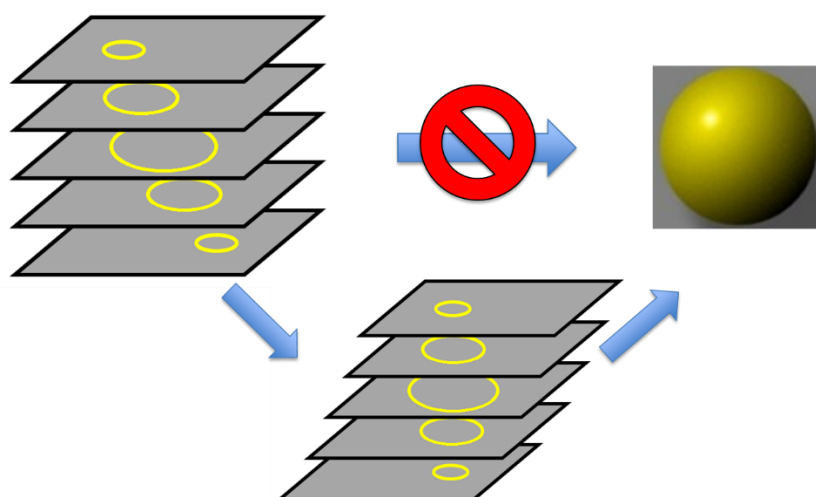
Figure 23. Schematic representation of the approach used to reconstruct 3D objects based on the deformed images obtained via LSCM. Direct reconstruction of the objects is not possible requiring
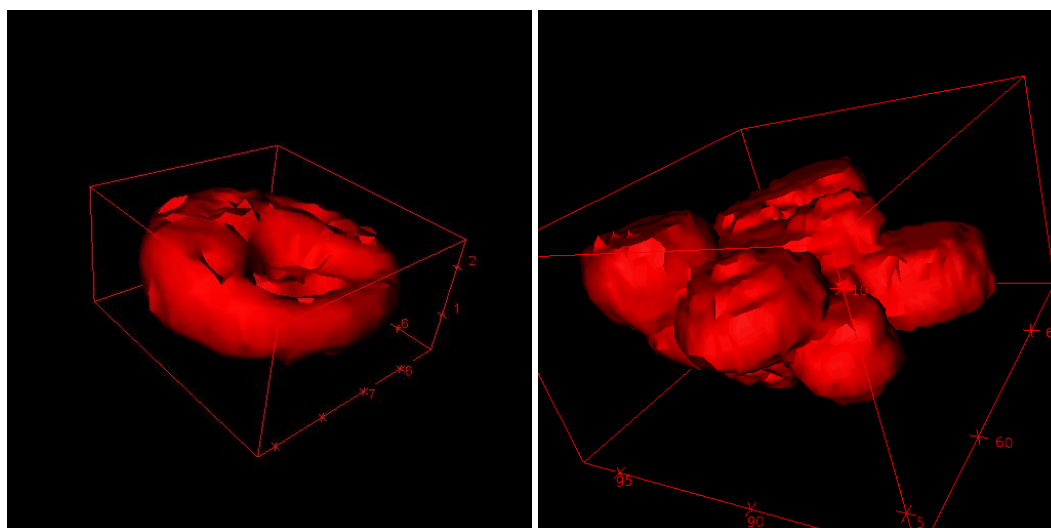
Figure 24. 3D surface reconstruction of a RBCs after alignment. The outer limit of the cells was rendered in 3D. The figure on the right highlights the possibility of reconstructing large objects composed of multiple cells, even if in the scope of this work these were excluded from the analysis.

Multiple channels can be analyzed parallelly, hence NP clusters could be visualized in conjunction with the RBC's (Figure 25). However, due to the resolution of the microscope it was not possible to distinguish individual NPs from NP clusters. As such, NP clusters are considered to be consisted of one or more NPs. It should be noted however that LSCM is able to distinguish the NP cluster's position in regards to the cell membrane, i.e. whether or not a cluster has crossed the membrane into the cytosol, or remains attached to it (Figure 26).
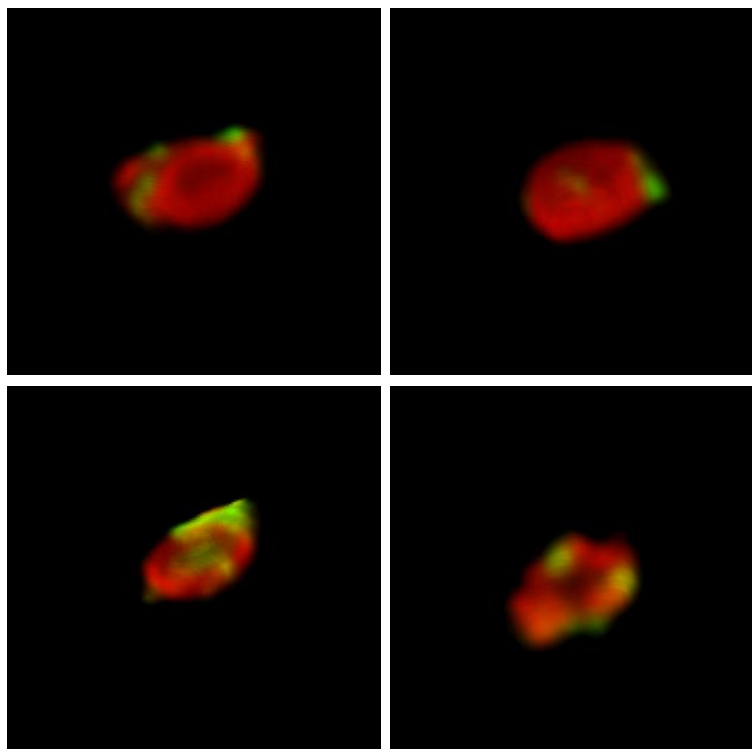
Figure 25. 3D Volume reconstruction of RBCs with SiNPs adsorbed onto the surface. The cell is reconstructed based on the intensity of the signal acquired. This allows visualization of multiple signals in contrast to surface-only visualization.

In order to obtain a complete 3D reconstruction of the cell, the flow should be slow enough to allow a partial overlap of the same cell at different z-planes. Under standard conditions reported in this work, RBC 3D reconstruction could be achieved at flow speeds under 3 µm per z step of the microscope.
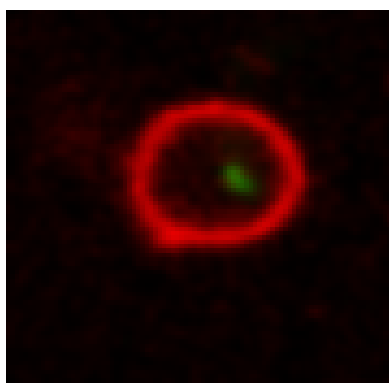
Figure 26. Rare occurrence of a negatively charged SiNP inside a RBC.

The concentration of NPs plays an important role in the attachment of NPs to the RBC's membrane. An increase in the concentration of NPs is associated with a higher distribution of the nanoparticles across the available RBC's. Interestingly, NPs do not seem to cover the surface uniformly, but rather form clusters at the RBC surface (Figure 25).

The number of clusters observed at the surface depends on the type of particle (Figure 27). Plain SiNPs show an average of 0.42 clusters per cell at 5 mg mL^{-1}. While this number seems quite small, larger concentrations of SiNPs cause lysis of the cells. For the highly negatively charged COOH-SiNPs the number of attached SiNP cluster is similar, remaining at 0.5 clusters per cell even at 5 mg mL^{-1}. In contrast, the NH$_2$-SiNPs have an average of 2.1 clusters per cell, with most of the cells being covered by NPs. These results suggest the attachment of SiNPs is dependent on their surface charge, as the least negatively charged NH$_2$-SiNPs are present on the surface of RBC's on a much larger scale than either plain-SiNPs or COOH-SiNPs.
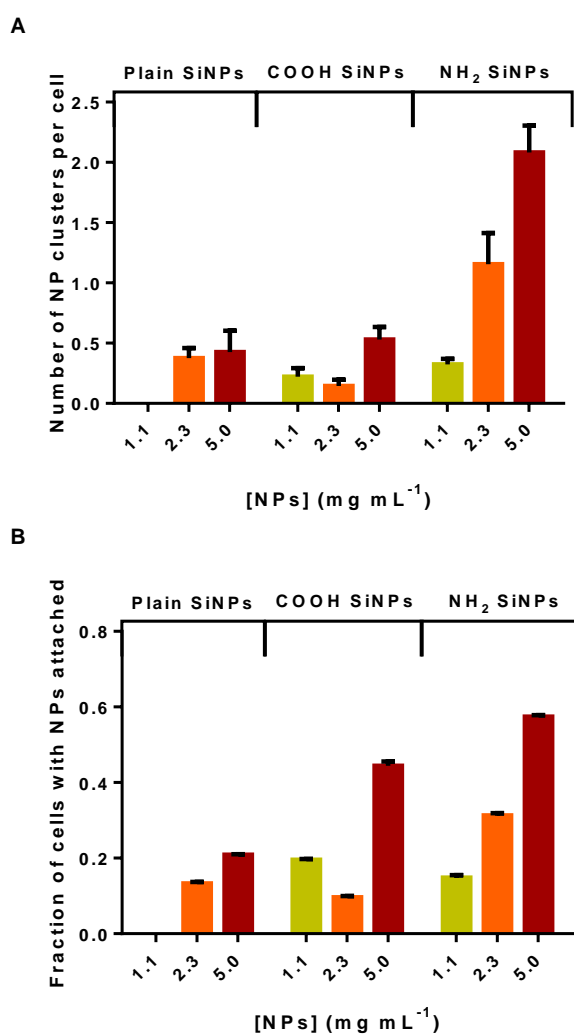
Figure 27. (A) Average number of SiNP clusters attached to single RBCs and (B) fraction of cells containing at least 1 SiNP cluster. RBCs were reconstructed and individually analyzed for the presence and number of SiNP clusters. Results are shown as average and SEM.

Comparing the results with the toxicity described earlier, there is a correlation between the amount of SiNP clusters adsorbed onto the RBC membrane and their disruptive power. Samples with higher number of SiNP clusters adsorbed are related with higher toxicity, while samples with similar number of SiNP clusters per cell, also show the same tendency, p.e. both

plain SiNPs and COOH-SiNPs present similar values for number of SiNP clusters attached while also presenting similar values for toxicity.

When analyzing the shape descriptors for the different samples, for all types of nanoparticles no clear sign of disturbance is observed (Figure 28). While average values are within the expected range for healthy RBCs, it is not clear whether they retain their elasticity and deformability.
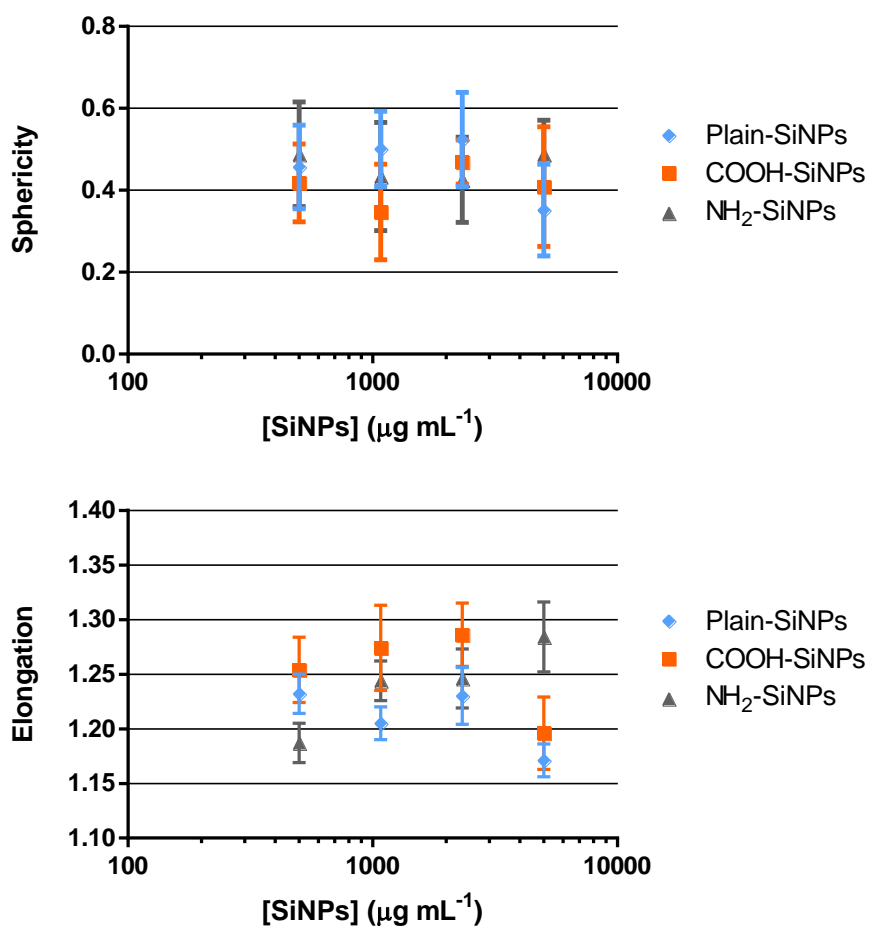
Figure 28. Morphological analysis for sphericity (top) and elongation (bottom) of RBCs interacting with differently charged SiNPs. Samples show no statistically significant differences when compared amongst themselves and with the control sample (Sphericity$_{control}$=0.482±0.071; Elongation$_{control}$=1.218±0.033)

4.3.   SiNP interaction with GUVs

To demonstrate the generic applicability of this study, and as a collaboration with Dr. Jean-Baptiste Fleury from University of Saarlandes, the interaction between the same types of nanoparticles and Giant Unilammelar Vesicles (GUVs) was investigated. GUVs can be considered a model system for RBCs, while being less rigid and not having a glycocalyx layer surrounding the membrane. Fluorescent GUVs were prepared using a DOPC/DOPS mixture supplemented with 8% PS lipids to provide a negative electrostatic charge to the vesicles. Upon addition of Plain- and NH2-SiNPs, they begin attaching to the surface of the GUVs, though it is not known whether this effect is reversible or not. COOH-SiNPs however do not seen to attach to the GUVs (Figure 29). When measuring the GUV morphology over time, it is observable that plain-SiNPs do not cause shape distortions of the GUV. On the other hand, both the NH2-SiNPs and the COOH-SiNPs cause a strong disturbance of the membrane (Figure 30).
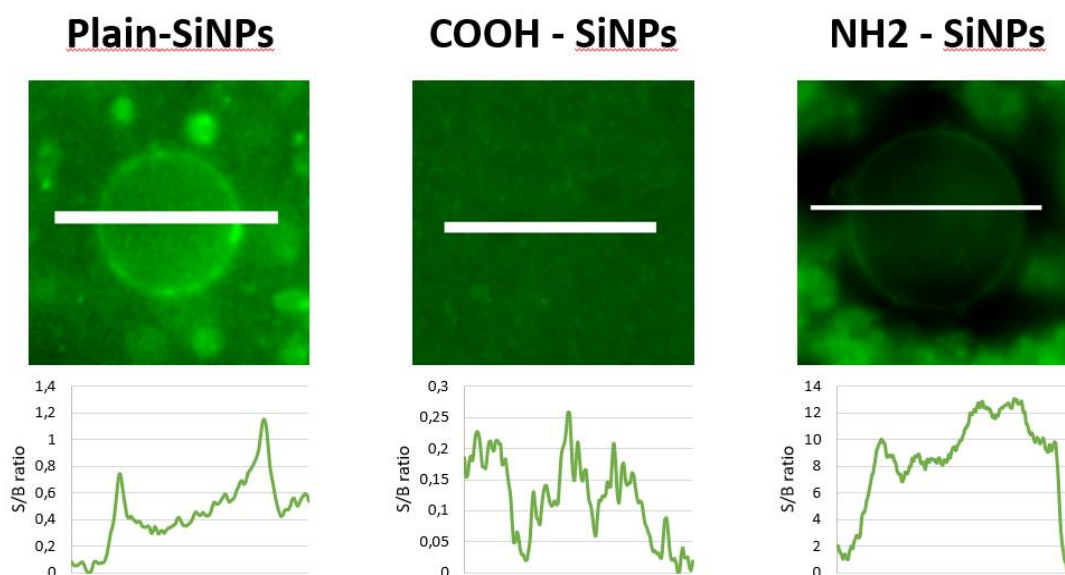
Figure 29. Fluorescence microscopy images (top) and corresponding line scans (bottom) of a GUV when in contact with different SiNPs throughout a brief period of time. SiNPs are labelled in green, while GUVs are not labelled. Line scans measurements are represent according to the signal-to-background (S/B) ratio.
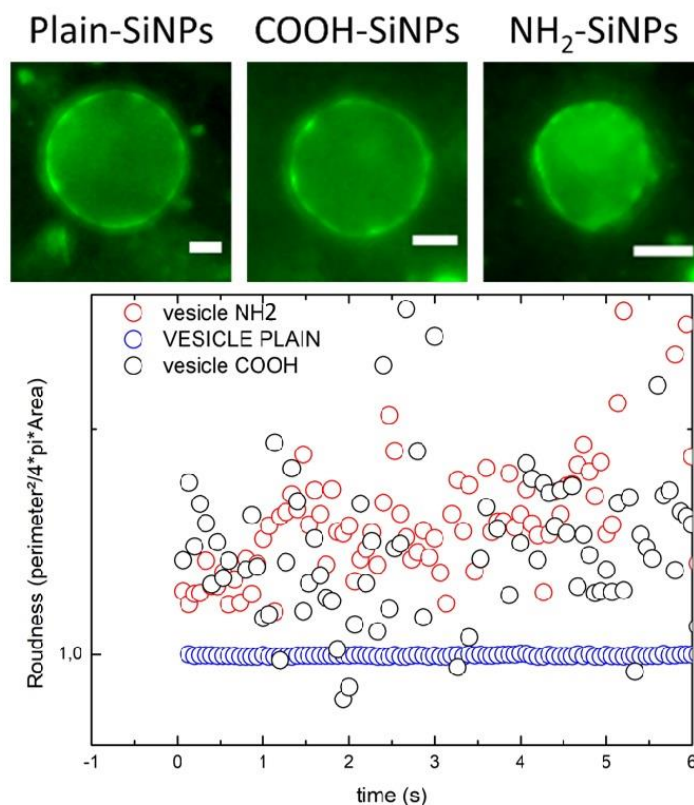
Figure 30. Fluorescence microscopy images (top) and corresponding roundness measurements (bottom) of a GUV when in contact with different SiNPs throughout a brief period of time. GUVs are labelled in green, while SiNPs are not labelled. Scale bar represents a 10 μm distance.

Unlike what is observed on RBCs, SiNPs interacting with GUVs are distributed in a more uniform manner and not under the form of clusters. This might indicate that flow conditions under which the RBC experiments were performed triggered the clustering of the SiNPs. The most negatively charged particles, COOH-SiNPs, do not attach to GUVs, while on RBCs, they presented a similar behaviour to the plain-SiNPs. As with RBCs, NH2-SiNPs show the strongest attachment to GUVs, which is consistent with literature data. These different behaviours may be due to a structural difference between the vesicle (fluid membrane) and RBCs (elastic membrane) and the glycocalyx layer surrounding the RBCs.

Despite the different adsorption behaviours by NH_2- and COOH-SiNPs, both types of NPs induce a strong disturbance of the GUV membrane, while plain-SiNPs do not disturb the membrane. While in the case of NH2-SiNPs, these distortions can be justified by the attachment of SiNPs, the same justification does not apply to COOH-SiNPs. A better attempt to explain the latter would be to consider electrostatic repulsion between the vesicles and the COOH-SiNPs, this question still requires further investigation.

5. Future perspectives

Despite the work described in this thesis, several questions remain unanswered. The first part of the work described the determination of freezing and thawing point but did not fully explore the mechanisms which lead to a hysteresis of the freezing point. In this regard, it is possible that, due to the small volume of the sample, it undergoes a vitrification process, leading to an amorphous phase. This process could be clarified via differential scanning calorimetry, as it can be expected the crystalline structure displays a different heat capacity relatively to its amorphous counterpart. Understanding of this process will lead to further optimization of existing protocols, namely for alternative cryoprotectants such as trehalose.

In chapters 3.2, the question of the influence of aging on the cryopreservation of RBCs was also raised. The understanding of this influence is vital for the optimization of current protocols both for RBC cryopreservation studies and for clinical environments. Even though the benefits of current methods vastly outperform possible drawbacks, it is important to minimize the latter. It is known that protein composition on the membrane of red blood cells changes with age, being one of the mechanisms allowing the identification of old RBCs for renewal by our body. Relating the protein composition at different points in time with the survival rate of cells after a freeze-thawing cycle will provide clues on which proteins affect this process, either by stabilizing the membrane during freezing or, in contrary, by destabilizing it. Such knowledge can be applied to improve cryopreservation protocols by incorporating stabilizing proteins in the system.

Population studies in chapter 3.3 have shown an increase in RBC size after a freeze-thawing cycle. It is not clear the effect of this change on the function of RBCs, and more information is required on the molecular alterations which lead to this increase, namely alterations to the membrane structure, composition, permeability and lipid spacing. It is also important to analyse RBCs rheological properties as these are vital towards their function. It should be noted that the benefits of using cryopreserved RBCs heavily outweigh the risks, thus even if their function is partially impaired, it is not expected this will modify existing protocols.

Chapter 4 explores the interaction of SiNPs with RBCs, as potential co-agents for the delivery of trehalose. During the scope of this project it was not possible to evaluate the internalization of trehalose or other small molecules, so this would be a logical next step. It was also not possible to measure their rheological properties, so techniques such as micropipette suction would provide valuable information in this regard.

Chapter 4.3 shows the use of GUVs as model systems for RBCs. Here, it was shown that SiNPs attach in a uniform manner to the surface of GUVs, suggesting they follow a Langmuir

adsorption model. However, in chapter 4.2 it was shown that SiNPs attach as clusters to the surface of RBCs, arguing for a different adsorption model. While determination of adsorption isotherms in RBCs may be complicated in solution due to the high concentration of SiNPs required, it would be possible to do so by immobilizing the RBCs on the surface thus limiting the volume of sample required. Understanding the adsorption mechanism would contribute towards increasing our knowledge on the influence of the glycocalyx on the attachment of SiNPs to RBCs.

Finally, the high-throughput image alignment method described in chapter 4.2 is not limited to the study of RBCs with a single type of NP or to LSCM images. First, relatively to the image acquisition methodology, this post-processing method simply requires a z-stack as an input. Thus, it can be directly applied to different imaging methods which can produce this output (e.g. widefield deconvolution microscopy, spinning disk confocal microscopy, light sheet fluorescence microscopy). Second, it works identifying the objects in the channel showcasing the cell membranes and using these to align the remaining channels. In this work, the first channel corresponded to labelled RBCs, but it can be expanded to other suspension cells (e.g. monocytes, leukocytes). Furthermore, in a raw sense, the remaining channels correspond to a signal originating from something other than the dye in the membrane, and not necessarily to NPs. This means that the same method can be directly applied to the study of membrane proteins on suspension cells or other external objects so long as they emit fluorescence or can be labelled with a fluorescent dye. In principle, more than two channels can be used for imaging, with the only limitations set during the sample preparation and image acquisition steps. This last point highlights the possibility to not only study the interaction of NPs with the membrane, but also the correlation between different objects (e.g. to study the modulation of certain membrane proteins upon interaction with the membrane. In short, the proposed method, presents an easy option which can be applied to multiple systems, without requiring expensive improvements to existing microscopes.

6. Conclusions

This thesis describes different strategies for cryopreservation of red blood cells (RBCs): chapter 3 is focused on application of trehalose for the cryopreservation of RBCs, and chapter 4 study the interactions of SiNPs with RBCs for future application as co-agents for trehalose delivery. In particular, In chapter 3, I have presented an improvement to current methods for determining the freezing and melting points of blood by applying post-processing image analysis to the images obtained via freeze-drying microscopy. This method uses pixel intensity profiles throughout time as the sample is frozen and molten to remove the user from the analysis, obtaining a fully analytical method and allowing to obtain more precise measurements. This method has been validated only for blood samples, however it offers the possibility of being applied to other samples, while also allowing the process to become fully automated.

Freezing and thawing conditions as well as buffer composition were analyzed according to their influence of the survivability of RBCs. These conditions play a major role in the preservation of RBCs as ice crystal growth is controlled by them. Very slow freezing rates result in low RBC survival likely due to ice crystals growing too large. Faster cooling rates show better survival rates as ice crystals do not have as much opportunity to grow. Freezing in liquid N2, presents a viable option only when samples are thawed quickly, in a water bath at 37°C. While the reason is not fully understood, it can be suggested that during immersion in liquid N2, the samples undergo a vitrification process instead of crystallization, allowing cells to keep water in the cytosol. Slow thawing methods allow the water to restructure, causing damage to the membrane.

Observation that hypertonic solutions are able to protect RBC's from freezing damage led to the analysis of different buffer parameters on RBC cryosurvival: osmolarity, salt composition, pH, and sugar molecule. While osmolarity and salt composition (NaCl vs KCl) do present a role in protecting RBCs, the presence of trehalose is more impactful than using salt alone. This molecule is also able to outperform similar sugar molecules, suggesting it's a particular effect observable only for trehalose. Effect which is enhanced at lower pH (6.5). The RBC survivability is higher than reported in literature, although this is likely associated to the use of sheep RBCs instead of human RBCs. The use of trehalose presents a viable alternative to glycerol for cryopreservation of RBCs, not requiring such high concentrations of the cryoprotectant and possibly allowing to bypass the cryoprotectant removal step, due to it being metabolized in the body.

Lyophilization of RBC samples was attempted using different buffer compositions. This strategy offers the advantage of not requiring cold storage, facilitating not only storage but also

transport. Nonetheless, all the conditions tested resulted in the bursting of the RBCs and oxidation of hemoglobin. While promising, the drawbacks of the method do not allow for its implementation, requiring more understanding of the membrane phase shifts or redox reactions during the drying and reconstitution steps.

In chapter 4, and in order to study the effects of differently charged SiNPs on RBC, three types of SiNPs were added to RBC samples. These NPs show signs of toxicity at concentrations higher than 1 mg/mL (survivability decreases by 20%), whereas the effect is further enhanced (survivability decreases by 40%) when using NPs with a lower negative charge, SiNPs-NH2. This suggests the toxicity is related to stronger interactions between the SiNPs and the negatively charged cell membrane. As per fluorescence intensity measurements, the decrease in survivability is also associated with an increase in the concentration of SiNPs adsorbed, providing further evidence of these interactions.

In order to visualize the RBCs as to measure any deformations, two strategies were attempted: first, by brightfield microscopy, using an adapted freeze-drying microscope; and second, by LSCM, in order to acquire more precise and 3-dimensional data. Due to imperfections in the data acquisition steps, the use of brightfield microscopy was abandoned in favor of more precise measurements acquired via a LSCM microscope. For the analysis of the acquired 3D images of floating RBCs, a high throughput image analysis method was developed allowing the XY alignment of individual objects across the Z-axis of the image, and which has been published in Dias et al, Nanoscale, 2019 (annex I)[70]. Additionally, the method allows the alignment of multiple channels, enabling labelling multiple compounds and distinguishing the position of each signal to the cell.

When incubated with RBCs in solution, NPs distributed under the form of clusters. The average number of clusters found on each cell is higher for lower negatively charged nanoparticles, hinting at the major role of surface charge in this interaction. Despite the number of identified clusters attached to RBCs, the cells did not exhibit morphological changes when compared to a control sample in the absence of SiNPs. This seems to point that despite the attachment of RBCs, cells retain their structure and deformability potential. Nonetheless, the results must be taken with a grain of salt, as the high deformability of RBCs may hide potential variations in the parameters analyzed. The results were confirmed with a experimental model system, GUVs with a lipid composition mimicking that of RBCs. These experiments show a similar behavior in that weakly negatively charged SiNPs, SiNPs-NH2, display a stronger attachment in comparison with the remaining similar sized SiNPs. However, when attaching to GUVs, SiNPs do not adsorb as clusters, suggesting the glycocalyx may play a more important role than initially considered.

Overall, as long as below the 1 mg/mL threshold, SiNPs are a stable component, not showing clear signs of toxicity to RBCs. This enables further applications to be developed by making use of SiNPs as nanocarriers, while using their surface charge to tailor the interaction strength to RBCs. The alignment method published may also see application in other biological samples, like suspension cells, to locate fluorescent proteins expressed or other labelled compounds.

7. Materials and Methods

Red Blood Cells: RBCs were isolated from fresh whole sheep blood supplied in Alsever's medium (TCS Biosciences Ltd, UK) and kept at 4 °C. Before use, RBCs were washed twice by centrifugation at 500g and exchanging media with phosphate-buffered saline (PBS), and adjusted to 40% hematocrit.

Incubation media: 3x Phosphate Buffered Saline (PBS) solutions were prepared by dissolving PBS tablets in AnalaR water. Subsequent dilutions were prepared by diluting the 3x PBS solution in AnalaR water. Trehalose, glucose and sucrose solutions were prepared by dissolving the specific compound in 1x PBS. Afterwards, the pH of the medium was adjusted with NaOH/HCl using a digital pH meter (FE20, Mettler Toledo, Switzerland). Finally, the osmolarity was measured using a Type 13/13DR osmometer (Löser Messtechnik, Berlin, Germany). All chemicals were acquired from Sigma-Aldrich, UK.

Freeze-thawing curves: After washing and medium exchange with the appropriate solution, a RBC droplet was imaged using a Lyostat5 (BTL, UK). The temperature was decreased until -30 °C and then increased up to 25 °C (room temperature) while keeping the chamber at 1 atm. Cooling and heating rates were slowed down close to the freezing and melting points and imaging rate was increased in order to increase the sensitivity of the measurements. Images were exported and analyzed using FIJI, a distribution of ImageJ. Data was then transferred and analyzed using Microsoft Excel.

RBC freeze-thawing: After washing and exchanging media for the appropriate solution, samples were frozen according to 3 different protocols: flash-freezing, by immersing the samples in liquid N_2; medium cooling, by storing the samples in a pre-cooled freeze-drier at -40 °C; and slow cooling, by using a freeze-drier to reduce the temperature by -0.5 °C / min down to -40 °C. Samples were kept at – 40 °C for 4 hours, followed by storage overnight at -80 °C. For thawing, samples were thawed according to 4 different protocols: using a water bath at 37 °C; allowing the samples to rest at room temperature; using a freeze-dryer to increase the temperature by 0.5 °C / min, from -40 °C to 25 °C; and by storing the samples in a 4 °C fridge.

Hemolysis assay: Hemolysis assay was performed by diluting the RBCs samples in MQ Water (5 µL sample: 95 µL MQ water) in a Greiner 96-well plate. This causes RBCs to lyse due to osmotic pressure, thus releasing intracellular hemoglobin to the medium. Fluorescence intensity (λex =

550 nm; λem = 627 nm) and absorbance spectra (500 nm to 800 nm, with increments of 2 nm) were recorded using a Tecan Infinity m200 microplate reader. Hemoglobin (Hb) concentration is calculated by taking into account the different contributions of the its different forms to the final UV-Vis spectrum as described in Benesch *et al*[71]. Ultimately the survivability is defined as a ratio between the Hb concentration in the sample and the Hb concentration in an untreated control.

$$Survivability(\%) = \frac{[Hb]_{sample}}{[Hb]_{untreated}} \cdot 100$$

The concentration of adsorbed nanoparticles was determined by comparing the fluorescence emission of the sample to known standards previously prepared. This comparison assumes that after cell lysis particles become homogenously suspended in solution and no other component acts as a quencher for the conditions used.

RBC's morphology measurements: For imaging, RBC's smears were prepared using a coverslip and covered. The sample was imaged using a Lyostat5 (BTL, UK), which had been set up as a brightfield microscope by removing the polarizer and analyzer disks. The pixel size was determined for a 50x objective using a calibration slide. During image acquisition, a background image was acquired (either by direct acquisition or by processing different background images as required) and background correction was performed by dividing the sample image by the background image. This allowed to correct artifacts present in the images, while improving overall image quality, as seen in Figure 31.
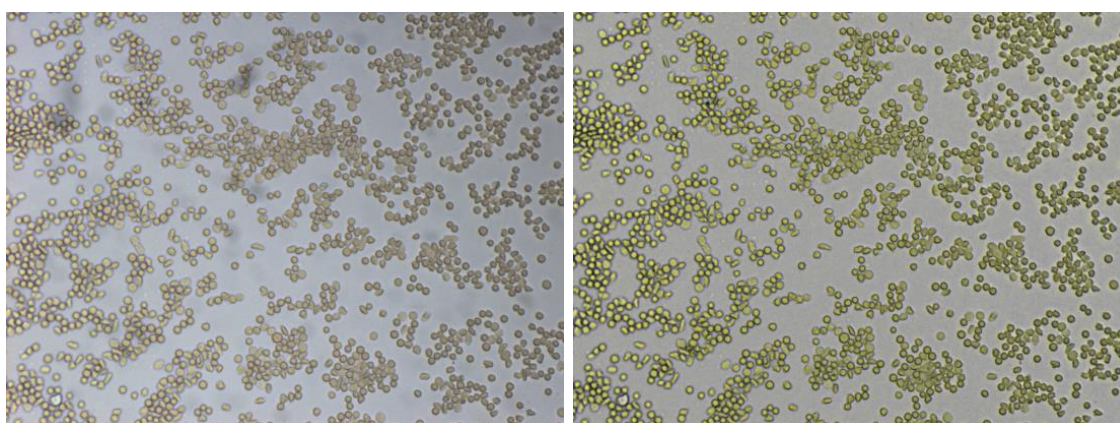
Figure 31. Micrograph of sRBC's suspended in 3x PBS solution before (left) and after background correction (after).

A mask for the individual selection of RBCs was created by applying a "mean" thresholding algorithm available on the the FIJI distribution of ImageJ, followed by a watershed. Objects were analysed using the "Analyse Particles" function available in the same software. The results were

exported to Graphpad Prism where frequency histograms were plotted according to the RBCs' size and a Gaussian fit was applied to describe the sRBC's population. RBCs diameter was calculated by assuming RBCs as circles, and, as such, their radius as a function of the area occupied.

RBC lyophilization: After washing, RBCs' medium was exchanged to the appropriate solutions previously used for cryopreservation experiments. Samples were frozen by immersion in liquid N_2 and immediately transferred to a pre-cooled to $-40\,°C$ freeze drier. After, they were kept in a vacuum at -40 °C for 2 days, after which they were removed and stored at room temperature. Samples were reconstituted using PBS solution. The RBC powder was imaged prior to sample reconstitution using a Lyostat5 (BTL, UK) previously adapted with a 50x objective and by removing the polarizer and analyzer disks.

Fluorescent SiNPs: Amorphous, fluorescent and spherical "red-Sicastar" SiNPs of 200 nm were purchased from Micromod Partikeltechnologie GmbH. These particles are prepared according to the hydrolysis process. The advantage of this process is that the fluorescent molecules are dispersed in the bulk of the NPs and their presence at a surface is marginal. They have a hydrophilic surface functionalized with terminal Si-OH bonds (i.e. plain silica). In order to compare the effects of the surface properties of NPs, fluorescent SiNPs with different groups were used: -NH2 (weakly negatice) or -COOH (strongly negative).

Incubation with SiNPs: Nanoparticle suspensions were prepared by diluting the nanoparticles in PBS. Previously prepared RBCs were split into 0.5 mL aliquots, centrifuged at 500g for 5 min and resuspended in the nanoparticle suspension. Samples were kept at 37°C in an orbital mixer overnight at 15 rpm. Before analysis, RBCs were washed by centrifuging at 500g for 5 min and resuspending in PBS.

Brightfield microscopy: After incubation with nanoparticles, samples were immediately diluted in PBS (1:50 ratio) and inserted in a Countess™ Cell Counting Chamber Slide. Cells were allowed to deposit for 5 min and imaged with a Lyostat5 Freeze Drying Microscope adapted for brightfield microscopy by removal of the polarizer and analyzer filters.
Images were analyzed using Fiji as described in chapter 1, while using a "Moments" filter to create the segmentation mask.

Laser Scanning Confocal Microscopy: Glass slides were washed with MQ water, 70% ethanol and isopropanol and dried under N_2 stream. A temporary chamber on the glass slide was created using silicone spacers to allow handling the samples. Slides were coated with Collagen type IV (Sigma Aldrich, St Louis, USA) by incubating with 3% solution (w/v) for 30 min and removing excess by washing three times with PBS. Samples were then diluted in PBS (1:10 ratio) and 300 µL were transferred into the chamber and allowed to deposit for 30 min. Excess RBCs were removed by washing twice with PBS.

RBC membrane was labelled by incubating the samples with 5 µg/mL WGA-AF488 in PBS for 10 min and removing excess by washing twice with PBS. The silicone spacer was then removed and slides were mounted using Ibidi Mounting Medium.

Samples were imaged using a Leica SP5 Laser Scanning Confocal Microscope equipped with an Ar laser and a 561 diode laser, and a 63x magnification objective (oil, N.A. 1.4). Pinhole was set to 1 airy and image magnification was set to 2.4x (pixel size ~100 nm), interplane distance was optimized using the microscope software (~340 nm voxel height). Images were acquired using resonant scanner mode to decrease acquisition time; and using line sequential scanning, to remove cross-talk between the different channels, with a line average of 8 times, to decrease background noise.

3D reconstructions followed by morphological analyses of the RBCs were performed using a custom script for FIJI. Results were exported as comma separated values (csv) files and RBC populations were described by performing a gaussian fit via a custom python3 script.

Giant unilamellar vesicles' preparation: Giant Unilamellar Vesicles (GUVs) were grown following the protocol of Angelova et al[74] Briefly, 20 µl of a 1 mM lipid stock solution (DOPC/DOPS/Rho-DOPE, 91.2 : 8 : 0.8 mol%) in chloroform (Sigma) were dried on an ITO glass slide (Delta Technologies) under vacuum and rehydrated with 2 ml of 200 mM sucrose (Sigma). GUV formation was performed at 8 Hz and 1.1 V for 2 h. The GUVs were then mixed with 0.1 mg ml^{-1} of fluorescent SiNPs and introduced by capillarity into a microfluidic chamber. The vesicles and the NPs were observed under an epifluorescence microscope (Zeiss Axio Observer.Z1) with two different excitation wavelengths (blue laser 493 nm and green laser 531 nm). To fabricate the observation chambers with a flat bottom, glass slides were cut into squares of about 2.5 × 2.5 cm and coated with octadecyltrichlorosilane (OTS, purchased from Sigma) to prevent GUV adhesion.25,26 The OTS-coated glass squares were stacked with a cover slide (thickness 150 µm) as a spacer and glued together at three sides using epoxy glue.

GUV shape analysis: The shape of GUVs was analyzed automatically using ImagePro Plus10 as commercial image processing software (Media Cybernetics).

Lipids: Phospholipids: dioleoyl-phosphatidylcholine (DOPC), dioleoylphosphatidylserine (DOPS), 1,2-dioleoyl-sn-glycero-3-phosphoethanolamine-N-(lissamine rhodamine B sulfonyl) (Rho-DOPE), 1,2-dioleoyl-sn-glycero-3-phosphoethanolamine (NBD-DOPE), and 7-nitrobenzofurazan-labeled. All lipids were purchased from Avanti Polar Lipids (USA).

8. References

1. Willis,R. (1847) The works of William Harvey, MD. London, Sydenham Society;
2. Donovan, A.J. (2004) Richard Lower, M.D., physician and surgeon (1631-1691). *World J Surg*. 28, 9, 938-945;
3. Pick, A. "When Was The First Blood Transfusion?" HeartValveSurgery.com 2019. 3 Jan 2009, https://www.heart-valve-surgery.com/heart-surgery-blog/2009/01/03/first-blood-transfusion/;
4. Ellis, H. (2007) Surgical Anniversaries: James Blundell, pioneer of blood transfusion. *Brit J Hosp Med*. 68, 8;
5. "Karl Landsteiner – Facts". NobelPrize.org. Nobel Media AB 2019. 26 Feb 2019, https://www.nobelprize.org/prizes/medicine/1930/landsteiner/facts/;
6. Tissot, J.-D., Bardyn, M., Sonego, G., Abonnenc, M., Prudent, M. (2017) The storage lesions: From past to future. *Transfus Clin Biol*. 2017, 24, 3, 277-284;
7. Pelis, K. (2001). Taking Credit: The Canadian Army Medical Corps and the British Conversion to Blood Transfusion in WWI. *J Hist Med A Sci*. 56 (3): 238–277;
8. Gibson 2nd, J.G., Gregory, C.B., Button, L.N. (1961) Citrate-phosphate-dextrose solution for preservation of human blood: a further report. *Transfusion*. 1, 280-287;
9. Bicalho, B., Serrano K., Dos Santos Pereira, A., Devine, D.V., Acker, J.P. (2016) Blood bag plasticizers influence red blood cell vesiculation ratee without altering the lipid composition of the vesicles. *Tranfus. Med. Hemother*. 43, 19-26;
10. Kendrick, D.B. (1964) Blood Program in World War II. Washington: Historical Unit of the United States Army Medical Service. *Br J Surg*. 52, 317-317;
11. Hogman, C.F., Hedlund, K., Zetterstrom, H. (1978) Clinical usefulness of red blood cells preserved in protein-poor mediums. *N. Engl. J. Med*. 299, 1372-1382;
12. McQuilten, Z.K., French, C.J., Nichol, A., Higgins, A., David, J.C. (2018) Effect of age of red blood cells for transfusion on patient outcomes: a systematic review and meta-analysis. *Transfus Med Rev*. 32, 2, 77-88;
13. Rogers, S.C., Dosier, L.B., McMahon, T.J., Zhu, H., Timm, D., Zhang, H., Herbert, J., Atallah, J., Palmer, G.M., Cook, A., Ernst, M., Prakash, J., Terng, M.,Roufighi, P., Doctor, R., Said, A., Joens, M.S., Fitzpatrick, J.A.J., Hanna, G., Lin, X., Reisz, J.A. Nemkov, T., D'Alessandro, A., Doctor, A. (2018) Red blood cell phenotype fidelity following glycerol cryopreservation optimized for research purposes. *PLoS One*. 13, 12, e0209201;
14. Rapoport, S., Wing, M. (1947) Dimensional, Oosmotic, and chemical changes of erythrocytes in stored blood. I Blood preserved in sodium citrate, neutral and acid citrate-Glucose (ACD) mixtures. *J Clin Invest*. 26, 4, 591–615;
15. Chang, A., Kim, Y., Hoehn, R., Jernigan, P., Pritts, T. (2017) Cryopreserved packed red blood cells in surgical patients: past, present and future. *Blood Transfus*. 15, 341-347;
16. Mazur, P. (2004) Principle of cryobiology. In: Fuller, B.J., Lane, N., Benson, E.E., editors. Life in the frozen state. 1st ed. Abdingon, CA. CRC Press, p. 3-66;
17. Smith, A.U. (1950) Prevention of haemolysis during freezing and thawing of red blood-cells. *Lancet*. 2. 910-911;
18. Mollison, P.L., Sloviter, H.A. (1951) Sucessful transfusion of previously frozen human red blood cells. *Lancet*. 258, 862-864;
19. Fahy, G.M., MacFarlane, D.R., Angell, C.A., Meryman, H.T. (1984) Vitrification as an approach to cryopreservation. *Cryobiology*. 21, 407-426;
20. Freshney, R.I. (2005) Culture of Animal Cells: A Manual of Basic Technique. 5th ed. New Jersey, USA, Wiley;
21. Satpathy, G.R., Török, Z., Bali, R., Dwyre, D.M., Little, E., Naomi, J.W., Tablin, F., Crowe, J.H., Tsvetkoba, N.M. (2004) Loading red blood cells with trehalose: a step towards biostabilization. *Cryobiology*. 49, 123-136;
22. Lynch, A.L., Chen, R., Dominowski, R., Shalaev, E.Y., Robert, Yancey Jr, R.J., Slater, N.K.H. (2010) Biopolymer mediated trehalose uptake for enhanced erythrocyte cryosurvival. *Biomaterials*. 31, 6096-6103;
23. Stefanic, M., Ward, K., Tawfik, H., Seeman, R., Baulin, V., Guo, Y., Fleury, J.-B., Drower, C. (2017) Apatite nanoparticles strongly improve red blood cell cryopreservation by mediating trehalose delivery via enhanced membrane permeation. *Biomaterials*. 140, 138-149;

24. Scott, K.L., Lecak, J., Acker, J.P. (2005) Biopreservation of red blood cells: past, present, and future. *Trans Med Rev*. 19, 2, 127-142;

25. Franzé, S., Selmin, F., Samaritani, E., Minghetti, P., Cilurzo, F. (2018) Lyophilization of liposomal formulations: Still Necessary, Still Challenging. *Parmaceutics*. 10, 139;

26. Richards, A. B., Krakowka, S., Dexter, L. B., Schmid, H., Wolterbeek, A. P.M., Waalkens-Berendsen, D. H., Shigoyuki, A., Kurimoto, M. (2002) Trehalose: a review of properties, history of use and human tolerance, and results of multiple safety studies. *Food Chem Toxicol*. 40, 871-898;

27. Tang, M., Waring, A.J., Hong, M. (2007) Trehalose-protected lipid membranes for determining protein structure and insertion. *J Magn Reson*. 184, 2, 222-227;

28. Ding, S.-P., Fam, J., Green, J.L., Lu, Q., Sanchez, E., Angell, C.A. (1996) Vitrification of trehalose by water loss from its crystalline dihydrate. *J Therm Anal*. 47, 1391-1405;

29. Zhang, M., Oldenhof, H., Sieme, H., Wolkers W.F. (2017) Combining endocytic and freezing-induced trehalose uptake for cryopreservation of mammalian cells. *Biotechnol Prog*. 33, 1, 229-235

30. (2012) Introduction to Freeze-Drying. V. 2.1. Winchester, UK, BTL;

31. Bensouda, Y., Laatiris, A. (2006) The lyophilization of dispersed systems: influence of freezing process, freezing time, freezing temperature and RBCs concentration on RBCs hemolysis. *Drug Dev Ind Phar*. 32, 941-945;

32. Meryman, H.T. (1966) Cryobiology. 1st ed. New York, USA, Academic Press;

33. Meryman, H.T. (1960) Drying of mammalian cells. *Ann N Y Acad Sci*. 85, 729-739;

34. Goodrich, R.P., Sowemimo-Coker, S.O., Zerez, C.R., Tanaka, K.R. (1992) Preservation of metabolic activity in lyophilized human erythrocytes. *Proc Natl Acad Sci U S A*. 89, 3, 967-971;

35. Sowemimo-Coker, S.O., Goodrich, R.P., Zerez, C.R., Tanaka, K.R. (1993) Refrigerated storage of lyophilized and rehydrated, lyophilized human red cells. *Transfusion*. 33, 4, 322-329;

36. Goodrich, R.P., Spwemimo-Coker. S.O.: Freeze-drying of red blood cells. In: Steponkus, P.L. (1993) Advances in Low Temperature Biology. 2nd ed. London, JAI Press ltd, 53-99;

37. Spieles, G., Heschel, I., Rau, G. (1996) An attempt to recover viable human red blood cells after freeze-drying. *Cryo Letters*. 17, 43-52;

38. Zhao, F., Zhao, Y., Liu, Y., Chang, X., Chen, C., Zhao, Y. (2011) Cellular uptake, intracellular trafficking, and cytotoxicity of nanomaterials. *Small*.7, 10, 1322-1337;

39. Li, J., Mao, H., Kawazoe, N., Chen, G. (2016) Insight into the interactions between nanoparticles and cells. *Biomater Sci*. 5, 2, 173-189;

40. Forest, V., Pourchez, J. (2017) Preferential binding of positive nanoparticles on cell membranes is due to electrostatic interactions: A too simplistic explanation that does not take into account the nanoparticle protein corona. *Mat Sci Eng C*. 70, 889-896;

41. Shang, L., Nienhaus, G.U. (2015) Fluorescent nanoparticle interactions with biological systems: What have we learned so far? *Proc. SPIE*. 9338, 93380M;

42. Chithrani, B.D., Ghazani, A.A., Chan, W.C. (2006) Determining the size and shape dependence of gold nanoparticle uptake into mammalian cells. *Nano Lett*. 6, 4, 662-668;

43. Malugin, A., Ghandehari, H. (2010) Cellular uptake and toxicity of gold nanoparticles in prostate cancer cells: a comparative study of rods and spheres. *J Appl Toxicol*. 30, 3, 212-217;

44. Lu, F., Wu, S.H., Hung, Y., Mou, C.Y. (2009) Size effect on cell uptake in well-suspended, uniform mesoporous silica nanoparticles. *Small*. 5, 12, 1408-1413.

45. Huang, J., Bu, L., Xie, J., Chen, K., Cheng, Z., Li, X., Chen, X. (2010) Effects of nanoparticle size on cellular uptake and liver MRI with polyvinylpyrrolidone-coated iron oxide nanoparticles. *ACS Nano*. 4, 12, 7151-7160;

46. Shang, L., Nienhaus, K., Nienhaus, G.U. (2014) Engineered nanoparticles interacting with cells: size matters. *J Nanobiotech*. 12, 5.

47. Sharifi, S., Behzadi, S., Laurent, S., Forrest, M.L., Stroeve, P., Mahmoudi, M. (2012) Toxicity of nanomaterials. *Chem Soc Rev*. 41, 6, 2323-2343;

48. Ogneva, I.V., Buravkov, S.V., Shubenkov, A.N., Buravkova, L.B. (2014) Mechanical characteristics of mesenchymal stem cells under impact of silica-based nanoparticles. *Nanoscale Res Lett*. 9, 1, 284;

49. Buyukhatipoglu, K., Clyne, A.M. (2011) Superparamagnetic iron oxide nanoparticles change endothelial cell morphology and mechanics via reactive oxygen species formation. *J Biomed Mater Res A*. 96, 1, 186-195;

50. Holt, B.D., Short, P.A., Rape, A.D., Wang, Y.L., Islam, M.F., Dahl, K.N. (2010) Carbon nanotubes reorganize actin structures in cells and ex vivo. *ACS Nano*. 4, 8, 4872-4878;

51. Beck, G.R. Jr., Ha, S.W., Camalier, C.E., Yamaguchi, M., Li, Y., Lee, J.K., Weitzmann, M.N. (2012) Bioactive silica-based nanoparticles stimulate bone-forming osteoblasts, suppress bone-resorbing osteoclasts, and enhance bone mineral density in vivo. *Nanomedicine*. 8, 6, 793-803;

52. Zhang, D., Liu, D., Zhang, J., Fong, C., Yang, M. (2014) Gold nanoparticles stimulate differentiation and mineralization of primary osteoblasts through the ERK/MAPK signaling pathway. *Mater Sci Eng C Mater Biol Appl.* 42, 70-77;

53. Huang, D.M., Hsiao, J.K., Chen, Y.C., Chien, L.Y., Yao, M., Chen, Y.K., Ko, B.S., Hsu, S.C., Tai, L.A., Cheng, H.Y., Wang, S.W., Yang, C.S., Chen, Y.C. (2009) The promotion of human mesenchymal stem cell proliferation by superparamagnetic iron oxide nanoparticles. *Biomaterials.* 30, 22, 3645-3651;

54. Mao, H., Kawazoe, N., Chen, G. (2015) Cell response to single-walled carbon nanotubes in hybrid porous collagen sponges. *Colloids Surf B Biointerfaces*. 126, 63-69;

55. Mu, Q., Du, G., Chen, T., Zhang, B., Yan, B. (2009) Suppression of human bone morphogenetic protein signaling by carboxylated single-walled carbon nanotubes. *ACS Nano.* 3, 5, 1139-44;

56. Duncan, R., Gaspar, R. (2011) Nanomedicine(s) under the microscope. Mol Pharm. 8, 6, 2101-2141;

57. Lu, X., Qian, J., Zhou, H., Gan, Q., Tang, W., Lu, J., Yuan, Y., Liu, C. (2011) In vitro cytotoxicity and induction of apoptosis by silica nanoparticles in human HepG2 hepatoma cells. *Int J Nanomedicine.* 6, 1889-1901

58. Kumar, V., Abbas, A. K., & Aster, J. C. (2015). Robbins and Cotran pathologic basis of disease (Ninth edition.). Philadelphia, PA: Elsevier/Saunders.

59. Brenner, J.S., Pan, D.C., Myerson, J.W., Marcos-Contreras, O.A., Villa, C.H., Patel, P., Hekierski, H., Chatterjee, S., Tao, J.Q., Parhiz, H., Bhamidipati, K., Uhler, T.G., Hood, E.D., Kiseleva, R.Y., Shuvaev, V.S., Shuvaeva, T., Khoshnejad, M., Johnston, I., Gregory, J.V., Lahann, J., Wang, T., Cantu, E., Armstead, W.M., Mitragotri, S., Muzykantov, V. (2018) Red blood cell-hitchhiking boosts delivery of nanocarriers to chosen organs by orders of magnitude. *Nat Commun*. 9, 1, 2684;

60. Kozelskaya, A.I., Panin, A.V., Khlusov, I.A., Mokrushnikov, P.V., Zaitsev, B.N., Kuzmenko, D.I., Vasyukov, G.Y. (2016) Morphological changes of the red blood cells treated with metal oxide nanoparticles. *Toxicol In Vitro*. 37, 34-40;

61. Treuel, L., Jiang, X., Nienhaus, G.U. (2013) New views on cellular uptake and trafficking of manufactured nanoparticles. *J R Soc Interface.* 10, 82, 20120939.

62. Bracht, A., Ishii-Iwamoto, E. L. (2003) Métodos de laboratório em bioquímica. 1st ed. Tamboré, Brazil, Editora Manole Ltda

63. Johnson, I., Spence, M.T.Z. (ed)(2010) TheMolecular Probes® Handbook: A Guide to Fluorescent Probes and Labeling Technologies. 11th ed. Carlsbad, USA, Life Technologies Corporation;

64. "A Brief History of Light Microscopy – From the Medieval Reading Stone to Super-Resolution". Leica Microsystems. Leica Microsystems © 2019. 24 Mar 2019, https://www.leica-microsystems.com/science-lab/a-brief-history-of-light-microscopy-from-the-medieval-reading-stone-to-super-resolution/;

65. "Basic Concepts in Optical Microscopy". Olympus. Olympus Corporation © 2019. 24 Mar 2019, https://www.olympus-lifescience.com/en/microscope-resource/primer/anatomy/anatomy/ ;

66. "Basic Concepts and Formulas in Microscopy". Nikon. Nikon Instruments Inc. 2019. 24 Mar 2019, https://www.microscopyu.com/microscopy-basics ;

67. "Specialized Microscopy Techniques". Olympus. Olympus Corporation © 2019. 24 Mar 2019, https://www.olympus-lifescience.com/en/microscope-resource/primer/techniques/ ;

68. "Lyostat Freeze Drying Microscope". BTL. 2018 Biopharma Process Systems Ltd. 06 Mar 2019, https://biopharma.co.uk/intelligent-freeze-drying/intelligent-freeze-drying/products/lyostat-microscope/;

69. Mikami, H., Harmon, J., Kobayashi, H., Hamad, S., Wang, Y., Iwata, O., Suzuki, K., Ito, T., Aisaka, Y., Kutsuna, N., Nagasawa, K., Watarai, H., Ozeki, Y., Goda, K. (2018) Ultrafast confocal fluorescence microscopy beyond the fluorescence lifetime limit. *Optica*. 5, 2, 117-126;

70. Dias, A., Werner, M., Ward, K.R., Fleury, J.-B., Baulin, V.A. (2019) High-throughput 3D visualization of nanoparticles attached to the surface of red blood cells. *Nanoscale*. 11, 5, 2282-2288;

71. Bolte, S., Cordelières, F.P. (2006) A guided tour into subcellular colocalization analysis in light microscopy. *J Microsc*. 224, 213-232;

72. Parslow, A., Cardona, A., Bryson-Richardson, R. J. (2014) Sample Drift Correction Following 4D Confocal Time-lapse Imaging. *J. Vis. Exp*. 86, e51086;

73. Benesch, R.E., Benesch, R., Yung, S. (1973) Equations for the spectrophotometric analysis of hemoglobin mixtures. *Anal Biochem.* 55, 1, 245-248.

74. Angelova, M. I., Soléau, S., Méléard, Ph., Faucon, J. F., Bothorel, P. (1992) Preparation of giant vesicles by external AC electric fields. Kinetics and apllications. *Trends in Coll Int Sci VI*. 89, 127-131

Annex I

Original article published as a result of the work described in this thesis:

Dias, A., Werner, M., Ward, K.R., Fleury, J.-B., Baulin, V.A. (2019) High-throughput 3D visualization of nanoparticles attached to the surface of red blood cells. Nanoscale. 11, 5, 2282-2288;

Annex I

Nanoscale

Check for updates

High-throughput 3D visualization of nanoparticles attached to the surface of red blood cells†

André Dias, [ID] [a] Marco Werner, [ID] [b] Kevin R. Ward, [ID] [c] Jean-Baptiste Fleury[d] and Vladimir A. Baulin [ID] *[a]

Blood circulation is the main distribution route for systemic delivery and the possibility to manipulate red blood cells (RBCs) by attaching nanoparticles to their surface provides a great opportunity for cargo delivery into tissues. Nanocarriers attached to RBCs can be delivered to specific organs orders of magnitude faster than if injected directly into the bloodstream. Another advantage is a shielding from recognition by the immune system, thereby increasing the efficiency of delivery. We present a high-throughput microfluidic method that can monitor the shape of drifting cells due to interactions with nanoparticles and characterize the 3D dispersion of fluorescent silica nanoparticles at the surface of RBCs. The combination of fluorescence microscopy with image analysis demonstrates that the adsorption of silica nanoparticles onto the surface of RBCs is strongly influenced by electrostatic interactions. A reduced number of intact RBCs with increasing nanoparticle concentration beyond a certain threshold points to a toxicity mechanism associated with the nanoparticle adsorption at the surface of RBCs.

Red blood cells (RBCs) are universal carriers of oxygen to tissues in humans and animals. Their particular shape and great membrane elasticity allow for delivery of oxygen through tiny capillaries. It is thus an attractive target for bioengineering applications[1] that allows one to alter and "hijack" the surface of RBCs with nanomaterials[2,3] and modify their ability as a delivery vector. RBCs have many features of ideal drug carriers, including their bioavailability, biocompatibility, and a long lifetime in the bloodstream (approximately 120 days in humans).[4] Due to their simple structure, RBCs can be easier to tailor than other types of cells. They also lack many active processes vitally important for functioning of living cells including endocytosis.[5] In addition, engineered nanomaterials interacting with living cells have attracted increasing attention[6] in view of rising concerns of toxicity of these nanomaterials.

Nanoparticles (NPs) are actively exploited as vectors for targeted delivery, imaging tools and heat conductors for cancer treatment.[6] Among the undesirable effects and difficulties for NP biotechnological applications one can mention rapid covering of NPs with serum proteins[7] which leads to the formation of a protein corona and consequent recognition by the immune system. This effect also alters the surface properties of NPs and the aggregation of NPs into clusters and may be directly linked to hemolysis and consequent toxicity.[8,9]

Engineered complexes formed by RBCs and NPs attached to their surfaces provide several advantages for their applications:[10] it has been shown that the attachment of NPs to RBCs alters the function and properties of NPs and greatly reduces the NP uptake by mononuclear phagocytes.[11] The non-covalent attachment of NPs to RBCs increases their presence in the blood for over 24 hours and, at the same time, reduces their elimination by the liver and spleen.[11] Moreover, it has been demonstrated that NPs attached to the surface of RBCs can be reversibly removed from RBCs in a shear flow.[11] Another aspect of the attachment of NPs to RBCs is a "cleaning effect", *i.e.* a reduction of freely floating NPs in the bloodstream: NPs in the solution modify the hydrodynamic properties of the blood flow and might lead to the undesired formation of RBC clusters.[8] In turn, NPs by themselves can be used as blood-cleaning devices.[8]

Optimal observation conditions for optical microscopy are achieved for NPs on the order of hundreds of nanometers in

[a]*Departament d'Enginyeria Quimica, Rovira i Virgili, Tarragona, Spain.*
E-mail: vladimir.baulin@urv.cat
[b]*Leibniz-Institut für Polymerforschung Dresden e.V., Hohe Straße 6, 01069 Dresden, Germany*
[c]*Biopharma Technology, Winchester SO23 0LD, UK*
[d]*Université des Saarlandes, Experimental Physics and Center for Biophysics, 66123 Saarbrücken, Germany*

†Electronic supplementary information (ESI) available: ImageJ macro performing the 3D alignment for individual objects (3d alignment.ijm); a 3D alignment macro setup for batch processing of all open images (3d alignment_macro); macro counting the number of NP clusters present in the reconstructed images (3d analysis.ijm); a video of raw acquisition of a 3D stack of RBCs in suspension (3d stack.avi); a video of a 3D volume rendering of the RBC shown in Fig. 4; a video of a vesicle without NPs (control); a video of a vesicle with positively charged NPs (NH₂-modified). See DOI: 10.1039/c8nr09960j

UNIVERSITAT ROVIRA I VIRGILI
STUDY OF RBC SHAPE TRANSITIONS INDUCED BY NANOPARTICLES
André Eduardo Carneiro Dias

Paper

View Article Online

Nanoscale

diameter. These are typical sizes of NPs used for the visualization of NPs' interaction with RBCs. Previous studies of the interaction of NPs with RBCs revealed the spatial distribution of NPs on the surface of the RBCs.[12] Scanning electron microscopy under static conditions[13] allowed the visualization of the dispersion of ∼100–500 nm NPs on the surface of RBCs, while a lower spatial resolution has been achieved with fluorescence confocal microscopy and fluorescent NPs.[14,15] These independent experiments demonstrate that NPs are distributed randomly on the cell surface of RBCs. However, due to a flow in the solution, it was not possible to visualize NPs on a single RBC with these methods. For example, a shear flow present during the measurements is able to remove an individual NP from the RBC surface.[11] Indirect methods, such as the quantification of hemolysis, or optical microscopy monitoring the shape of RBCs, provide indirect information on the effect of NP adhesion on the RBC surface *via* characteristics such as deformability, clustering and cell death.[16] It is noteworthy that most of these experimental techniques require immobilized RBCs in solution, or even for cells to be attached to a substrate. As such, the characterization and visualization of individual cells with attached NPs within the flow is a challenging task.[17]

Here we present a high-throughput method that allows for quantification – and reconstruction in a 3D format – of fluorescently labelled NPs attached to the surface of fluorescent RBCs while they are flowing in a microfluidic chamber with a specially designed image analysis technique. In contrast to the standard laser scanning confocal microscopy that requires sample immobilization during scanning, our approach allows for the individual reconstruction of each cell regardless of its movement or spatial distribution. Other approaches to 3D imaging of fast-moving objects usually aim at increasing the scanning speed of the microscope to cancel their movement,[18] whereas we present a post-processing method which can be applied to any confocal microscope and computer hardware.

Materials and methods

Red blood cells

RBCs were isolated from the fresh whole sheep blood supplied in Alsever's medium (TCS Biosciences Ltd, UK) and used within one week. RBCs were washed twice by centrifugation at 500*g* and exchanging media with phosphate-buffered saline (PBS).

Silica nanoparticles

Amorphous, fluorescent and spherical "red-Sicastar" silica NPs (SiNPs) of 200 nm were purchased from Micromod Partikeltechnologie GmbH. These particles are prepared according to the hydrolysis process. The advantage of this process is that the fluorescent molecules are dispersed in the bulk of the NPs and their presence at a surface is marginal. They have a hydrophilic surface functionalized with terminal Si–OH bonds (*i.e.* plain silica). In order to compare the effects of the surface properties of NPs, fluorescent SiNPs with

different groups were used: $-NH_2$ (weakly negative) or $-COOH$ (strongly negative). See the ESI.†

Nanoparticles and RBC mixture

Samples were prepared by adding the SiNPs while adjusting hematocrit to 40% and were incubated at 37 °C overnight with constant stirring. After incubation, the samples were washed once with PBS and stored at 4 °C.

Hemolysis assay

After preparation, the samples were diluted to 1 : 20 in Milli-Q water and the absorbance was measured at 560, 576, 630 and 700 nm using a Tecan Infinite M200. Hemoglobin concentration, $c(Hb)$, was determined according to the protocol described by Benesch *et al.*[19] while using the absorbance at 700 nm as a background. RBCs' survivability was determined by

$$\text{Survivability } (\%) = \frac{c(\text{Hb})_{\text{final}}}{c(\text{Hb})_{\text{initial}}} \times 100.$$

Microfluidic device fabrication

Glass slides were coated with Blood Serum Albumin (BSA) and 20 μL of the sample were deposited onto the slide and isolated with a silicone spacer. The samples were washed twice by adding PBS and discarding the supernatant. The RBCs were stained by suspending the cells in 1% WGA-Alexa488 solution (Invitrogen) for 10 min and washing twice with PBS. Finally, the slide was mounted using Ibidi mounting medium.

Fluorescence imaging

Laser scanning confocal microscopy (LSCM) was performed using a Leica SP5 laser confocal microscope equipped with a resonant scanner. Different channels were acquired individually in the sequential mode.

Image reconstruction and analysis

The recorded microscopy images were reconstructed and analyzed automatically *via* a specially constructed image analysis technique compatible with ImageJ [available in the ESI†]. LSCM images were analyzed using FIJI,[20,21] a distribution version of ImageJ, in the following sequence. Individual objects were identified with a 3D Object counter[22] and aligned with Correct 3D Drift.[23] In particular, the number of NP clusters and their position inside or outside the RBC surface could be measured in a high-throughput manner. Nanoparticle clusters were counted with 3D object counter. The figures were plotted using Graphpad Prism 7. To achieve a successful reconstruction, a cell has to move less than a radius (from its starting position) during the scanning step. In our case, this was obtained when a cell was moving at less than 0.15 μm s⁻¹.

Giant unilamellar vesicles' preparation

Giant Unilamellar Vesicles (GUVs) were grown following the protocol of Angelova *et al.*[24] Briefly, 20 μl of a 1 mM lipid stock solution (DOPC/DOPS/Rho-DOPE, 91.2 : 8 : 0.8 mol%) in chloroform (Sigma) were dried on an ITO glass slide (Delta

Technologies) under vacuum and rehydrated with 2 ml of 200 mM sucrose (Sigma). GUV formation was performed at 8 Hz and 1.1 V for 2 h. The GUVs were then mixed with 0.1 mg ml^{-1} of fluorescent SiNPs and introduced by capillarity into a microfluidic chamber. The vesicles and the NPs were observed under an epifluorescence microscope (Zeiss Axio Observer.Z1) with two different excitation wavelengths (blue laser 493 nm and green laser 531 nm). To fabricate the observation chambers with a flat bottom, glass slides were cut into squares of about 2.5 × 2.5 cm and coated with octadecyltrichlorosilane (OTS, purchased from Sigma) to prevent GUV adhesion.[25,26] The OTS-coated glass squares were stacked with a cover slide (thickness 150 μm) as a spacer and glued together at three sides using epoxy glue.

GUV shape analysis

The shape of GUVs was analyzed automatically using Image-Pro Plus10 as commercial image processing software (Media Cybernetics).

Lipids

Phospholipids: dioleoyl-phosphatidylcholine (DOPC), dioleoyl-phosphatidylserine (DOPS), 1,2-dioleoyl-*sn-glycero*-3-phosphoethanolamine-*N*-(lissamine rhodamine B sulfonyl) (Rho-DOPE), 1,2-dioleoyl-*sn-glycero*-3-phosphoethanolamine (NBD-DOPE), and 7-nitrobenzofurazan-labeled. All lipids were purchased from Avanti Polar Lipids (USA).

Results and discussion

When fluorescent SiNPs were mixed with a suspension of RBCs, SiNPs became attached to the surface of RBCs. This process depends on the surface properties of NPs and to investigate the influence of the surface properties on adsorption, we tested 3 types of SiNPs with different levels of negative charge at physiological pH (Table 1). Our image recognition and analysis technique has been applied to fluorescence microscope images where RBCs had a red dye and the attached SiNPs had a green dye.

It was possible to reconstruct a 3D structure of a single cell by slowly drifting in the solution during the acquisition of fluorescent images using a confocal microscope by a combination of (i) identification of the 3D object center of mass and (ii) correction for flow of the center of mass of the stack. A typical example of a fluorescence image that was analyzed is shown in Fig. 1. As a result of the analysis, 3D reconstructed cells with or without the attached NPs have been obtained (Fig. 2). This method can be applied to each detected cell in the solution automatically and thus, such a high-throughput
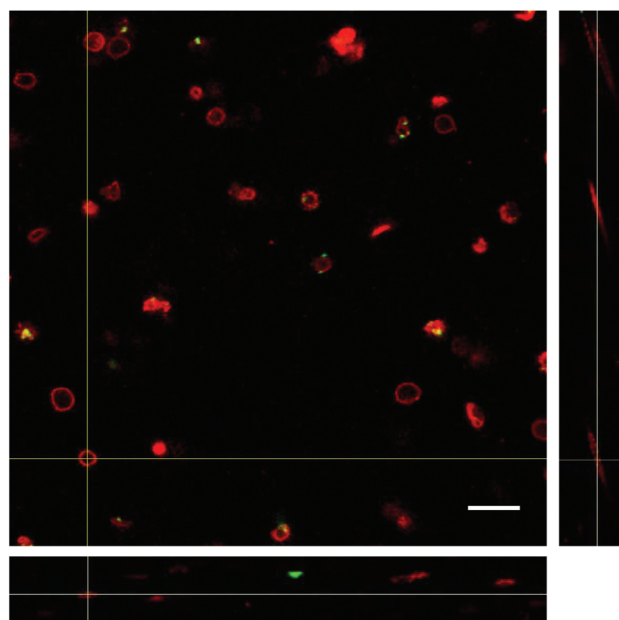
Fig. 1 Orthogonal view of a raw acquisition of the 3D stack of RBCs with SiNPs. *XZ* and *YZ* views show the distortion of the cell caused by their movement. Scale bar corresponds to a 10 μm length.
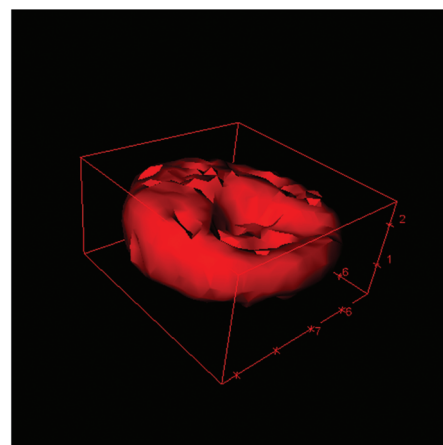
Fig. 2 3D surface reconstruction of a RBC after alignment. The outer limit of the cell was rendered in 3D.

method provides an accurate statistics of the shapes of RBC cells affected by the interaction with NPs and allows the visualization of NPs attached to the surface of RBCs. However, due to the resolution of the microscope, it was not possible to distinguish individual NPs from the clusters of NPs (Fig. 3). Therefore, we consider that NP clusters can consist of one or several NPs. In contrast, the spatial resolution of confocal images was good enough to resolve the position of the cluster with respect to the membrane of the cell, *i.e.* distinguish whether the cluster has crossed the membrane and attached to the inside of the cell or it was localized at the RBC membrane outside of the cell (Fig. 4). Thus, this method can be

Table 1 Zeta-potential measurements of SiNPs employed in this study

	NH$_2$	Plain	COOH
pH = 7.4	−39.5 mV (±7)	−54.8 mV (±7)	−63.7 mV (±10)

UNIVERSITAT ROVIRA I VIRGILI
STUDY OF RBC SHAPE TRANSITIONS INDUCED BY NANOPARTICLES
André Eduardo Carneiro Dias

Paper

View Article Online

Nanoscale
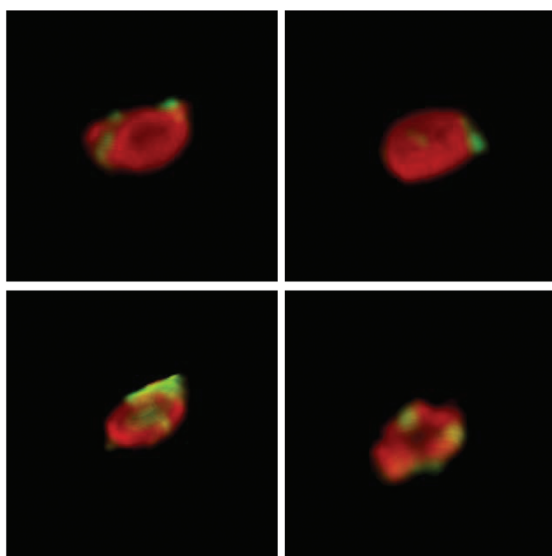
Fig. 3 3D volume reconstruction of RBCs with SiNPs adsorbed onto the surface. The cell is reconstructed based on the intensity of the signal acquired. This allows the visualization of multiple signals in contrast to surface-only visualization.
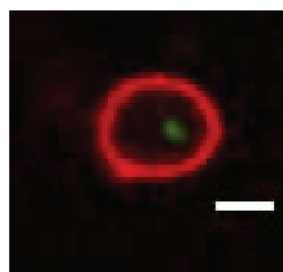
Fig. 4 Rare occurrence of a negatively charged SiNP inside a RBC. Scale bar corresponds to a 2 μm length.

Fig. 5 (A) Average number of SiNP clusters attached to single RBCs and (B) fraction of cells containing at least 1 SiNP cluster. RBCs were reconstructed and individually analyzed for the presence and number of SiNP clusters. The results are shown as average and SEM.

used for screening of translocation events through the membrane of the cell and allows for the collection of the corresponding statistics over many cells. It would be possible to extend this method to study endocytosis and active or passive membrane crossings with other types of living cells for different nanoobjects.

In order to obtain a complete 3D reconstruction of the cell, the flow should be slow enough to allow for the confocal microscope to complete the scanning of z-stacks before the cell moves out of the field of view. For the standard conditions reported in this article, RBC 3D reconstruction can be achieved at flow speeds slower than 3 μm (in the xx' and yy' axes) per z step of the microscope.

It is noteworthy that the concentration of NPs plays an important role in the attachment of NPs to the RBCs. Increasing the concentration of plain SiNPs from ~1 mg ml^{-1} to ~5 mg ml^{-1} in the RBC suspension strongly affects the distribution of clusters at the cell surface (Fig. 5). Interestingly, for the highest concentration of plain SiNPs in this experi-

ment, NPs do not cover the RBC surface uniformly, but form clusters at the RBC surface, which increase in number.

The number of attached NPs and clusters formed on the surface of RBCs depends on the surface properties of the NPs. Plain SiNPs are charged negatively in water, while $-NH_2$ surface-modified SiNPs are less negatively charged and $-COOH$ surface-modified SiNPs are more negatively charged (Table 1).

The number of clusters attached to the RBCs' surface for plain SiNPs, at 5 mg ml^{-1}, is on average 0.42 per cell. This number looks relatively small when taking into account the considerable SiNP concentration in the suspension. A further increase in the concentration leads to lysis of the cells. For the most negatively charged COOH–SiNPs the number of clusters attached to the RBCs' surface is similar for the same concentrations. Even at a very high concentration, 5 mg ml^{-1}, the average number of clusters attached to RBCs is only equal to

UNIVERSITAT ROVIRA I VIRGILI
STUDY OF RBC SHAPE TRANSITIONS INDUCED BY NANOPARTICLES
André Eduardo Carneiro Dias

Nanoscale

View Article Online

Paper

0.5. In contrast, for the least negatively charged NH$_2$–SiNPs, the average number of clusters attached to the RBC surface is 2.1. Assuming that clusters have similar sizes, these results indicate that the least negatively charged NH$_2$–SiNPs attach to the RBC surfaces in larger amounts than plain SiNPs and COOH–SiNPs suggesting that the attachment of SiNPs is influenced by the charge. The least negatively charged NH$_2$–SiNPs have less repulsion with negative charges at the RBC surface. This fact can also explain the difficulty for highly negatively charged COOH–SiNPs to attach to the RBC surface and explains why plain SiNPs do not attach to RBC surfaces in large numbers, despite the high adhesion energy between the plain silica surface and a single RBC, as measured by AFM.[27]

In addition to the quantification of the numbers of clusters attached to the RBCs' surface, this method can indirectly inform on the toxicity of NPs that at high concentrations can induce RBC hemolysis.[28] To study this effect, we measured the RBCs' survivability with a hemolysis assay as a function of the SiNP concentration (Fig. 6). RBCs' survivability can be evaluated according to the concentration of hemoglobin. As different forms of the molecule have different absorbance spectra, the contribution of each species must be taken into account.[19] Plain SiNPs and highly charged COOH–SiNPs present similar hemolysis values and they are able to disrupt RBCs at concentrations above 1 mg ml^{-1}. This may indicate that the presence of (several) clusters is mandatory to cause the mechanical disruption of the RBC membrane. However, the least negatively charged NH$_2$–SiNPs seem to have a significantly higher toxicity at lower concentrations (Fig. 6), which is likely associated with possibly stronger attraction to the surface of RBCs. It is interesting to compare these hemolysis results with those reported in the literature.[29–31] Crystalline and amorphous plain SiNPs have also been reported to trigger membrane disruption at high nanoparticle concentrations.[29–31] The hemolysis rate is similar for NPs of the same size (~20%), when we compare with our results for highly negatively charged and plain SiNPs.[31] However, this survivability rate is much weaker compared to ~40% hemolysis
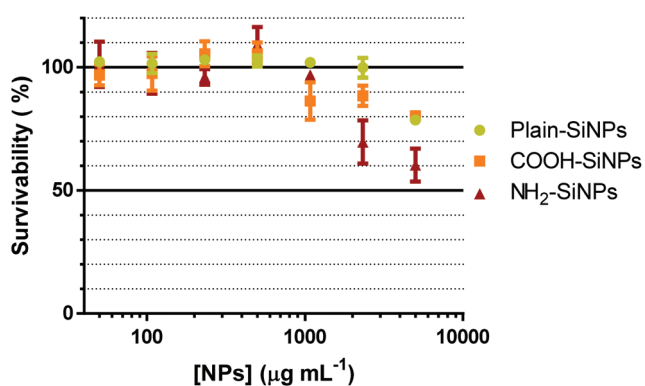
rate measured for our positively charged SiNPs,[30] confirming a key role of electrostatic interactions in the interaction between RBCs and the SiNPs.

To demonstrate the more general applicability of the results presented in this study, we studied the interaction between the same three types of SiNPs and Giant Unilamellar Vesicles (GUVs). GUVs can be considered as a model system for RBCs, while being less rigid, with a fluid membrane and also without having a glycocalyx layer as a pericellular matrix coating the RBC surface. To mimic RBC lipid bilayers, fluorescent GUVs containing a DOPC/DOPS mixture were prepared with the addition of 8% PS lipids, which provide a negative electrostatic charge to the vesicles. Note that GUVs in the absence of NPs show a very regular spherical shape. On adding fluorescent plain SiNPs with different fluorescent excitation wavelengths as compared to the lipids composing the vesicles, we observed no distortion of the GUV shape (Fig. 7). However, it is not clear whether these plain negatively charged SiNPs could detach reversibly from the GUV surface. In contrast, highly negatively charged SiNPs show large fluctuations of the shape suggesting strong disturbance to the membrane of the GUVs.

Comparing the results of the interaction of the three types of NPs with different charges between GUVs and RBCs, we observe that the lowest negatively charged SiNPs are showing the strongest attachment, while stronger negatively charged SiNPs are showing a weaker attachment for both lipid vesicles and RBCs. This is consistent with literature data.[24–26] However, there are two important differences: first, no clusters are

Fig. 6 Survivability of RBCs when exposed to different concentrations of SiNPs. Weakly charged NH$_2$–SiNPs show a higher toxicity (*i.e.* lower RBC survivability). Error bars show the SD from 3 independent experiments.
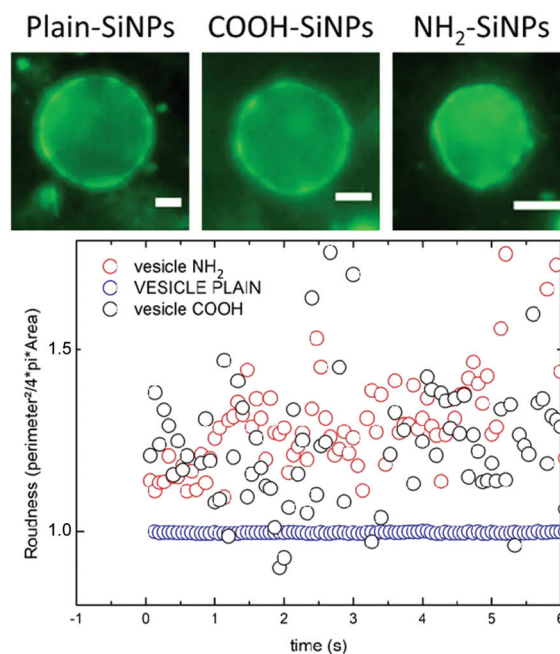

Fig. 7 Fluorescence microscopy images (top) and the corresponding roundness measurements (bottom) of a GUV when in contact with different SiNPs throughout a brief period of time. Scale bars correspond to a 10 μm length.

observed on GUVs for all three types of SiNPs used in this study and in contrast to RBCs, GUVs are covered with SiNPs homogeneously. This may indicate that a shear flow may trigger the clustering of SiNPs in the RBC experiment. Second, the lowest negatively charged NH_2-SiNPs attach more strongly to GUVs than to RBCs. This may be due to a structural difference between vesicles (fluid membrane) and RBCs (elastic membrane) and the glycocalyx network covering the RBC surface; this question requires further investigation.

Conclusions

A high-throughput image analysis and reconstruction method has been presented that enables fast 3D reconstruction and characterization of individual RBCs flowing in a microfluidic chamber. This automated method can enable the visualization and characterization of the distribution of fluorescent NP clusters attached to RBC surfaces and furthermore, the data presented here demonstrate that this technique can also resolve the 3D position of a NP cluster on the RBCs' surface. Moreover, this method allows the user to distinguish whether the cluster is located inside the cell, or at its surface. This method was applied to the analysis of the interaction of SiNPs with different levels of negative charges. It turned out that plain and highly negatively charged COOH–SiNPs do not interact strongly with RBCs, while weakly charged NH_2–SiNPs show strong attachment to the RBC surface. These results were confirmed with the model experimental system, GUVs with the lipid composition mimicking the structure of the RBC bilayer and the same three types of SiNPs. GUV experiments show similar behavior, with weakly charged NH_2–SiNPs attaching more strongly to the membrane than plain and highly charged COOH–SiNPs. However, in contrast to RBCs, no clusters were observed for all three types of SiNPs. This may indicate that hydrodynamic flow plays a key role in triggering the clustering of SiNPs. These results are interesting in the context of the toxicity of SiNPs. In particular, NH_2–NPs show high hemolysis properties in comparison to similar sized silica nanoparticles with a different surface, or structural, chemistry. The image reconstruction suggests that the presence of clusters is the cause of the cells' hemolysis. Finally, we expect that this method can be extended to other types of living cells and nanoobjects. It may also be further applied to record the structure of fluorescent biomolecules in living cells, like microtubules, vesicles, proteins, or lipid droplets.

Author contributions

A. D., K. W., J. B. F. and V. B. designed the experiments, A. D. and K. W. performed experiments with RBCs, J. B. F. carried out experiments with vesicles, A. D. and J. B. F did image reconstruction and analysis, and A. D., M. W., K. W., J.-B. F. and V. B. wrote the paper.

Conflicts of interest

The authors declare no conflicts of interest.

Acknowledgements

References

1 D. Septiadi, F. Crippa, T. L. Moore, B. Rothen-Rutishauser and A. Petri-Fink, *Adv. Mater.*, 2017, **30**, 1704463.

2 C. H. Villa, D. B. Cines, D. L. Siegel and V. Muzykantov, *Transfus. Med. Rev.*, 2017, **31**(1), 26–35.

3 A. Krantz, *Blood Cells, Mol., Dis.*, 1997, **23**, 58–68.

4 C. H. Villa, D. C. Pan, S. Zaitsev, D. B. Cines, D. L. Siegel and V. R. Muzykantov, *Ther. Delivery*, 2015, **6**, 795–826.

5 R. Schekman and S. J. Singer, *Proc. Natl. Acad. Sci. U. S. A.*, 1976, **73**, 4075–4079.

6 V. Mailänder and K. Landfester, *Biomacromolecules*, 2009, **10**, 2379–2400.

7 E. Casals, T. Pfaller, A. Duschl, G. J. Oostingh and V. Puntes, *ACS Nano*, 2010, **4**, 3623–3632.

8 J. Tan, W. Keller, S. Sohrabi, J. Yang and Y. Liu, *Nanomaterials*, 2016, **6**, 30.

9 D. Walczyk, F. B. Bombelli, M. P. Monopoli, I. Lynch and K. A. Dawson, *J. Am. Chem. Soc.*, 2010, **132**, 5761–5768.

10 J. S. Brenner, D. C. Pan, J. W. Myerson, O. A. Marcos-Contreras, C. H. Villa, P. Patel, H. Hekierski, S. Chatterjee, J.-Q. Tao, H. Parhiz, *et al.*, *Nat. Commun.*, 2018, **9**, 2684.

11 V. H. Nguyen and B.-J. Lee, *Int. J. Nanomed.*, 2017, **12**, 3137–3151.

12 C.-M. J. Hu, L. Zhang, S. Aryal, C. Cheung, R. H. Fang and L. Zhang, *Proc. Natl. Acad. Sci. U. S. A.*, 2011, **108**, 10980–10985.

13 B. M. Rothen-Rutishauser, S. Schürch, B. Haenni, N. Kapp and P. Gehr, *Environ. Sci. Technol.*, 2006, **40**, 4353–4359.

14 L. Treuel, X. Jiang and G. U. Nienhaus, *J. R. Soc., Interface*, 2013, **10**, 20120939–20120939.

15 M. Stefanic, K. Ward, H. Tawfik, R. Seemann, V. Baulin, Y. Guo, J.-B. Fleury and C. Drouet, *Biomaterials*, 2017, **140**, 138–149.

16 S. O. Sowemimo-Coker, *Transfus. Med. Rev.*, 2002, **16**, 46–60.

17 J. Dupire, M. Socol and A. Viallat, *Proc. Natl. Acad. Sci. U. S. A.*, 2012, **109**, 20808–20813.

18 H. Mikami, J. Harmon, H. Kobayashi, S. Hamad, Y. Wang, O. Iwata, K. Suzuki, T. Ito, Y. Aisaka, N. Kutsuna, K. Nagasawa, H. Watarai, Y. Ozeki and K. Goda, *Optica*, 2018, **5**, 117–126.

19 R. E. Benesch, R. Benesch and S. Yung, *Anal. Biochem.*, 1973, **55**, 245–248.

UNIVERSITAT ROVIRA I VIRGILI
STUDY OF RBC SHAPE TRANSITIONS INDUCED BY NANOPARTICLES
André Eduardo Carneiro Dias

Nanoscale

View Article Online

Paper

20 C. T. Rueden, J. Schindelin, M. C. Hiner, B. E. DeZonia, A. E. Walter, E. T. Arena and K. W. Eliceiri, *BMC Bioinf.*, 2017, **18**, 529.

21 J. Schindelin, I. Arganda-Carreras, E. Frise, V. Kaynig, M. Longair, T. Pietzsch, S. Preibisch, C. Rueden, S. Saalfeld, B. Schmid, *et al.*, *Nat. Methods*, 2012, **9**, 676–682.

22 S. Bolte and F. P. Cordelières, *J. Microsc.*, 2006, **224**, 213–232.

23 A. Parslow, A. Cardona and R. J. Bryson-Richardson, *J. Visualized Exp.*, 2014, **86**, e51086.

24 M. I. Angelova, S. Soléau, P. Méléard, F. Faucon and P. Bothorel, in *Trends in Colloid and Interface Science VI*, 1992, vol. 89, pp. 127–131.

25 M. E. McGovern, K. M. R. Kallury and M. Thompson, *Langmuir*, 1994, **10**, 3607–3614.

26 R. Tero, M. Takizawa, Y.-J. Li, M. Yamazaki and T. Urisu, *Langmuir*, 2004, **20**, 7526–7531.

27 Y. Wu, Y. Hu, J. Cai, S. Ma, X. Wang, Y. Chen and Y. Pan, *Micron*, 2009, **40**, 359–364.

28 L. Yildirimer, N. T. K. Thanh, M. Loizidou and A. M. Seifalian, *Nano Today*, 2011, **6**, 585–607.

29 V. Murashov, M. Harper and E. Demchuk, *J. Occup. Environ. Hyg.*, 2006, **3**, 718–723.

30 H. Shinto, T. Fukasawa, K. Yoshisue, M. Tezuka and M. Orita, *Adv. Powder Technol.*, 2014, **25**, 1872–1881.

31 B. Wildt, R. A. Malinauskas and R. P. Brown, in *Handbook of Immunological Properties of Engineered Nanomaterials*, ed. Frontiers in Nanobiomedical Research, World Scientific, 2012, vol. 1, pp. 173–206.

Annex II

Original article published as collaborative project in the scope of ITN-SNAL:

Orlowska, A., Perera, P. T., Al Kobaisi, M., **Dias, A.**, Nguyen, H. K. D., Ghanaati, S., Baulin, V., Crawford, R. J., Ivanova, E.P. (2017) The Effect of Coatings and Nerve Growth Factor on Attachment and Differentiation of Pheochromocytoma Cells. Materials (Basel).11, 1 E60;

Annex II

materials

MDPI

Article

The Effect of Coatings and Nerve Growth Factor on Attachment and Differentiation of Pheochromocytoma Cells

Anna Orlowska [1,2], **Pallale Tharushi Perera** [3], **Mohammad Al Kobaisi** [3], **Andre Dias** [1,2], **Huu Khuong Duy Nguyen** [3], **Shahram Ghanaati** [1], **Vladimir Baulin** [2] (iD), **Russell J. Crawford** [4] and **Elena P. Ivanova** [3,*] (iD)

[1] Frankfurt Orofacial Regenerative Medicine, University Hospital Frankfurt, Theodor-Stern-Kai 7, D-60590 Frankfurt am Main, Germany; a.b.orlowska@gmail.com (A.O.); andreecdias@gmail.com (A.D.); s.ghanaati@med.uni-frankfurt.de (S.G.)

[2] Departament d'Enginyeria Quimica, Universitat Rovira i Virgili, 26 Avenue dels Paisos Catalans, 43007 Tarragona, Spain; va.baulin@gmail.com

[3] Department of Chemistry and Biotechnology, School of Science, Swinburne University of Technology, P.O. Box 218, Hawthorn VIC 3122, Australia; pgperera@swin.edu.au (P.T.P.); malkobaisi@swin.edu.au (M.A.K.); huukhuongduynguyen@swin.edu.au (H.K.D.N.)

[4] School of Science, RMIT University, P.O. Box 2476, Melbourne VIC 3001, Australia; Russell.Crawford@rmit.edu.au

* Correspondence: eivanova@swin.edu.au; Tel.: +61-3-9214-5137; Fax: +61-3-9819-0834

Abstract: Cellular attachment plays a vital role in the differentiation of pheochromocytoma (PC12) cells. PC12 cells are noradrenergic clonal cells isolated from the adrenal medulla of *Rattus norvegicus* and studied extensively as they have the ability to differentiate into sympathetic neuron-like cells. The effect of several experimental parameters including (i) the concentration of nerve growth factor (NGF); (ii) substratum coatings, such as poly-L-lysine (PLL), fibronectin (Fn), and laminin (Lam); and (iii) double coatings composed of PLL/Lam and PLL/Fn on the differentiation process of PC12 cells were studied. Cell morphology was visualised using brightfield phase contrast microscopy, cellular metabolism and proliferation were quantified using a 3-(4,5-dimethylthiazol-2-yl)-5-(3-carboxymethoxyphenyl)-2-(4-sulfophenyl)-2H-tetrazolium (MTS) assay, and the neurite outgrowth and axonal generation of the PC12 cells were evaluated using wide field fluorescence microscopy. It was found that double coatings of PLL/Lam and PLL/Fn supported robust adhesion and a two-fold enhanced neurite outgrowth of PC12 cells when treated with 100 ng/mL of NGF while exhibiting stable metabolic activity, leading to the accelerated generation of axons.

Keywords: nerve growth factor (NGF); poly-L-lysine; fibronectin; laminin; PC12 neuronal differentiation

1. Introduction

The pheochromocytoma (PC12) cell line is commonly used in in vitro studies to examine neuronal differentiation and neurotoxicity implicated in neurodegenerative disease [1,2]. PC12 cells are noradrenergic clonal cells originating from *Rattus norvegicus* transplantable pheochromocytoma [1]. They exhibit a reversible response to nerve growth factor (NGF). After NGF exposure, PC12 cells acquire characteristic phenotypic properties associated with sympathetic neuron-like cells, which includes the inhibition of proliferation, outgrowth of neurites, and the possibility of being electrically excitable [1–3]. Upon differentiation, the neuron-like PC12 cells start to express various integral proteins that are responsible for neurite growth [1] and can transmit signals along the axons [4,5].

In laboratory conditions, PC12 cells attach poorly to polystyrene (PS) tissue culture surfaces [4,6] where they grow mostly as floating cell aggregates [6]. This poor adhesion ultimately results in insufficient levels of neurite outgrowth [4]. Functionalization of the surface can improve the attachment of the PC12 cells. Previously, it was shown that the pre-treatment of the substratum surface with proteins, especially the extracellular matrix components, enhanced not only cell adhesion, but also their growth, morphology, migration, and differentiation, increasing their life-span [7].

Various substratum coatings used in the formation of PC12 neuronal processes have been reported, e.g., glycoproteins, collagen (type IV from human placenta, type I) [8–11], laminin (Lam) [12], and fibronectin (Fn) [3]. In addition, it was shown that polyornithine [3,13–16], poly-D-lysine, and poly-L-lysine (PLL) can be used to enhance the attachment of PC12 cells [8–11]. Although Tomaselli et al. [17] have shown that Lam and collagen type IV coated surfaces promoted PC12 adhesion to a greater degree than Fn, no systematic assessment of the suitability of various coatings that would enhance the attachment and differentiation of PC12 cells has been performed. Therefore, the aim of our study was to investigate the effect of five coating types, including Lam, Fn, and PLL (and various combinations of these coatings) on the attachment, proliferation, and differentiation of PC12 cells. The extent of differentiation of the PC12 cells using different coatings was monitored by measuring a set of parameters related to cellular functions as a function of NGF concentration. The proliferation and metabolic activity of the PC12 cells were analysed using an MTS (3-(4,5-dimethylthiazol-2-yl)-5-(3-carboxymethoxyphenyl)-2-(4-sulfophenyl)-2H-tetrazolium) assay. The morphology and neuron-like characteristics of the cells were analysed by using brightfield phase contrast microscopy and wide field fluorescence microscopy.

2. Materials and Methods

2.1. PC12 Cell Line

Commercially-available PC12 CRL-1721™ cells were obtained from the American Type Culture Collection (American Type Culture Collection (ATCC), Manassas, VA, USA). The cells were cultured in 75 mm^2 tissue culture flasks with complete Gibco™ 1640 RPMI medium supplemented with 10% horse serum (HS, Thermo Fisher Scientific Australia Pty Ltd., Melbourne, Australia), 5% fetal bovine serum (FBS, Thermo Fisher Scientific Australia Pty Ltd., Melbourne, Australia) and 1% Penicillin/Streptomycin (Pen/Strep, Thermo Fisher Scientific Australia Pty Ltd., Melbourne, Australia). The cells were maintained according to standard protocols [4,18] at 37 °C in a 95% humidified incubator with 5% CO$_2$. The medium was changed every 2 days, and passaged accordingly when the confluence reached 90%.

2.2. Coatings

2.2.1. Poly-L-lysine

Sterile-filtered poly-L-lysine (PLL) (molecular weight 150,000–300,000 Da) was purchased from Sigma-Aldrich (Sydney, Australia) and used at the recommended concentration of 0.01% w/v in water. The sterile filtered solution was stored at 4 °C until required.

2.2.2. Fibronectin

Fibronectin (Fn) was purchased from Sigma-Aldrich (Sydney, Australia) in lyophilized powder form. An aqueous working solution of 40 µg/mL concentration was prepared and stored at −20 °C until required.

2.2.3. Laminin

Laminin (Lam) derived from a mouse Engelbreth-Holm-Swarm (EHS) sarcoma was purchased from Sigma-Aldrich (Sydney, Australia). An aqueous working solution of 10 µg/mL concentration was prepared and stored at -20 °C until required.

2.3. Atomic Force Microscopy

The surface topography of the various substrata was visualized using an Innova® atomic force microscope (Bruker, Billerica, MA, USA). A phosphorous-doped silicon probe (MPP-31120-10, Bruker, Billerica, MA, USA) was employed in tapping mode for all measurements performed in air, at a temperature of approximately 22 °C. The atomic force microscopy (AFM, Veeco, Bruker, Billerica, MA, USA) scans, obtained over a 10 µm × 10 µm surface area with 512 × 512 data points, were processed using Gwyddion software (Version 2.49, Czech Metrology Institute, Brno, Czech) [19]. Analysis was conducted using three AFM micrographs for each sample, and for two samples of each substratum surface. The surface roughness parameters derived from the AFM data included the arithmetic average height (S_a), root mean square deviation from the mean plane (S_q), maximum height of the profile (S_{max}), skewness (S_{skw}), and kurtosis (S_{kur}), as described in detail elsewhere [20].

2.4. Differentiation of PC12 Cells

PC12 cells were seeded onto 24-well polystyrene (PS) tissue culture plates at a density of 3×10^4 cells/mL in Gibco™ 1640 Roswell Park Memorial Institute (RPMI) medium (1% HS, 1% FBS and 1% Pen/Strep) supplemented with 0, 25, 50, and 100 ng/mL Nerve Growth Factor (NGF) (mouse recombinant NGF 7S, Sigma-Aldrich, Sydney, Australia). Prior to seeding, the tissue culture dish (Sarstedt AG & Co., Nümbrecht, Germany) was prepared with different coatings, with each being prepared in triplicate. Non-coated plates were employed as control surfaces. PLL was added to cover the entire surface area and incubated at 25 °C for 2 h. The wells were washed with phosphate-buffered saline (PBS) and a second coating of Fn or lam was added and incubated at 25 °C for 2 h. The non-coated wells of the tissue culture dishes were used as control surfaces. At least two technical replicates were completed. The culture medium on the samples was changed every second day.

2.5. Metabolic Activity

The metabolic activity of the PC12 cells was determined using the CellTiter 96®AQueous One Solution Cell Proliferation Assay (Promega, Sydney, Australia). The assay was performed by adding the tetrazolium compound to the PC12 cell culture at a 10% ratio of the final volume. This allowed the reduction of (3-(4,5-dimethylthiazol-2-yl)-5-(3-carboxymethoxyphenyl)-2-(4-sulfophenyl)-2H-tetrazolium) (MTS) to formazan, resulting in the formation of a coloured precipitate. The absorbance of the resultant solution was recorded at a wavelength of 490 nm after incubation for 90 min at 37 °C using a FLUOstar Omega microplate reader (BMG LABTECH, Cary, NC, USA).

2.6. Assessment of Neurite Outgrowth

A neurite outgrowth analysis was performed using representative digitized photomicrographs of each well, obtained using a phase contrast brightfield inverted Olympus microscope (CKX41, Olympus, Tokyo, Japan) equipped with a Panasonic camera (DMC-GH3). The quantity of differentiated cells was established by the visual detection of neurites. Evaluation of neurite growth was carried out by manually tracking the length of the neurites on each cell using NeuronJ software (ImageJ plugin; NIH, Bethesda, MD, USA). This procedure was conducted for all cells in a field where the entire neurite could be visualized.

2.7. Widefield Fluorescence Microscopy

After a 5-day incubation period, the cells were washed with PBS and fixed with 4% paraformaldehyde for 15 min. After fixation, the cells were washed with PBS and cell membranes were

stained using Wheat Germ Agglutinin, Alexa Flour™ 488 (WGA, Thermo Fisher Scientific Australia Pty Ltd., Melbourne, Australia). The nucleus was stained using DAPI (4′,6-diamidino-2-phenylindole). Samples were then imaged using a Nikon Eclipse Ti-E epifluorescence inverted microscope (Nikon Instruments Inc., Tokyo, Japan). Sequential images were acquired using DAPI and GFP-B standard series filter cubes and analysed using FIJI (ImageJ) software (k.1.45, National Institute of Mental Health, Bethesda, MD, USA) [21].

2.8. Statistical Analysis

Statistically significant differences ($p < 0.05$, $p < 0.01$, $p < 0.001$, $p < 0.0001$) were calculated among the various groups using a two-way ANOVA analysis followed by Tukey's multiple comparison test. All statistical analyses were carried out using the GraphPad Prism 7 statistical software package (GraphPad Software, Inc., San Diego, CA, USA).

3. Results

Single- and two-component coatings were investigated in this study. The glycoproteins, such as Lam and Fn, were selected because they are typical components of the extracellular matrix [5,17,22,23]. It has been reported that Lam and Fn positively influenced the outgrowth of neurons, axonal guidance, differentiation and cell proliferation [5,22]. Since PLL was reported to facilitate cell attachment and improve the differentiation of PC12 cells [24], PLL was also selected for analysis. In addition to single component coatings, PLL/Lam and PLL/Fn combination coatings were also studied.

3.1. Protein Distribution on the Substratum

An AFM analysis confirmed that an even distribution of the coatings was present on the plastic surfaces of the cell culture wells (Figure 1A). The S_a of the control (2.2 ± 0.2 nm) was found to be similar to that present on the substrata with a single coating, namely, Fn (1.8 ± 0.1 nm) and PLL (2.1 ± 0.7 nm). The Lam coating exhibited a higher S_a of 2.9 ± 0.4 nm. The PLL/Fn and PLL/Lam dual component coatings were found to have S_a of 3.4 ± 0.4 nm and 5.8 ± 1.2 nm, respectively.

3.2. PC12 Cell Attachment and Initial Differentiation in the Presence of NGF

The extent of growth of the PC12 cells on substrata containing the five different coating types, together with various concentrations of NGF, was investigated in order to identify the most suitable growth conditions for the stimulated attachment and differentiation of PC12 cells into neuron-like cells. Cell attachment, growth, and differentiation patterns were monitored over a five-day period (Figures 1B and 2). The initial differentiation and attachment propensity of the PC12 cells after 48 h (day 2) was studied using phase-contrast brightfield microscopy (Figure 1B).

The densities of attached cells on the substrata possessing a single Lam coating and dual-component coatings were found to be comparable, whereas isolated, spherically-shaped cells were observed without protrusions on substrata containing the PLL and Fn coatings. Enhanced levels of cell attachment were detected on substrata containing the PLL/Fn and Lam coatings in the presence of 50 ng/mL NGF (Figure 1B). In the absence of 50 ng/mL NGF, only a few cells were observed to have attached to these surfaces. These results confirmed that the presence of a coating is essential for robust cell attachment to be supported, whereas it was apparent that NGF could act as a co-factor for achieving enhanced levels of cell attachment.

In order to compare and confirm the cell differentiation processes on the various substrata being investigated, PC12 cells were stained with a membrane specific protein and imaged using wide field fluorescence microscopy (Figure 2). Analysis of the fluorescence micrographs indicated that the dual component PLL/Fn and PLL/Lam coatings supported enhanced levels of PC12 cell differentiation, as evidenced by the presence of neurite outgrowth. In contrast, on PLL- and Lam-coated surfaces, the PC12 cells exhibited a lower degree of differentiation, with no or just a few non-differentiated cells being observed on the Fn- and non-coated surfaces.

(A) (B)
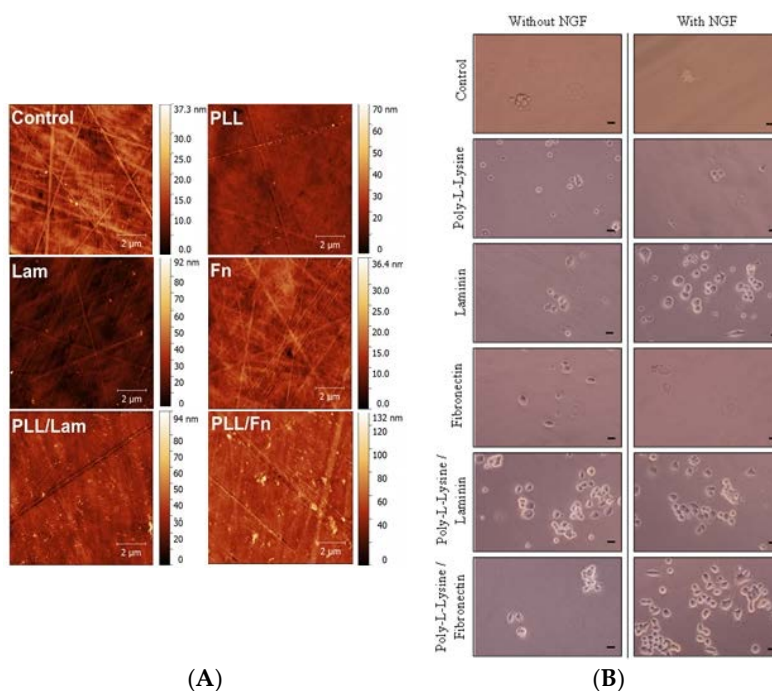
Figure 1. (**A**) AFM analysis of surfaces with different coatings. The AFM micrographs show an even distribution of single and two-component coatings on the surfaces of the polystyrene substratum. (**B**) Attachment and initial differentiation of PC12 cells after two days of incubation in the presence and absence of NGF solution. Cells were seeded at a density of 3×10^4 cells/mL on poly-L-lysine, laminin, fibronectin, poly-L-lysine/laminin, and poly-L-lysine/fibronectin-coated wells. The cells were grown in a medium that was supplemented with human recombinant NGF (50 ng/mL). The control wells did not contain any coating. In these experiments the PC12 cells appeared to attach to the surface in clusters. Scale bar is 5 μm.
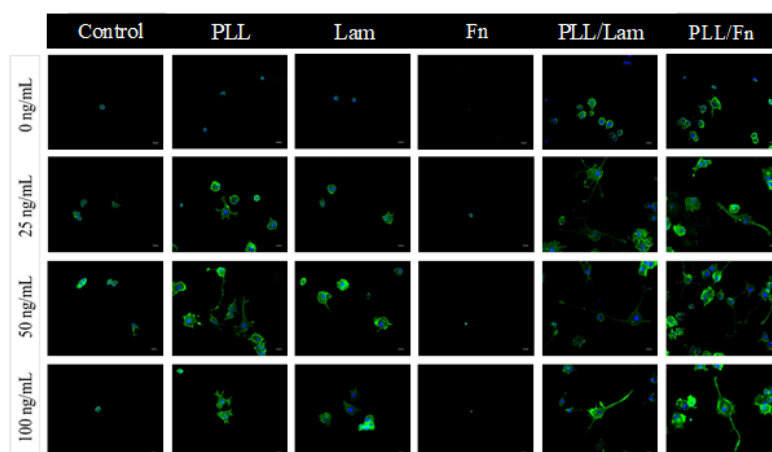
Figure 2. Comparative differentiation of PC12 cells on substrata with single- and two-component coatings in the presence of NGF solution. The NGF concentrations used were 0, 25, 50, and 100 ng/mL. Cells were grown over a period of five days; fixed in 4% PFA for 15 min and stained with WGA-488 (membrane, green), DAPI (nuclei, blue). Significant neurite outgrowth was observed for cells grown on substrata with double coatings containing poly-L-lysine/laminin and poly-L-lysine/fibronectin. Substrata containing single coatings of poly-L-lysine and laminin exhibited poor cell differentiation.

PC12 cells incubated on Fn- or non-coated surfaces exhibited little to no attachment propensity in both the presence and absence of NGF. These results are consistent with previously reported data

that suggested that NGF acted as a co-factor in enhancing the attachment and differentiation of cells, however, the surface coating itself was found to be the main factor determining the extent to which cells would attach to surfaces.

3.3. PC12 Cells Metabolic Activity and Proliferation

The differentiation of PC12 cells into neuron-like cells has been found to be accompanied by an arrest in the post-mitotic G0 stage in the cell cycle, which in turn decreased their potential to proliferate [1–3,25]. A commonly used method for the evaluation of proliferation activity is through monitoring cell metabolic activity via an MTS assay [26]. In this work, an MTS assay was employed to study the metabolic activity of the PC12 cells while attached to the different substratum surfaces. PC12 cells grown on PLL-coated substrata exhibited an increased growth after five days when both 25 and 50 ng/mL NGF was present, compared to growth in the absence of NGF (Figure 3). At a concentration of 100 ng/mL NGF, however, a decrease in cell growth was observed. This decrease is likely to be associated with a progression of the cells into an arrested G0 stage, which is characteristic of PC12 cells that have undergone a differentiation to form neuron-like cells. Analysis of the metabolic activity of the PC12 cells 24 h after seeding (day 1) indicated that the metabolic activity of the cells increased in the presence of NGF, however, when cells were incubated on a PLL-coated substratum, an increase in metabolic activity was not observed. After the third day of growth, a similar metabolic activity was observed for all cells attached to all surfaces.
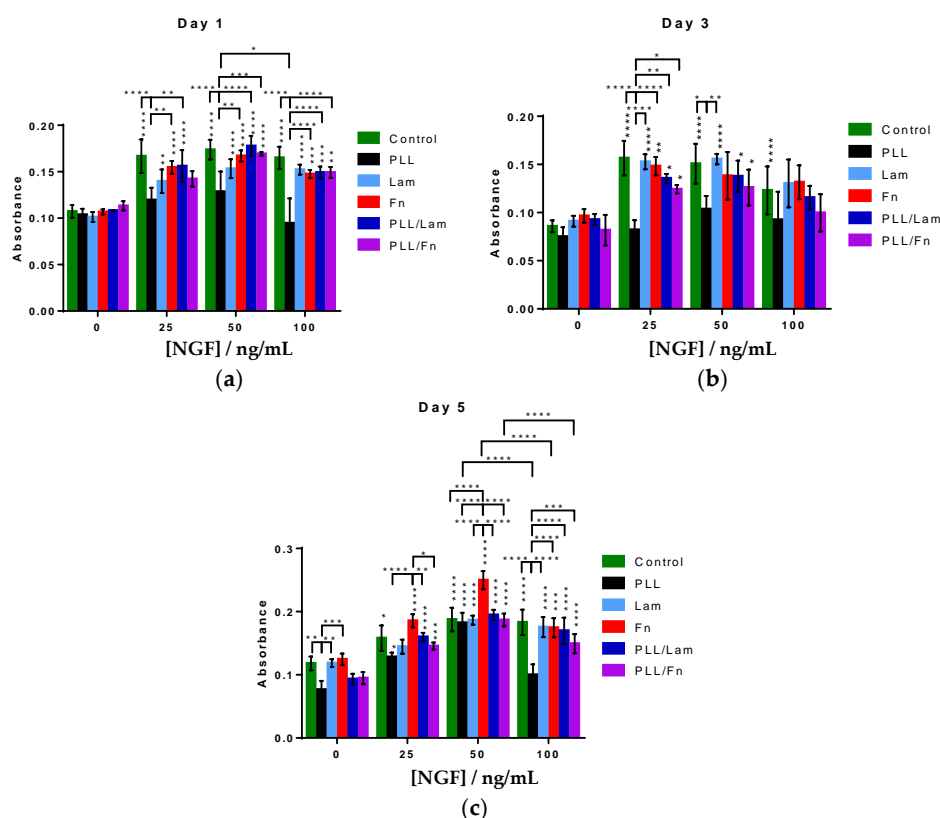
Figure 3. Comparative analysis of the proliferation of PC12 cells on substrata with different coatings in the presence of NGF solution. PC12 cells were grown over a period of 5 days in the presence of 0, 25, 50, or 100 ng/mL NGF. Incubation of PC12 cells on substratum surfaces in the presence of 50 ng/mL NGF resulted in an increased amount of attachment on day (**a**) 1, (**b**) 3 and (**c**) 5 compared to the other NGF solutions. Results are presented as the mean $\pm$ standard deviation. Unless otherwise specified, statistically significant differences in cell proliferation grown on the different substrata are shown versus the absence of NGF solution. "*" indicates the degree of statistically significant differences.

After the 5th day, cell proliferation was found to increase with increasing NGF concentration for all substrata. Cells incubated in the presence of substrata coated with PLL, Fn and PLL/Fn, and 100 ng/mL NGF exhibited a statistically significant decrease in proliferation compared to that observed in the presence of 50 ng/mL NGF.

3.4. Neurite Outgrowth

The neurite outgrowth was evaluated for individual cells, grown under different experimental conditions. The results are presented in Figure 4. A comparative analysis of these data indicated that increases in NGF concentration stimulated the outgrowth of neurites, despite the metabolic activity of the cells being greater at 50 ng/mL (Figure 3). It was also found that substrata with two-component coatings stimulated the outgrowth of neurites in the presence of a 100 ng/mL NGF solution (Figure 4). PC12 cells incubated in the presence of substrata with or without a single coating showed reduced levels or no outgrowth of neurites, most likely because of low cell attachment occurring on these surfaces. The substrata possessing dual component coatings stimulated the differentiation of neurites (Figure 4) after cell proliferation had been arrested (in the presence of 100 ng/mL NGF) after the 5th day of incubation (Figure 3).
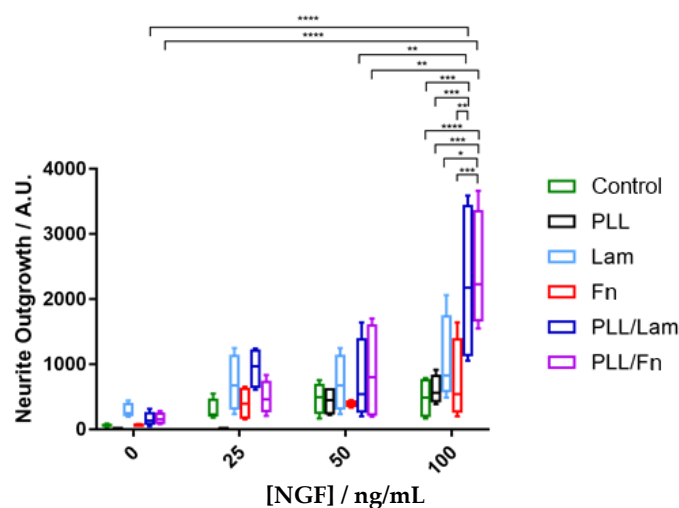
Figure 4. Quantification of neurite extension. The PC12 cells were grown on various coatings over a period of five days and in the presence of 0, 25, 50, and 100 ng/mL NGF. Over fifty fields of view were analysed for each condition. The results indicated a two-fold greater neurite outgrowth occurring on substrata containing the dual-component coatings of poly-L-lysine/laminin and poly-L-lysine/fibronectin with increasing NGF concentrations. Results are presented as minimum, 1st quartile, median, 3rd quartile, and maximum. "*" indicates the degree of statistically significant differences.

4. Discussion

The results of this study have demonstrated that PC12 cells incubated in the presence of substrata with dual-component coatings composed of PLL/Lam or PLL/Fn exhibited enhanced attachment, proliferation, and outgrowth of neurites. It is likely that this enhancement has occurred because PLL offers an increased number of cationic sites that can bind to the ionic sites present on the polystyrene surfaces of the tissue culture wells via hydrogen bonding or electrostatic interactions (Figure 5A). The glycoproteins, while effectively binding to PLL via electrostatic interactions (Fn and Lam isoelectric point of 5.5–6.0 [27] and 6.4 [28], respectively (Figure 5B,C)), also provided specific binding sites for the PC12 cells, allowing greater levels of cell attachment to take place [29], because cell surface receptors that promote cellular adhesion to extracellular matrices [30] are known to facilitate adherence the PC12 cells [30]. It was also demonstrated that the cell attachment domain of Fn consists of potential chains

of β-turns, which form the most hydrophilic region for cell attachment [29]. The integrin binding domain present on Lam [27] can bind with the integrin receptors present on the surface of PC12 cells (Figure 5C), resulting in adhesion and the initiation of cell differentiation. The PC12 cells strongly attached to the substrata containing a PLL coating due to the negatively-charged cell membrane and nonspecific electrostatic interactions with the highly positively-charged PLL surface (Figure 5A) [24]. The single-component coatings composed of only glycoproteins were most likely not able to support a robust attachment onto the surfaces of the tissue culture wells because of the weak binding affinity of this protein to the well surface. As a result, the PC12 cells would not have been able to withstand the washing procedures taking place during the incubation period.
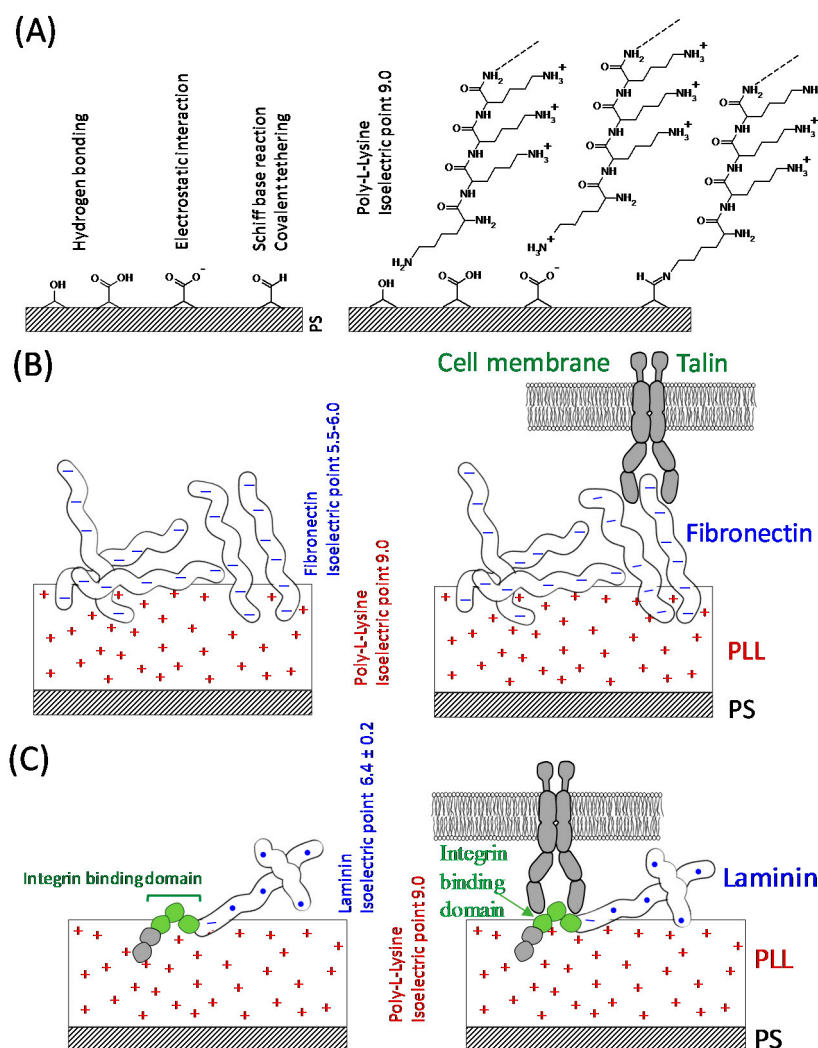
Figure 5. Schematic interpretation of the bio-interfaces of the PC12 cells undergoing attachment onto the substratum samples. (**A**) Possible chemical interactions between the polystyrene substratum and the coating materials. The aldehyde and ketone groups present on the surface of polystyrene undergo a Schiff base reaction and bind covalently with the amine groups. (**B**) negatively-charged fibronectin (pI 5.5–6.0) binding to the positively charged poly-L-lysine coating via electrostatic interactions. (**C**) laminin (pI 6.4) with a net negative charge also binds electrostatically to the poly-L-lysine layer. Laminin interacts with the PC12 cell surface receptors via the integrin binding domain.

5. Conclusions

In summary, substrata containing the two-component coatings of PLL/Lam and PLL/Fn in the presence of 100 ng/mL NGF solution were found to result in the greatest levels of attachment of PC12 cells followed by early stimulation of cell differentiation and neurite outgrowth.

Author Contributions: Elena P. Ivanova and Anna Orlowska conceived and designed the experiments; Anna Orlowska, Pallale Tharushi Perera and Huu Khuong Duy Nguyen performed the experiments; Anna Orlowska, Pallale Tharushi Perera, Mohammad Al Kobaisi, Andre Dias, and Elena P. Ivanova analyzed the data; Pallale Tharushi Perera, Anna Orlowska, Shahram Ghanaati, Vladimir Baulin, Russell J. Crawford and Elena P. Ivanova wrote the paper.

Conflicts of Interest: The authors declare no conflict of interest.

References

1. Jesky, R.; Chen, H. The neuritogenic and neuroprotective potential of senegenin against A b-induced neurotoxicity in PC12 cells. *BMC Complement. Altern. Med.* **2016**, *16*, 26. [CrossRef]
2. Westerink, H.R.; Ewing, A.G. The PC12 cell as model for neurosecretion. *Acta Physiol.* **2008**, *192*, 273–285. [CrossRef] [PubMed]
3. Gordon, J.; Amini, S.; White, M.K. General overview of neuronal cell culture. *Methods Mol. Biol.* **2013**, *1078*, 1–8. [PubMed]
4. Fuji, D.K.; Massoglia, S.L.; Savion, N.; Gospodarowicz, D. Neurite outgrowth and protein synthesis by PC12 cells as a function of substratum and nerve growth factor. *J. Neurosci.* **1982**, *2*, 1157–1175.
5. Akeson, R.; Warren, S.L. PC12 adhesion and neurite formation on selected substratums are inhibited by some glycosaminoglycans and a fibronetion-derived tetrapeptide. *Exp. Cell Res.* **1986**, *162*, 347–362. [CrossRef]
6. Attiah, G.D.; Kopher, R.A.; Desai, T.A. Characterization of PC12 cell proliferation and differentiation-stimulated by ECM adhesion proteins and neurotrophic factors. *J. Mater. Sci. Mater. Med.* **2003**, *14*, 1005–1009. [CrossRef] [PubMed]
7. Kleinman, H.K.; Luckenbill-Edds, L.; Cannon, F.W.; Sephel, G.C. Use of extracellular matrix components for cell culture. *Anal. Biochem.* **1987**, *166*, 1–13. [CrossRef]
8. Ergin, V.; Erdogan, M.; Menevse, A. Regulation of shootin1 gene expression involves ngf-induced alternative splicing during neuronal differentiation of PC12 cells. *Sci. Rep.* **2015**, *5*, 17931. [CrossRef] [PubMed]
9. Ogra, Y.; Tejima, A.; Hatakeyama, N.; Shiraiwa, M.; Wu, S.; Ishikawa, T.; Yawata, A.; Anan, Y.; Suzuki, N. Changes in intracellular copper concentration and copper-regulating gene expression after PC12 differentiation into neurons. *Sci. Rep.* **2016**, *6*, 33007. [CrossRef] [PubMed]
10. Boczek, T.; Kozaczuk, A.; Ferenc, B.; Kosiorek, M.; Pikula, S.; Zylinska, L. Gene expression pattern in PC12 cells with reduced PMCA2 or PMCA3 isoform: Selective up-regulation of calmodulin and neuromodulin. *Mol. Cell. Biochem.* **2012**, *360*, 89–102. [CrossRef] [PubMed]
11. Marino, A.; Ciofani, G.; Filippeschi, C.; Pellegrino, M.; Pellegrini, M.; Orsini, P.; Pasqualetti, M.; Mattoli, V.; Mazzolai, B. Two-photon polymerization of sub-micrometric patterned surfaces: Investigation of cell-substratum interactions and improved differentiation of neuron-like cells. *ACS Appl. Mater. Interfaces* **2013**, *5*, 13012–13021. [CrossRef] [PubMed]
12. Cowley, S.; Paterson, H.; Kemp, P.; Marshall, C.J. Activation of MAP kinase is necessary and sufficient for PC12 differentiation and for transformation of NIH 3T3 cells. *Cell* **1994**, *77*, 841–852. [CrossRef]
13. Shafer, J.T.; Atchison, W.D. Transmitter, ion channel and receptor properties of pheochromocytoma (PC12) cells: A model for neurotoxicological studies. *Neurotoxicology* **1991**, *12*, 473–492. [PubMed]
14. Chen, T.-I.; Chiu, H.-W.; Pan, Y.-C.; Hsu, S.-T.; Lin, J.-H.; Yang, K.-T. Intermittent hypoxia-induced protein phosphatase 2A activation reduces PC12 cell proliferation and differentiation. *J. Biomed. Sci.* **2014**, *21*, 1–11. [CrossRef] [PubMed]
15. Pandey, A.; Singh, P.; Jauhari, A.; Singh, T.; Khan, F.; Pant, A.B.; Parmar, D.; Yadav, S. Critical role of the miR-200 family in regulating differentiation and proliferation of neurons. *J. Neurochem.* **2015**, *133*, 640–652. [CrossRef] [PubMed]

16. Connolly, L.J.; Green, S.A.; Greene, L.A. Comparison of rapid changes in surface morphology and coated pit formation of PC12 cells in response to nerve growth factor epidermal growth factor and dibutyryl cyclicl AMP. *J. Cell Biol.* **1984**, *98*, 457–465. [CrossRef] [PubMed]

17. Tomaselli, J.K.; Damsky, C.H.; Reichardt, L.F. Purification and characterization of mammalian integrins expressed by a rat neuronal cell line (PC12) evidence that they function as α/β heterodimeric receptors for laminin and type IV collagen. *J. Cell Biol.* **1988**, *107*, 1241–1252. [CrossRef] [PubMed]

18. Garcia-Parra, P.; Cavaliere, F.; Maroto, M.; Bilbao, L.; Obieta, I.; de Munain, A.L.; Álava, J.I.; Izeta, A. Modeling neural differentiation on micropatterned substratums coated with neural matrix components. *Front. Cell. Neurosci.* **2012**, *6*, 1–12. [CrossRef] [PubMed]

19. Nečas, D.; Klapetek, P. Gwyddion: An open-source software for SPM data analysis. *Open Phys.* **2012**, *10*, 181–188. [CrossRef]

20. Gadelmawla, E.S.; Koura, M.M.; Maksoud, T.M.A.; Elewa, I.M.; Soliman, H.H. Roughness parameters. *J. Mater. Process. Technol.* **2002**, *123*, 133–145. [CrossRef]

21. Schindelin, J.; Arganda-Carreras, I.; Frise, E.; Kaynig, V.; Longair, M.; Pietzsch, T.; Preibisch, S.; Rueden, C.; Saalfeld, S.; Schmid, B.; et al. Fiji: An open-source platform for biologicical-image analysis. *Nat. Methods* **2012**, *9*, 676–682. [CrossRef] [PubMed]

22. Freire, E.; Gomes, F.C.; Linden, R.; Neto, V.M.; Coelho-Sampaio, T. Structure of laminin substratum modulates cellular signalling for neuritogenesis. *J. Cell Sci.* **2002**, *115*, 4867–4876. [CrossRef] [PubMed]

23. Rogers, S.L.; Letourneau, P.C.; Palm, S.L.; McCarthy, J.; Furcht, L.T. Neurite extension by peripheral and central nervous system neurons in response to substratum-bound fibronectin and laminin. *Dev. Biol.* **1983**, *98*, 212–220. [CrossRef]

24. Mazia, D.; Schatten, G.; Sale, W. Adhesion of cells to surfaces coated with polylysine. *J. Cell Biol.* **1975**, *66*, 198–200. [CrossRef] [PubMed]

25. Ajioka, I. Coordination of proliferation and neuronal differentiation by the retinoblastoma protein family. *Dev. Growth Differ.* **2014**, *56*, 324–334. [CrossRef] [PubMed]

26. Berridge, M.V.; Tan, A.S. Characterization of the cellular reduction of 3-(4,5-dimethylthiazol-2-yl)-2,5-diphenyltetrazolium bromide (MTT):subcellular localization, substratum dependance, and involvement of mitochondrial electron transport in MTT reduction. *Arch. Biochem. Biophys.* **1993**, *303*, 474–482. [CrossRef] [PubMed]

27. Vartio, T. Characterization of the binding domains in the fragments cleaved by cathepsin g from human plasma fibronectin. *FEBS J.* **1982**, *123*, 223–233. [CrossRef]

28. Paulsson, M.; Deutzmann, R.; Timpl, R.; Dalzoppo, D.; Odermatt, E.; Engel, J. Evidence for coiled-coil α-helical regions in the long arm of laminin. *EMBO J.* **1985**, *4*, 309–316. [PubMed]

29. Pierschbacher, D.M.; Ruoslahti, E. Cell attachment activity of fibronectin can be duplicated by small synthetic fragments of the molecule. *Nature* **1984**, *309*, 30–33. [CrossRef] [PubMed]

30. Hynes, R.O. Integrins: Versatility, modulation and signalling in cell adhesion. *Cell* **1992**, *69*, 11–25. [CrossRef]

Annex III

Original article published as collaborative project in the scope of ITN- SNAL:

Chia-Lai, P. J., Orlowska, A., Al-Maawi, S., **Dias, A**., Zhang, Y., Wang, X., Zender, N., Sader, R., Kirkpatrick, C. J., Ghanaati, S. (2018) Sugar-based collagen membrane cross-linking increases barrier capacity of membranes. Clin Oral Investig. 22, 4, 1851-1863;

Annex III

ORIGINAL ARTICLE

CrossMark

Sugar-based collagen membrane cross-linking increases barrier capacity of membranes

Po-ju Chia-Lai [1] · Anna Orlowska [1] · Sarah Al-Maawi [1] · Andre Dias [1] · Yunxin Zhang [1] · Xuejiu Wang [1,2] · Niklas Zender [1] · Robert Sader [1] · C. James Kirkpatrick [1] · Shahram Ghanaati [1]

Abstract

Objectives This study examines the permeability and barrier capacity of a sugar cross-linked resorbable collagen membrane ex vivo and in vivo.

Materials and methods In an ex vivo study, injectable platelet-rich fibrin (i-PRF), a peripheral blood-derived human leukocyte-and-platelet-rich plasma was used to analyze membrane permeability. in vivo subcutaneous implantation in Wistar rats ($n = 4$ per time point and group) was used to investigate the barrier capacity of the membrane. The induced in vivo cellular reaction was evaluated at 3, 15, and 30 days and compared to sham OP (control) without biomaterial using histological, immunohistochemical, and histomorphometric methods.

Results Ex vivo, the membrane was impenetrable to leukocytes, platelets, and fibrin from peripheral human blood concentrate (PRF). In vivo, the membrane maintained its structure and remained impervious to cells, connective tissue, and vessels over 30 days. CD-68-positive cell (macrophage) numbers significantly decreased from 3 to 15 days, while from day 15 onwards, the number of multinucleated giant cells (MNGCs) increased significantly. Correspondingly, a rise in implantation bed vascularization from 15 to 30 days was observed. However, no signs of degradation or material breakdown were observed at any time point.

Conclusion Ex vivo and in vivo results showed material impermeability to cellular infiltration of human and murine cells, which highlights the membrane capacity to serve as a barrier over 30 days. However, whether the induced MNGCs will lead to material degradation or encapsulation over the long term requires further investigation.

Clinical relevance The data presented are of great clinical interest, as they contribute to the ongoing discussion concerning to what extent an implanted material should be integrated versus serving only as a barrier membrane.

Keywords Collagen · Guided bone regeneration · Guided tissue regeneration · Foreign body giant cell reaction · Multinucleated giant cells · Barrier membrane

Introduction

Guided bone regeneration (GBR) is a widely used procedure in different surgical fields, especially in oral and maxillofacial surgery [1]. The principle aim is to substitute and support impaired regions due to diseases or traumatic events and to enhance the amount of bone available, such as prior to implant therapy in oral surgery. Since the rate of bone formation is slower than the rate of fibrogenesis, the role of the membrane is first and foremost to prevent the ingrowth of epithelium and connective tissue into the augmentation region [2–4]. Further requirements are to act as a place holder, to maintain space for delayed osteogenesis, and to stabilize the wound in order to achieve primary wound closure [5].

Currently, two types of membranes are commercially available: resorbable and non-resorbable membranes. In the 1990s, non-resorbable membranes, such as expanded polytetrafluoroethylene (e-PTFE), titanium mesh, and titanium-reinforced PTFE, were used in the GBR technique. Although these barriers proved very effective in preventing the invasion of soft tissue physically [6, 7], their technique sensitivity and increased patient

✉ Shahram Ghanaati
shahram.ghanaati@kgu.de

1 Department for Oral, Cranio-Maxillofacial and Facial Plastic Surgery, FORM (Frankfurt Orofacial Regenerative Medicine) Lab, University Hospital Frankfurt Goethe University, Theodor-Stern-Kai 7, 60590 Frankfurt am Main, Germany

2 Department of Oral and Maxillofacial Plastic and Trauma surgery, Capital Medical University School of Stomatology, Beijing, China

morbidity (due to obligatory membrane retrieval) were major limitations. To avoid these drawbacks, biomaterials development has been focused on generating resorbable membranes. Among these, collagen, as a ubiquitous molecule, has shown suitable and beneficial properties. Consequently, collagen-based biomaterials have demonstrated favorable GBR results [8] while bypassing the shortcomings of non-resorbable membranes. However, collagen membranes are predisposed to degradation within their implantation beds [9], which undermines their ability to function as true barriers.

During wound healing, different inflammatory cells are involved in the regeneration process of the affected tissue as a cellular response to the injury. In the early wound healing stage and during hemostasis, platelet accumulation occurs to build a platelet plug, which then becomes a fibrin matrix [10]. This phase is then followed by the recruitment of different physiologic mononuclear cells, such as leukocytes and their subtypes, which allows phagocytosis of contaminated and necrotic tissue, first by neutrophils and then by macrophages [10, 11]. Additionally, platelets and leukocytes release numerous growth factors to mediate vascularization [12] and allow the shift to the process of new tissue formation by recruiting keratinocytes and fibroblasts [10].

However, the implantation of biomaterials within the defect area adds an additional factor in the processes of wound healing and tissue regeneration. After biomaterial implantation, an interaction with the biomaterial occurs that results in a biomaterial-specific cellular reaction.

Previously, our group conducted a series of in vivo studies to analyze the cellular reactions towards various collagen membranes of different origins and attributes using a subcutaneous implantation model in small animals. The collected data have shown that, generally, there are two different types of cellular reactions that most likely depend on the physicochemical properties and the processing techniques of the biomaterials. Membranes that induced a physiological reaction by means of mononuclear cells underwent an integration process and maintained their structure over a period of 60 days [7, 13]. This process was revealed in non-cross-linked bilayered collagen membranes of porcine origin composed of collagen types I and III [7], as well as in a collagen-based matrix that included collagen types I and III harvested from porcine peritoneum and skin [13]. Furthermore, the main reaction towards these two collagen-based materials was dominated by mononuclear cells, which ultimately led to its integration within the host tissue without material breakdown [13]. In addition, the cellular reaction in translational clinical cases, including histological evaluation of human samples, corresponded to the in vivo observed outcomes [13].

Other biomaterials demonstrated a different type of cellular reaction that included non-physiological cells, such as multinucleated giant cells (MNGCs), which are a sign of a foreign body reaction [14]. In a comparative in vivo study, two collagen-based biomaterials with different thicknesses were analyzed in a subcutaneous implantation model. Both the thick collagen matrix and the thin bilayered collagen membrane induced the formation of MNGCs, a manifestation of a foreign body reaction [14, 15], which not only led to increased vascularization in the implantation regions but also to membrane breakdown in terms loss of the native structure [14]. Similarly, another in vivo study investigated the cellular responses towards two non-cross-linked collagen-based biomaterials, both of porcine origin but differing in their harvesting compartments and thicknesses, and found that they underwent disintegration by the induction of MNGCs, which led to a breakdown after 30 days in both biomaterials [15]. Therefore, the induced cellular reaction decisively influences the degradation and regeneration process of collagen-based biomaterials and their role as a barrier membrane.

To further increase the resistance of collagen-based biomaterials to degradation, various chemical and physical cross-linking methods, such as ultraviolet light, glutaraldehyde, and enzymatic ribose cross-linking, have been used to boost the biomechanical properties of the collagen fibers [16]. Various studies have shown that supplementary cross-linking confers stability on collagen membranes after implantation [17–19]. However, cross-linking was also associated with foreign body reaction and fibrosis, which might be due to chemical manipulation of the collagen structure [20]. Recently, GLYMATRIX™ technology (Datum Dental Ltd., 1 Bat Sheva Street, Lod 7120101 Israel), a novel technique which uses ribose—a naturally occurring sugar molecule—to cross-link collagen, has been developed [21]. The manufacturing process involves the extraction of collagen into monomeric fibrils, which are then reconstructed and cross-linked to form an improved collagen-based biomaterial. In this study, the capacity of such a sugar cross-linked collagen membrane, OSSIX® PLUS (OS, REGEDENT, Zurich, CH) to serve as a barrier was evaluated in vivo using a subcutaneous implantation model in Wistar rats. Special interest was directed at the induced cellular reaction in terms of cell types, membrane permeability, vascularization, and degradation patterns. Additionally, a blood concentrate system of injectable platelet-rich fibrin (i-PRF), which contains numerous human peripheral blood cells, was used for evaluation of membrane permeability ex vivo.

Materials and methods

OSSIX® PLUS membrane

OSSIX® PLUS membrane (OS) is a sugar cross-linked resorbable collagen membrane derived from porcine tendons [22]. The native tissue undergoes a series of purification

processes to isolate monomeric collagen and to remove all potential immunogenic tissue remnants. Subsequently, the monomeric collagen is reconstituted into collagen fibrils and then glycated with ribose, a naturally occurring sugar, using GLYMATRIX™ technology [21]. Sterilization was achieved with ethylene oxide. The collagen membrane is CE-marked. According to the manufacturer, OS maintains barrier functionality for 4–6 months. Furthermore, since it is purported to be resistant to the oral environment, membrane exposure during implantation will not impede wound healing or guided bone regeneration (GBR) [22]. The biomaterial is specified to be impermeable to cells, but permits the passage of fluid and plasma proteins.

2.2 The study was designed in two separate parts, including ex vivo evaluation and in vivo evaluation:

Experimental design of the ex vivo study part

Injectable platelet-rich fibrin Platelet-rich fibrin (PRF) is a blood concentrate system obtained by the centrifugation of human peripheral blood [23]. This system exists in a solid [23] and a liquid form [24]. PRF is a fully autologous concentrate system that does not require the addition of any external chemicals or anticoagulants. After blood collection, the tubes are immediately centrifuged using a specific, established centrifugation protocol [25]. In the case of the liquid, injectable PRF (i-PRF), the resultant blood concentrate contains a high number of platelets, leukocytes, and plasma proteins suspended in a soluble fibrinogen matrix [24]. Because i-PRF is not treated with anticoagulants, the physiological co-agulation process is not inhibited. Therefore, i-PRF forms a clot of cell-loaded fibrin after 10–15 min.

I-PRF preparation and application In the ex vivo section of this study, three healthy volunteers between 18 and 60 years of age, and who were not under any anticoagulant therapy, donated peripheral blood for research purposes. All three volunteers gave written informed consent beforehand. From each participant, venous blood was collected in four 10-ml sterile plastic tubes (Process for PRF, Nice, France). The tubes were immediately centrifuged in a pre-programmed centrifuge (Duo centrifuge, Process for PRF, Nice, France) according to the i-PRF centrifugation protocol (10 ml, 700 rpm, 60 ×g, for 3 min) [25]. After this centrifugation process, a multiphasic liquid consisting of a yellowish-orange upper phase and a reddish lower phase was obtained. The former is i-PRF, whereas the latter includes the remaining blood constituents. Using a blunt needle, 1–2 ml of the i-PRF liquid was collected into a 5-ml syringe (Injekt®, B. Braun Medical Inc., Bethlehem, PA, USA) for further use. In the process, care was taken to prevent the two phases from mingling or an accidental uptake of the lower phase.

Four 10 × 10-mm samples of OS were first placed inside a 4 × 6 cell culture plate and then covered by 500 μl i-PRF. After 15 min at room temperature, the i-PRF liquid formed fibrin clots on the OS samples. These OS membrane-fibrin clot samples were then fixed in 4% paraformaldehyde for 24 h to allow for subsequent histological analysis. This experiment was performed in triplicate at independent time points.

Experimental design of the in vivo study part

This study was approved by the Committee on the Use of Live Animals in Teaching and Research of the State of Hessen, Germany. A total of 24 Wistar rats were obtained from Charles River Laboratories (Sulzfeld, Germany) and housed in the Laboratory Animal Unit, Institute of Pathology, Goethe University Frankfurt, Germany. The animals were allowed an acclimation period of 1 week, which enabled them to become accustomed to the new laboratory environment before the experiments began. Throughout the entire study period, the animals were fed regularly with mouse pellets (Laboratory Rodent Chow, Altromin, Lage, Germany) and given water ad libitum. Artificial light–dark cycles of 12 h each simulated day and night rhythms.

Based on the study design, the 24 rats were first assigned randomly into two groups. The animals in the first group ($n = 4$ animals/time point) were implanted with OS, whereas the second group ($n = 4$ animals/time point) served as a sham-operated control in order to evaluate the inflammatory pattern during wound healing without biomaterial implantation. The evaluated time points were 3, 15, and 30 days after implantation. The implantation of OS was performed under sterile conditions in accordance with previously established subcutaneous implantation methods as previously described [13]. All animals survived the operational procedure and through the respective evaluation time points without any complications.

Tissue preparation for histology and histochemistry After explanation at the designated time points, tissue samples as well as ex vivo samples were processed by the methods described in previously published studies [26–28]. First, the samples were fixed in 4% neutral buffered formalin for 24 h. These samples were then placed into embedding cassettes (Histosette, VWR, Deutschland) and dehydrated in baths of progressively concentrated ethanol (70–100%) before alcohol clearance with xylene. Finally, the tissue segments were impregnated with molten paraffin wax and embedded into paraffin blocks. After sufficient cooling, the paraffin blocks were cut with a rotatory microtome (Rotationsmikrotom RM2255, Leica, Germany) to produce serial sections of 3-μm thickness. To evaluate the tissue sections under a microscope, they were stained as follows: the first section was stained with Mayer's hematoxylin and eosin (H&E), while the second section was

stained with Azan. The third section was stained with Masson's trichrome stain, and the fourth section underwent tartrate-resistant acid phosphatase (TRAP) staining. The latter stain was specifically used to identify TRAP activity in target cells. The fifth and sixth and seventh sections were stained immunohistochemically with anti-mouse CD-31, CD-68, and vWF respectively, as previously described [13, 15]. In brief, immunohistochemistry was conducted with a Lab VisionTM Autostainer 360-2D (ThermoFisher Scientific, Germany). After deparaffinization, the slides were pre-treated with citrate buffer and proteinase K, followed by H2O2 (UltraVisionTM Quanto Detection System, ThermoFisher Scientific, Germany) and avidin and biotin blocking solutions (Avidin/Biotin Blocking Kit, Vector Laboratories, US). The first antibody used was anti-CD-68 (MCA341GA; 1:400; 30 min), anti-CD-31 (orb10314; 1:200; 2 h), or anti-vWF (ab6994; 1:500; 2 h), whereas the second antibody was goat anti-rabbit IgG-B (sc-2040, 1:200, Santa Cruz Biotechnology, USA). Subsequently, the avidin-biotin-peroxidase complex (ABC) (30 min) and the Histostain-Plus IHC Kit including AEC (20 min) were applied (ThermoFisher Scientific, Germany). Counterstaining was performed using Mayer's hematoxylin. CD-31 and vWF highlight murine blood vessels, while CD-68 detects macrophages in the tissue sections. The negative control for the immuno-histochemical staining used was the absence of incubation for primary antibody, while the positive control was applied according to the manufacturer's instruction (anti-CD-31, rat lung; Anti-vWF, human tongue; and anti-CD-68, rat lymph node).

Qualitative histological analysis

Systematic histological assessment was performed by means of a Nikon ECLIPSE 80i microscope (Nikon, Tokyo, Japan) equipped with a motorized stage (ProScan III, Prior, Rockland, MA, USA) and NIS Elements software (Nikon, Tokyo, Japan) as described in preceding publications [14]. Qualitative and quantitative histological analysis focused on the cellular reaction and inflammatory pattern towards the implanted biomaterial, vascularization of the implantation bed, signs of fibrosis, encapsulation, and membrane degradation.

Quantitative histological analysis

Membrane thickness

Adopting the same histomorphometry methods as mentioned in earlier studies [27], the peri-implant tissue of each animal was first digitized prior to histomorphometric analysis. Initially, a total scan including 100–130 individual micrographs was taken automatically by the Nikon ECLIPSE 80i

microscope. This was made possible by the motorized stage, which moved automatically within coordinates specified in the NIS Elements software. These single images were then compounded to generate a single large total scan at ×100 magnification. The thickness of the OS membrane of each animal at each of the three time points (3, 15, and 30 days) was then measured at up to 15 distinct points along its length. The mean of these measurements was calculated as the absolute membrane thickness in micrometers. The values obtained from the later time points were also compared to that of day 3, assigned to a value of 100%.

Number of multinucleated giant cells and CD-68-positive mononuclear cells

To analyze the material-associated MNGCs histomorphometrically, TRAP- and CD-68-stained slides were first converted to total scan digital images as previously mentioned. The "annotations and measurements" function of the NIS Elements software was used to manually count the numbers of MNGCs and their subpopulations (TRAP-positive and -negative giant cells), as well as CD-68-positive cells, separately. The respective cell numbers were then computed in relation to the implantation area (MNGCs/mm^2; CD-68/mm^2), and statistical comparison of the different time points was performed to determine the tissue response elicited by OS over the course of the study.

Measurements of membrane vascularization

In a similar fashion, after digitizing the peri-implant region in total scans, the prominently stained blood vessels were manually circumscribed with the area tool of the "annotations and measurements" function of the NIS Elements software. For comparison purposes, the vessel density (vessels/mm^2) and the percentage of vascularization were computed from the total number and total area of vessels in the implantation bed, respectively.

Statistical analysis

The results from the abovementioned histomorphometric analysis were presented as the means ± standard deviation and were evaluated for significant differences at the different time points using a one-way analysis of variance (ANOVA) using GraphPad Prism 6.0 software (GraphPad Software Inc., La Jolla, CA, USA). Differences were considered statistically significant if the P values were* < 0.05 and highly significant if the P values were, **< 0.01, and ***< 0.001 and ****<0.0001. The compiled data were plotted with GraphPad Prism 6.0 software to represent the results graphically.

Results

3.1 Ex vivo histological analysis

The OS membrane was easily identified and exhibited a highly dense structure without detectable pores. The interaction with the i-PRF revealed that no leukocytes or platelets from the i-PRF penetrated into the biomaterial. Instead, OS prevented the inflammatory cells from entering the membrane body. Moreover, the extracellular fibrin was not included within the biomaterial, which resulted in the formation of a cell-rich fibrin clot on both surfaces of the membrane (Fig. 1a, b).

3.2 In vivo histological and histomorphometric analysis

All tested animals survived their respective operations, and healing was uneventful. During the entire experiment, no animals were observed to have necrosis or signs of atypical inflammation.

#### 3.2.1 Tissue reaction to the OS membrane

The OS membrane was clearly visible within the murine subcutaneous implantation bed 3 days after implantation (Fig. 2a). It showed a homogeneous structure of densely packed collagen. Both surfaces of this compact membrane were lined with a layer of mononuclear cells (Fig. 2a, b), of which a large amount were CD-68-positive, i.e., macrophages. No penetration by peri-implant cells or extracellular matrix was noted at this time point (Fig. 4a, A1). Thus, the membrane per se was free of

cells. Single vessels were found within the peri-implantation area, but the membrane itself exhibited no vascularization (Fig. 3 A).

On day 15 post-implantation, the membrane did not show any signs of degradation (Fig. 2c, d). In comparison to day 3, more mononuclear cells were observed in the implantation bed (Fig. 5b), several of which were CD-68-positive (Fig. 4b, B1). Additionally, a small number of MNGCs located predominantly at the biomaterial-tissue interface was seen (Fig. 2d). A majority of these MNGCs was TRAP-negative (Fig. 5c). At this time point, the membrane maintained its structure, preventing cellular infiltration into the membrane central region. Moreover, connective tissue formation was observed only within the peri-implantation region, and no connective tissue ingrowth was detected within the membrane. Although micro-vessel formation was noted in proximity to the membrane, the membrane body itself remained avascular (Fig. 5a, Fig. 3b). Additionally, no signs of membrane breakdown were observed at this time point.

At day 30 after implantation, no evidence of degradation of the membrane was perceived (Fig. 2e). The membrane displayed a stable dense structure and inhibited cellular infiltration of all kinds. Instead, an organized, cell-rich connective tissue was seen on both membrane surfaces (Fig. 5e). In comparison to day 15, the number of mononuclear cells adjacent to the membrane increased significantly (Fig. 2e, f). These included CD-68-positive cells (Fig. 4c, C1). In addition, more biomaterial-adherent MNGCs were identified within the implantation region (Fig. 2f), which remained on the membrane surface and did not enter the biomaterial body. The majority of the MNGCs showed no TRAP expression. Nevertheless, no signs of membrane

Fig. 1 a The native structure of OS membrane ex vivo as a control in H&E staining at ×100 magnification. b i-PRF alone in H&E staining at ×200 magnification; asterisk = fibrin clot, black arrows = human leukocytes. c i-PRF alone; black arrows = human leukocytes, asterisk = fibrin clot in H&E staining ×600 magnification. d A cross section of the OS membrane treated with i-PRF in H&E staining at ×100 magnification. e The interface between i-PRF and OS in H&E staining at ×200 magnification; asterisk = fibrin clot, black arrows = human leukocytes. f Black arrows = human leukocytes in H&E staining ×600 magnification
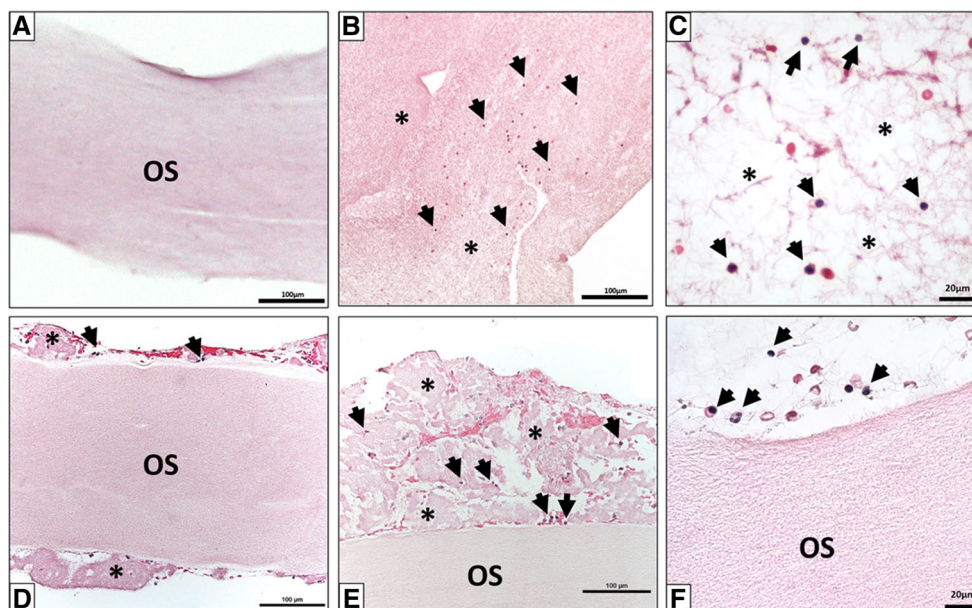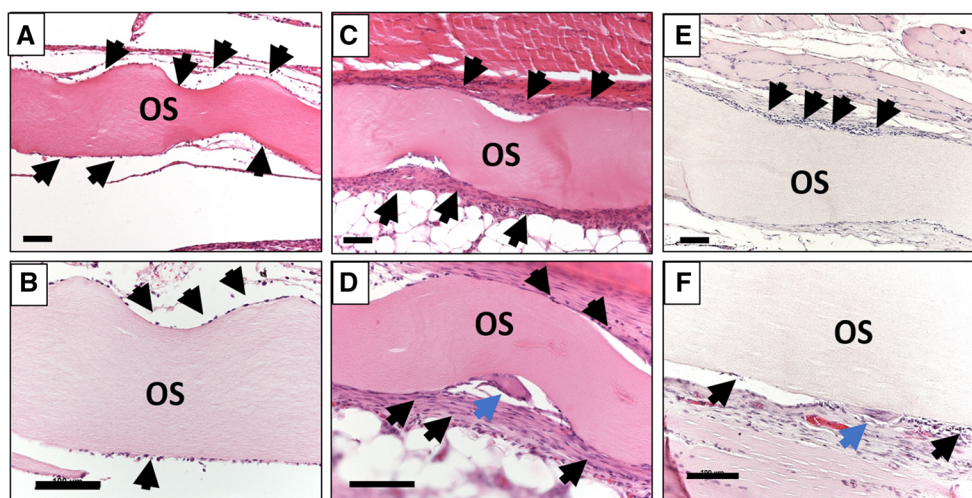
Fig. 2 **a** The membrane (OS) within the implantation bed on day 3. Mononuclear cells were detected on both membrane surfaces (black arrows). **b** Mononuclear cells on the membrane (OS) surface (black arrows) on day 3. **c** The membrane (OS) within the implantation region on day 15. There is an increased number of mononuclear cells on both membrane surfaces (black arrows). **d** Mononuclear cells (black arrows), as well as multinucleated giant cells (blue arrow) on the membrane surface (OS) on day 15. **e** The membrane within the implantation bed (OS) on day 30. **f** Mononuclear (black arrows) and multinucleated giant cells adhering to the membrane (OS) surface on day 30. (H&E staining; **a**, **c**, **e** at ×100 magnification; **b**, **d**, **f** at ×200 magnification; all scale bars = 200 μm)

breakdown were found (Fig. 5f). Although the membrane continued to be impermeable to cells and connective tissue, there were no indications that it was segregated from the surrounding tissue by encapsulation or fibrosis.

Fig. 3 The vascularization pattern over the investigation time points using immunohistochemical stains: **a–c** = anti-CD-31; × 200 magnification; scale bar = 100 μm. **d–f** = anti-vWF; ×00 magnification; scale bar = 20 μm. Black arrows indicate vessels and OS indicates the membrane
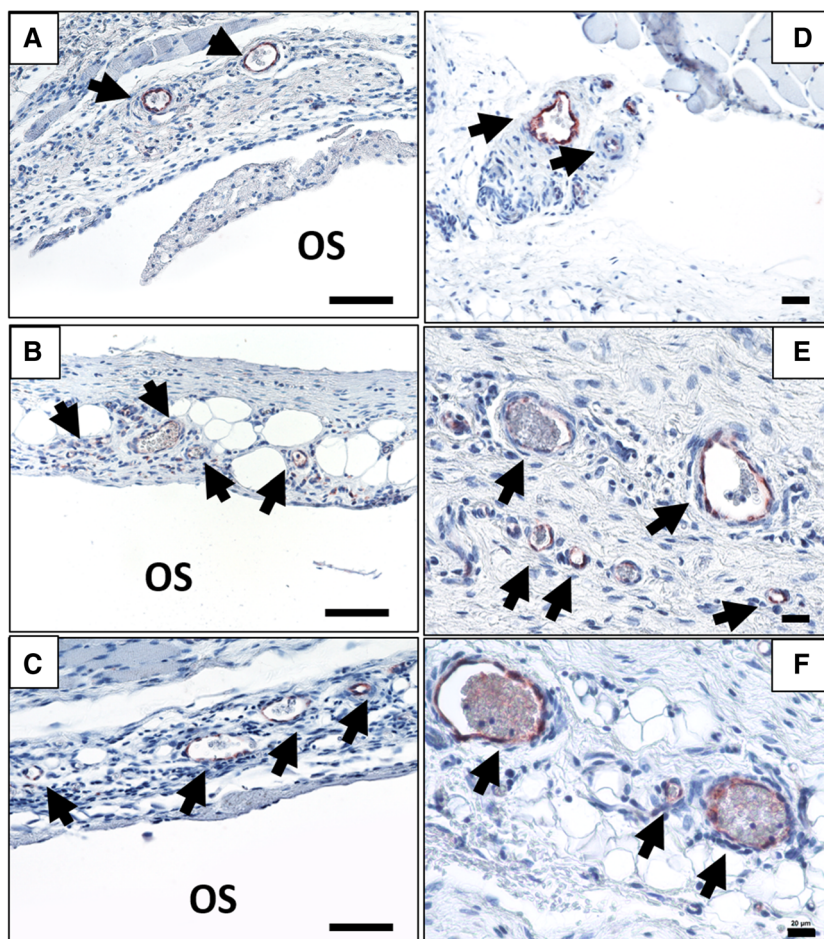
Fig. 4 The CD-68-positive cells on the biomaterial surface at day 3 (**a**; A1); day 15 (**b**; B1) and day 30 (**c**; C1). Black arrows = CD-68-positive mononuclear cells, i.e., macrophages. OS indicates the biomaterial. In **b** and **c**, the biomaterial was detached and washed during the staining process. **a**–**c** × 100 magnification; 100-μm scale bar. A1–C1 ×400 magnification; 20-μm scale bar
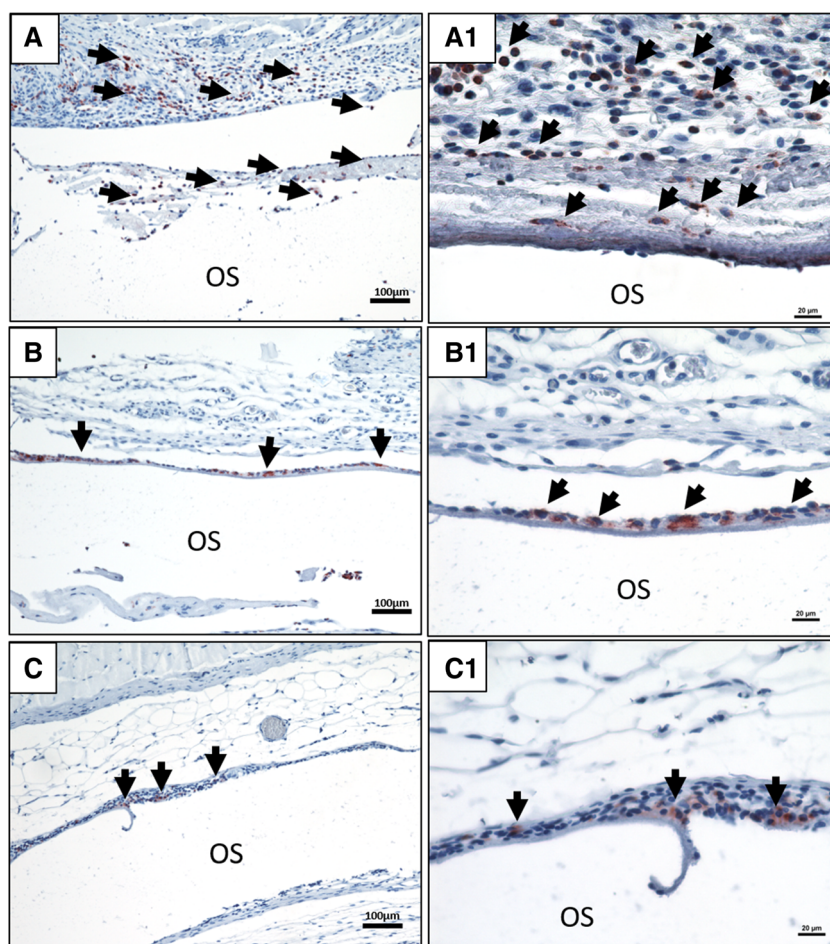
3.2.2 Histomorphometric results

Histomorphometric analysis of OS membrane thickness The histomorphometric analysis of the OS membrane revealed that there was no decrease in membrane thickness between day 3 and day 30 after implantation. In contrast, the measured membrane thickness showed a slight increase over the study period, which was not statistically significant (day $3 = 274.68 \pm 27.75$; day $15 = 287.59 \pm 27.83$; day $30 = 302.60 \pm 15.19$), (Fig. 6a). Due to the possibility of artifacts arising from the histological and implantation procedures, the membrane thickness was calculated as a percentage to obtain a more accurate evaluation. The thickness of day 3 was set at 100%, and all mean values of successive time points were calculated in relation to day 3. The percentage of thickness revealed a slight increase of the membrane thickness towards day 30. However, no statistically significant differences were detected over the duration of the study (day $15 = 104.70\% \pm 15.93\%$; day $30 = 110.11\% \pm 15.77\%$; Fig. 6b).

Histomorphometric analysis of CD-68-positive macrophages At day 3 post-implantation, the macrophage density in the peri-implant area was significantly higher than that of day

15 ($P < 0.1$) and day 30 ($P < 0.1$). There was no statistically significant increase in the density of the macrophages in the implantation bed between day 15 and day 30. A similar trend was observed within the control group, which showed that the number of macrophages decreased significantly from day 3 to 15, (day 3 vs. day 15 ($P < 0.5$); day 3 vs. day 30 ($P < 0.1$)). In contrast, there was no statistically significant difference between days 15 and 30 (data not shown). However, the number of macrophages within the OS group was significantly higher than that of the control group at all time points (day 3 ($P < 0.001$); day 15 ($P < 0.1$); day 30 ($P < 0.001$), Fig. 7b).

Histomorphometric analysis of multinucleated giant cells At day 3 after implantation, no MNGCs could be detected within the area of implantation. Their presence was first observed at day 15 after implantation. The number of MNGCs at day 15 was highly significant compared to day 3 ($P < 0.001$). Moreover, the majority of the MNGCs was TRAP-negative, and the difference between day 3 and day 15 was statistically significant ($P < 0.01$). The membrane-adherent TRAP-positive MNGCs at day 15 showed no statistical significance when compared between day 3 and day 15. However, at day 30, the total number of MNGCs increased significantly
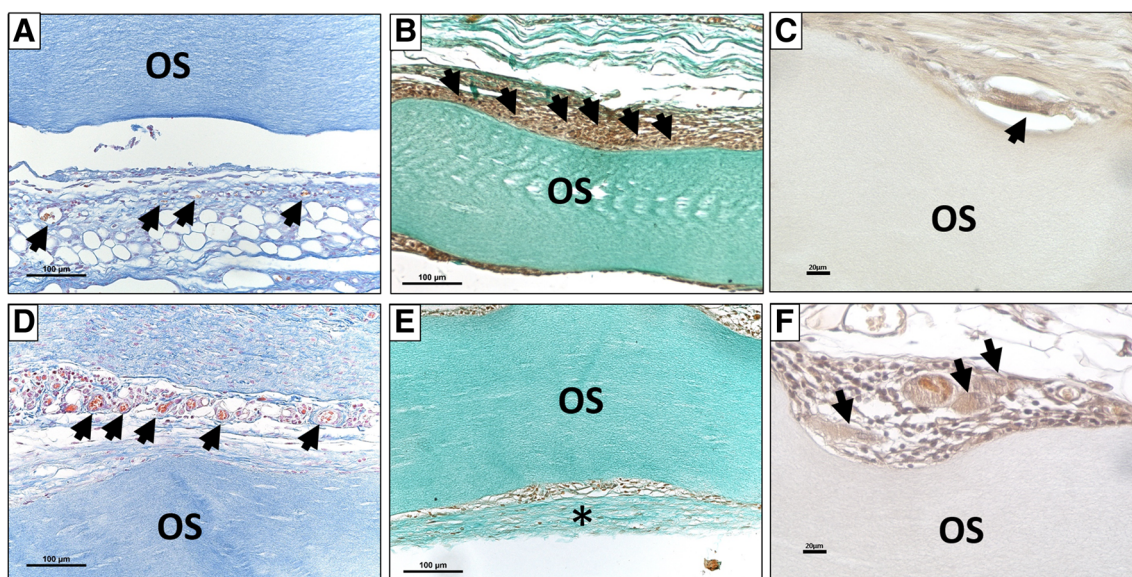
Fig. 5 Detailed representative micrographs on days 15 and 30. **a** Vessels (black arrows) were detected near the membrane (OS) at day 15, (Azan staining; ×200 magnification; scale bar = 100 μm). **b** Accumulation of mononuclear cells (black arrows) on the membrane (OS) surface at day 15, (Masson Goldner staining; ×400 magnification; scale bar = 20 μm). **c** TRAP-negative multinucleated giant cells (black arrows) adherent on the membrane (OS) surface at day 30 (TRAP staining; ×400 magnification; scale bar = 20 μm). **d** Increased numbers of vessels (black arrows) were detected in proximity to the membrane (OS) at day 30, (Azan staining; ×200 magnification; scale bar = 100 μm). **e** Formation of organized connective tissue including mononuclear cells (asterisk) on the membrane (OS) surface at day 30, (Masson Goldner staining; ×400 magnification; scale bar = 20 μm). **f** TRAP-negative multinucleated giant cell (black arrows) adherent on the membrane (OS) surface at day 30 (TRAP staining; ×400 magnification; scale bar = 20 μm)

compared to day 3 ($P < 0.0001$) and day 15 ($P < 0.0001$). Additionally, the number of TRAP-negative MNGCs was significantly higher than at day 3 ($P < 0.0001$) and day 15 ($P < 0.0001$). In contrast, the number of TRAP-positive MNGCs was notably constant, and there was no significant difference between day 3, day 15, and day 30 (Fig. 7a).

The control group showed no multinucleated giant cells at any time point.

Histomorphometric analysis of the implantation bed vascularization Histomorphometric evaluation of the implantation bed showed that no ingrowth of vessels into the membrane was detected at any time points during the study. The percentage of vascularization in the peri-implantation bed increased steadily over the course of the study. At day 3 after implantation, the percentage of vascularization was comparable to that of the control group. At day 15 post-implantation, there was no statistically significant increase in the vascularization percentage compared to day 3. In addition, no statistically significant difference was detected between the test group and the control group. However, at day 30, the percentage of vascularization was significantly higher in comparison to day 3 ($P < 0.0001$) and day 15 ($P < 0.001$), respectively. At this time point, the vascularization percentage in the test group was significantly higher than that in the control group ($P < 0.05$). Similarly, the percentage of vascularization increased gradually in the sham-operated groups as well (Fig. 6c).

The number of vessels detected per square millimeter at day 3 was significantly higher than that of the control group ($P < 0.01$). Comparing the values at day 15 to day 3, no statistically significant difference between the test groups was found. However, at day 15, the value in the test group was significantly higher than that of the control group ($P < 0.01$). Moreover, at day 30 post-implantation, there was a marked increase in the number of vessels per square millimeter. This value was highly statistically significant compared to both day 3 and day 15 ($P < 0.0001$). At this time point, the difference in vessel number per square millimeter was also highly significant compared to the control group ($P<0.0001$) (Fig. 7d).

Discussion

The present study evaluated a collagen membrane reinforced using a ribose cross-linking technique. The aim of the study was to analyze cellular permeability of this biomaterial ex vivo and its barrier capacity in vivo. Special interest was directed to the cellular reaction towards this biomaterial in terms of the induced cell types and vascularization and degradation pattern compared to the control sham operation group, which imitated the physiological wound healing process.

In the ex vivo part, the focus was placed on evaluating the cellular permeability of the biomaterial. Looking at the clinical scenario, after biomaterial application, the membrane first
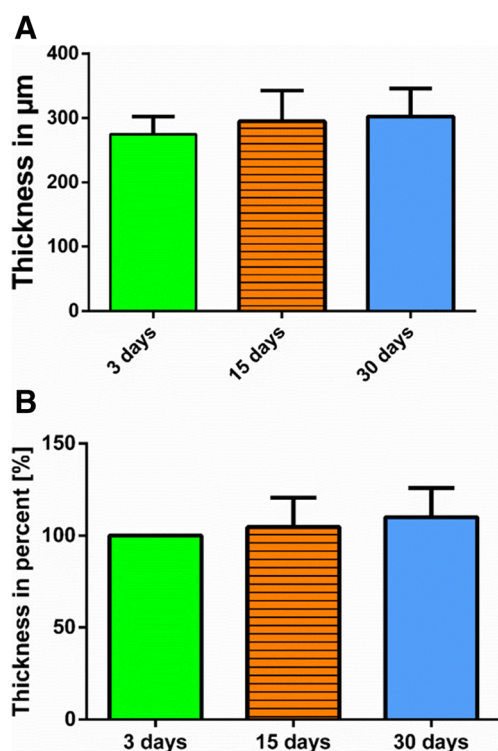
Fig. 6 **a** Illustration of the histomorphometric analysis of the membrane thickness in micrometers. **b** Illustration of the histomorphometric analysis of the membrane thickness as a percentage relative to day 3

comes in contact with the blood. Therefore, injectable platelet-rich fibrin (i-PRF), which is a blood concentrate system derived from centrifuged human peripheral blood, was chosen for this examination. I-PRF can be considered a cell suspension containing cells that are involved in wound healing, such as platelets and leukocytes [29]. In this context, the pattern of interaction with i-PRF might provide several hints concerning the initial cellular interactions with the biomaterial. The results of the ex vivo part showed that OS was occlusive to the cells and fibrin of the i-PRF and prevented cellular penetration into the membrane body. These results underline the impenetrability of OS to soluble plasma and proteins, such as the fluid fibrin.

The in vivo study focused on the barrier capacity of OS over 30 days and the induced cells in comparison to the cells involved in wound healing of the control group. In vivo histological analysis revealed no cellular penetration of the membrane at any time point. In short, both ex vivo human cells and in vivo murine inflammatory cells were not detected within the membrane. This comparison between the ex vivo and in vivo studies is noteworthy, as it was demonstrated in this study that it is possible to determine the barrier capacity and to obtain clues regarding the cellular response of biomaterials by using a human-derived cell-rich blood concentrate, i-PRF, to reach results similar to those obtained by in vivo animal experiments. However, further applications of this method are necessary to evaluate the potential of i-PRF to serve as an

alternative to in vivo animal experimentation to assess immediate and early tissue reactions towards biomaterials.

Histological analysis of the cellular reaction showed that the membrane induced an initial mononuclear cell-based reaction at day 3. At this time point, a large number of CD-68-positive cells, macrophages, were detected within the implantation bed. Thus, at the mid-term evaluation time point, day 15, a course change in the inflammatory pattern was observed. During this time, the number of CD-68-positive cells significantly decreased, coincident with the appearance of multinucleated giant cells (MNGCs). The trend of the CD-68 accumulation was similar to the control group wound healing. However, OS induced significantly higher numbers of CD-68 cells at all time points. In addition, no MNGCs were found in the control group at any time point. This significant reduction in the number of CD-68 cells towards days 15 and 30 in the OS group might be related to the physiological presence of macrophages in an increased number during the initial phase of the wound healing and their physiological persistence period within the wounded site, as was the case in the control group [10]. However, the high number of CD-68-positive cells within the OS group in comparison to the control group showed a higher rate of inflammation due to the biomaterial, which might have led to the persistence of a specific type of macrophages that is not only involved in wound healing but also in so-called "frustrated phagocytosis" [30, 31], a process of foreign body giant cell formation in which macrophages fuse to form MNGCs after their efforts to phagocytize the implanted biomaterial proved futile. From day 15 to day 30, the number of CD-68-positive cells showed no significant difference, but the number of MNGCs significantly increased. It might be deduced that newly recruited macrophages progressively fused to form MNGCs as the collagen biomaterial continued to persist in the implantation region. In this context, the observed cellular response also might be partly due to the surface topography of OS, as the surface properties of biomaterials influence the type of proteins that adhere to the biomaterial surfaces [13]. This impacts the adhesion and subsequent polarization of macrophages downstream, the amount and types of cytokines they secrete, and, eventually the fusion of these macrophages into MNGCs [32, 33].

The material-adherent MNGCs were mostly TRAP-negative. Only single TRAP-positive MNGCs were located within the implantation region, and their numbers displayed no statistically significant increase over the study period. The presence of MNGCs within the implantation bed indicated a foreign body reaction towards the evaluated membrane [31], although the role of biomaterial-related MNGCs is still mostly unexplored.

The aforementioned significant increase in the total number of MNGCs between day 3, day 15, and day 30 also contributed to a significant rise in implantation bed vascularization between the analyzed time points. The MNGCs might have
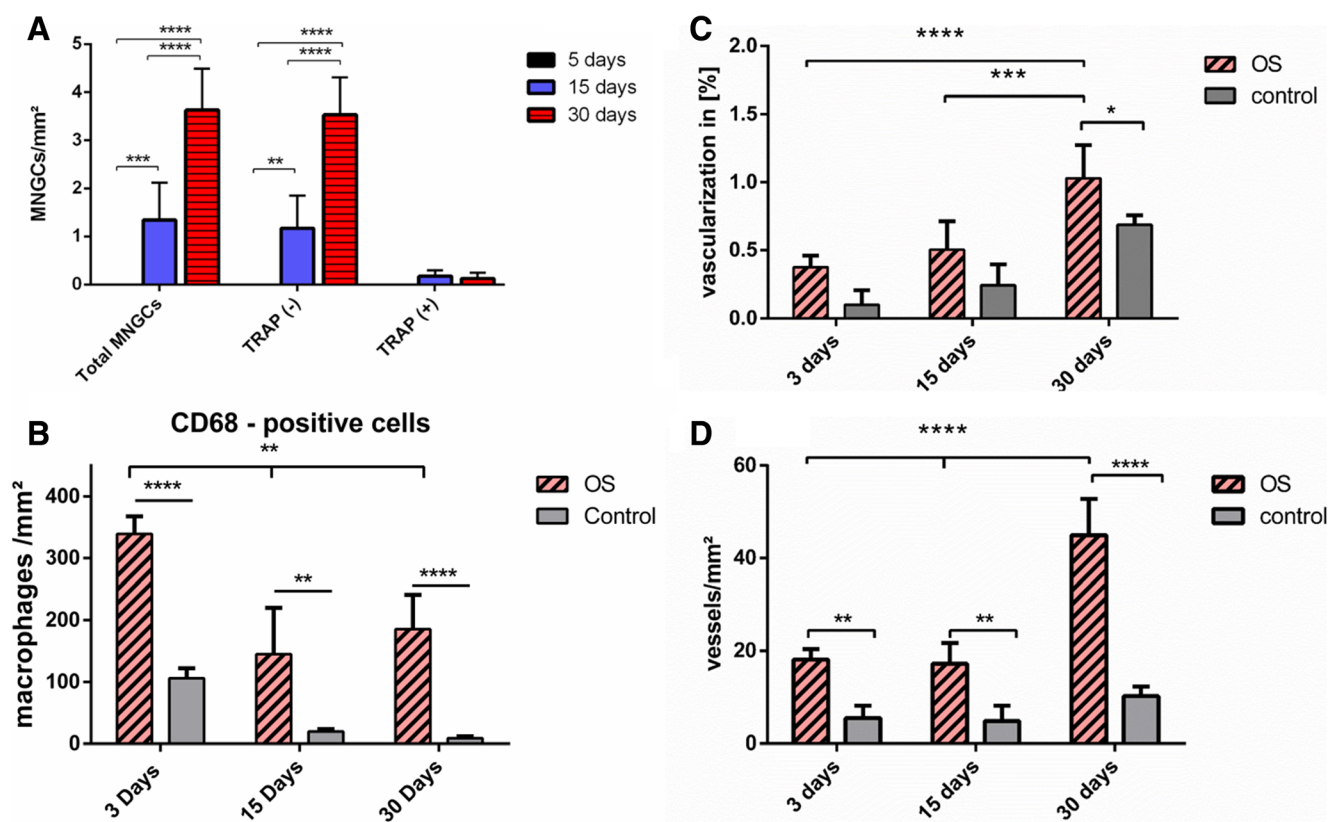
Fig. 7 Comparative graphical presentation of the histomorphometric statistical analysis over the study period. Values are illustrated as means and SD. **a** The number of total multinucleated giant cells (MNGCs) and TRAP-positive and TRAP-negative MGCSs per square millimeter. **b** The total number of macrophages (CD-68-positive cells) per square millimeter. **c** The vascularization rate over the study time in the OS test group and the control group. The vessel area was calculated as a percentage of the total examined area. **d** The number of vessels per square millimeter in the OS test group and the control group. $* = P < 0.05$, $** = P < 0.1$, $*** = P < 0.01$, and $**** = P < 0.001$

contributed to the increase in implantation bed vascularization, since it is known that MNGCs secrete vascular endothelial growth factor, a main protagonist of neoangiogenesis [12, 34]. These findings verify the present results, which highlight the correlation between the enhanced vascularization and the increase in the number of MNGCs within the implantation bed of collagen-based biomaterials. Taken together, the significant increase in the number of MNGCs and the significant rise in implantation bed vascularization over the course of the study are indicative of a foreign body reaction.

Interestingly, recent studies have shown that the presence of MNGCs within the implantation bed of the non-cross-linked collagen membrane led to its disintegration by premature connective tissue ingrowth and eventual membrane breakdown. In these studies, the correlation between the increased number of MNGCs and the enhanced implantation bed vascularization bears resemblance to our current findings [13, 35]. Although MNGCs boast enhanced oxidative and phagocytic capabilities compared to macrophages alone [36, 37], the significant increase in the vascularization and number of MNGCs in the present study did not alter the integrity of OS over 30 days. In contrast, the membrane remained fully intact, without exhibiting any signs of cellular penetration,

degradation, or membrane breakdown over the observation period of 30 days. Moreover, as OS is derived from porcine tendons, it is different from the other membranes investigated earlier by our study group, which are either processed from the porcine dermis and/or pericardium [13–15]. In this context, the quality and the harvesting compartment of the used collagen might play a crucial role in its degradation pattern and therefore its barrier function.

Other studies conducted by our group have shown that several biomaterials induce a full physiological reaction without the formation of MNGCs, such as a non-cross-linked gamma-sterilized collagen membrane that maintained its structure over a period of 60 days. It underwent a slow and controlled integration by inducing a mere mononuclear reaction that was similar to the wound healing physiological reaction that was observed in the control group of the present study. Moreover, these mononuclear cells were accompanied by a mild vascularization. This membrane elicited a physiological mononuclear reaction and mild vascularization pattern. The integration of the membrane was achieved by allowing the host cells to slowly migrate into the membrane scaffold while preserving the function, structure, and the functional barrier of the membrane [13].

Despite the formation of MNGCs, in an in vivo study in a dog model, OS was used to cover critical size defects within the jaw after tooth extraction. After 25 weeks, OS showed signs of ossification and led to enhanced bone regeneration compared to sham OP [38]. The manufacturing technique of OS also makes it highly interesting, as the collagen fibrils are reconstituted de novo from extracted monomeric collagen, whereas conventional membranes are assembled from residual in situ collagen after the removal of all immunogenic components from the donor tissue. Another distinct characteristic of OS is the incorporation of ribose to cross-link the collagen fibrils by a patented glycation process, GLYMATRIX™ [21]. In a way, OS simulates glycation by glucose, a well-documented occurrence in aging tissue and diabetes, which grants collagen fibers resistance to degradation by collagenase [39, 40].

In comparison, other cross-linking methods, such as chemical cross-linking with glutaraldehyde, evoked a more aggressive inflammatory reaction [41]. In addition, clinical human studies have shown that even when exposed to the oral environment, OS sustained GBR and GTR functions compared [18, 42]. Additionally, a case series in which OS was applied for GBR in implant-related bony defects showed that 25–29 weeks after primary healing, new bone formation was observed in close proximity to the OS showing partial signs of ossification [43].

The actual results in OS resemble the cellular reaction observed with e-PTFE, a non-resorbable membrane that displayed a similar inflammatory pattern and cellular reaction to the currently evaluated membrane OS. In brief, e-PTFE elicited an initial mononuclear cell-based reaction, which was followed by the formation of MNGCs. e-PTFE, which served as a bona fide physical barrier, prevented cellular infiltration for an investigation period of 60 days. Accordingly, the e-PTFE membrane was encapsulated within a vessel- and MNGC-rich connective tissue after 60 days [7]. No encapsulation could be detected at the latest time point of this study. Nevertheless, the limited evaluation period of 30 days is likely insufficient to evaluate whether the membrane will ultimately undergo encapsulation. Therefore, further long-term studies are needed to assess to what extent the presence of MNGCs within the implantation bed of this specific cross-linked biomaterial might influence the regeneration process, which is thought to be guided by OS.

Additionally, one limitation of the in vivo part of this study is analyzing only sugar-based without PRF. Thereby, this study cannot make any statement about the in vivo cellular reaction to OS-i-PRF combination. The implantation of i-PRF in small animals would require the use of severe combined immunodeficiency (SCID) mice to avoid any immune reaction to the implanted human cells. Ongoing research is towards understanding the in vivo cellular reaction to PRF and its combination with different biomaterials. This application might be a tool to modulate the cellular reaction towards biomaterials by means of pre-loading with i-PRF in advance.

Conclusion

The present study evaluated, the permeability and barrier capacity of a ribose cross-linked collagen membrane ex vivo as well as in vivo, with specific respect to the induced cell types. Ex vivo, the membrane was impermeable to human cells derived from peripheral blood. In vivo, the membrane showed a stable structure and allowed no cellular penetration over 30 days. The in vivo cellular reaction was initiated by mononuclear cells, which progressed to the formation of multinucleated giant cells (MNGCs) from day 15 onwards. Over the course of the experiment, a significant increase in the number of MNGCs was associated with a significant rise in implantation bed vascularization. This is indicative of a foreign body reaction. However, no breakdown was observed at any time point. The data gathered prove that ribose cross linking enhanced the barrier functionality of the collagen membranes. On these grounds, further long-term studies are necessary to investigate the degradation pattern of this specific cross-linked biomaterial.

Compliance with ethical standards

Conflict of interest   The authors declare that they have no conflict of interests.

Ethical approval   All applicable international, national, and/or institutional guidelines for the care and use of animals were followed.

Informed consent   For the ex vivo part, informed consent was obtained from all individual participants included in the study.

References

1.   Bottino MC, Thomas V, Schmidt G, Vohra YK, Chu T-MG, Kowolik MJ, Janowski GM (2012) Recent advances in the development of GTR/GBR membranes for periodontal regeneration—a materials perspective. Dent Mater 28(7):703–721. https://doi.org/10.1016/j.dental.2012.04.022

2.   Cen L, Liu W, Cui L, Zhang W, Cao Y (2008) Collagen tissue engineering: development of novel biomaterials and applications. Pediatr Res 63(5):492–496. https://doi.org/10.1203/PDR.0b013e31816c5bc3

3.   Dahlin C, Linde A, Gottlow J, Nyman S (1988) Healing of bone defects by guided tissue regeneration. Plast Reconstr Surg 81(5):672–676. https://doi.org/10.1097/00006534-198805000-00004

4.   Patino MG, Neiders ME, Andreana S, Noble B, Cohen RE (2002) Collagen as an implantable material in medicine and dentistry. Research 220

5. Wang H-L, Boyapati L (2006) "PASS" principles for predictable bone regeneration. Implant Dent 15:8–17. https://doi.org/10.1097/01.id.0000204762.39826.0f

6. Buser D, Dula K, Hirt HP, Schenk RK (1996) Lateral ridge augmentation using autografts and barrier membranes: a clinical study with 40 partially edentulous patients. J Oral Maxillofac Surg 54:420–432 3

7. Ghanaati S (2012) Non-cross-linked porcine-based collagen I-III membranes do not require high vascularization rates for their integration within the implantation bed: a paradigm shift. Acta Biomater 8(8):3061–3072. https://doi.org/10.1016/j.actbio.2012.04.041

8. Sheikh Z, Qureshi J, Alshahrani AM, Nassar H, Ikeda Y, Glogauer M, Ganss B (2016) Collagen based barrier membranes for periodontal guided bone regeneration applications. Odontology. https://doi.org/10.1007/s10266-016-0267-0

9. Bunyaratavej P, Wang HL (2001) Collagen membranes: a review. J Periodontol 72(2):215–229. https://doi.org/10.1902/jop.2001.72.2.215

10. Gurtner G, Werner S, Barrandon Y, Longaker M (2008) Wound repair and regeneration. Nature 453(7193):314–321. https://doi.org/10.1038/nature07039

11. Shevach EM, Rosenthal AS (1973) Function of macrophages in antigen recognition by guinea pig T lymphocytes. II. Role of the macrophage in the regulation of genetic control of the immune response. J Exp Med 138:1213–1229 http://www.ncbi.nlm.nih.gov/pubmed/4126770. Accessed 20 March 2017

12. Moens S, Goveia J, Stapor PC, Cantelmo AR, Carmeliet P (2014) The multifaceted activity of VEGF in angiogenesis—implications for therapy responses. Cytokine Growth Factor Rev 25(4):473–482. https://doi.org/10.1016/j.cytogfr.2014.07.009

13. Ghanaati S, Schlee M, Webber MJ, Willershausen I, Barbeck M, Balic E, Görlach C, Stupp SI, Sader RA, Kirkpatrick CJ, Ghanaati S (2011) Evaluation of the tissue reaction to a new bilayered collagen matrix in vivo and its translation to the clinic. Biomed Mater 6(1):15010–15012. https://doi.org/10.1088/1748-6041/6/1/015010

14. Barbeck M, Lorenz J, Kubesch A, Böhm N, Booms P, Choukroun J, Sader R, Kirkpatrick CJ, Ghanaati S (2015) Porcine dermis-derived collagen membranes induce implantation bed vascularization via multinucleated giant cells: a physiological reaction? J Oral Implantol 41(6):e238–e251. https://doi.org/10.1563/aaid-joi-D-14-00274

15. Barbeck M, Lorenz J, Holthaus MG, Raetscho N, Kubesch A, Booms P, Sader R, Kirkpatrick CJ, Ghanaati S (2015) Porcine dermis and pericardium-based, non-cross-linked materials induce multinucleated giant cells after their in vivo implantation: a physiological reaction? J. Oral Implantol. 41(6):e267–e281. https://doi.org/10.1563/aaid-joi-D-14-00155

16. Brunel G, Piantoni P, Elharar F, Benqué E, Marin P, Zahedi S (1996) Regeneration of rat calvarial defects using a bioabsorbable membrane technique: influence of collagen cross-linking. J Periodontol 67(12):1342–1348. https://doi.org/10.1902/jop.1996.67.12.1342

17. Friedmann A, Strietzel FP, Maretzki B, Pitaru S, Bernimoulin J-P (2002) Histological assessment of augmented jaw bone utilizing a new collagen barrier membrane compared to a standard barrier membrane to protect a granular bone substitute material. Clin Oral Implants Res 13(6):587–594. https://doi.org/10.1034/j.1600-0501.2002.130603.x

18. Moses O, Pitaru S, Artzi Z, Nemcovsky CE (2005) Healing of dehiscence-type defects in implants placed together with different barrier membranes: a comparative clinical study. Clin Oral Implants Res 16(2):210–219. https://doi.org/10.1111/j.1600-0501.2004.01100.x

19. Friedmann A, Gissel K, Soudan M, Kleber B-M, Pitaru S, Dietrich T (2011) Randomized controlled trial on lateral augmentation using two collagen membranes: morphometric results on mineralized tissue compound. J Clin Periodontol 38(7):677–685. https://doi.org/10.1111/j.1600-051X.2011.01738.x

20. Rothamel D, Schwarz F, Sager M, Herten M, Sculean A, Becker J (2005) Biodegradation of differently cross-linked collagen membranes: an experimental study in the rat. Clin Oral Implants Res 16(3):369–378. https://doi.org/10.1111/j.1600-0501.2005.01108.x

21. OSSIX PLUS—GLYMATRIX™ Technology in Brief, (n.d.)

22. OSSIX ® PLUS Instructions for Use IFU-MKT-OSP-016 ver OSSIX ® PLUS The Resorbable Collagen Membrane Instructions for Use for OSSIX ® PLUS, (2016)

23. Ghanaati S, Booms P, Orlowska A, Kubesch A, Lorenz J, Rutkowski J, Landes C, Sader R, Kirkpatrick C, Choukroun J (2014) Advanced platelet-rich fibrin: a new concept for cell-based tissue engineering by means of inflammatory cells. J Oral Implantol 40(6):679–689. https://doi.org/10.1563/aaid-joi-D-14-00138

24. Choukroun J, Ghanaati S (2017) Reduction of relative centrifugation force within injectable platelet-rich-fibrin (PRF) concentrates advances patients' own inflammatory cells, platelets and growth factors: the first introduction to the low speed centrifugation concept. Eur J Trauma Emerg Surg. https://doi.org/10.1007/s00068-017-0767-9

25. Miron RJ, Fujioka-Kobayashi M, Hernandez M, Kandalam U, Zhang Y, Ghanaati S, Choukroun J (2017) Injectable platelet rich fibrin (i-PRF): opportunities in regenerative dentistry? Clin Oral Investig. https://doi.org/10.1007/s00784-017-2063-9

26. Ghanaati S, Kirkpatrick C, Kubesch A, Lorenz J, Sader R, Udeabor S, Barbeck M, Choukroun J (2014) Induction of multinucleated giant cells in response to small sized bovine bone substitute (Bio-Oss TM) results in an enhanced early implantation bed vascularization. Ann Maxillofac Surg 4:150. https://doi.org/10.4103/2231–0746.147106

27. Ghanaati S, Orth C, Unger RE, Barbeck M, Webber MJ, Motta A, Migliaresi C, James Kirkpatrick C (2010) Fine-tuning scaffolds for tissue regeneration: effects of formic acid processing on tissue reaction to silk fibroin. J Tissue Eng Regen Med 4:464–472. https://doi.org/10.1002/term.257

28. Serrano C, García-Fernández L, Fernández-Blázquez JP, Barbeck M, Ghanaati S, Unger R, Kirkpatrick J, Arzt E, Funk L, Turón P, del Campo A (2015) Nanostructured medical sutures with antibacterial properties. Biomaterials 52:291–300. https://doi.org/10.1016/j.biomaterials.2015.02.039

29. Choukroun J, Ghanaati S (2016) Reduction of relative centrifugation force within injectable PRF—(platelet-rich-fibrin) concentrates advances patients' own inflammatory cells, platelets and growth factors: first introduction of the low speed centrifugation concept (LSCC), Eur J Trauma Emerg Surg. accepted

30. MacLauchlan S, Skokos EA, Meznarich N, Zhu DH, Raoof S, Shipley JM, Senior RM, Bornstein P, Kyriakides TR (2009) Macrophage fusion, giant cell formation, and the foreign body response require matrix metalloproteinase 9. J Leukoc Biol 85(4):617–626. https://doi.org/10.1189/jlb.1008588

31. Anderson JM, Rodriguez A, Chang DT (2008) Foreign body reaction to biomaterials. Semin Immunol 20(2):86–100. https://doi.org/10.1016/j.smim.2007.11.004

32. McNally AK, Anderson JM (2011) Macrophage fusion and multinucleated giant cells of inflammation. Adv Exp Med Biol 713:97–111. https://doi.org/10.1007/978-94-007-0763-4_7

33. McNally AK, Anderson JM (2003) Foreign body-type multinucleated giant cell formation is potently induced by alpha-tocopherol and prevented by the diacylglycerol kinase inhibitor R59022. Am J Pathol 163(3):1147–1156. http://www.ncbi.nlm.nih.gov/pubmed/12937156. Accessed 27 Jan 2017. https://doi.org/10.1016/S0002-9440(10)63474-8

34. Ghanaati S, Barbeck M, Orth C, Willershausen I, Thimm BW, Hoffmann C, Rasic A, Sader RA, Unger RE, Peters F, Kirkpatrick

CJ (2010) Influence of β-tricalcium phosphate granule size and morphology on tissue reaction in vivo. Acta Biomater 6(12): 4476–4487. https://doi.org/10.1016/j.actbio.2010.07.006

35. Lorenz J, Kubesch A, Korzinskas T, Barbeck M, Landes C, Sader RA, Kirkpatrick CJ, Ghanaati S (2015) TRAP-positive multinucleated giant cells are foreign body giant cells rather than osteoclasts: results from a split-mouth study in humans. J Oral Implantol 41(6): e257–e266. https://doi.org/10.1563/AAID-JOI-D-14-00273

36. McNally AK, Anderson JM (2005) Multinucleated giant cell formation exhibits features of phagocytosis with participation of the endoplasmic reticulum. Exp Mol Pathol 79(2):126–135. https://doi.org/10.1016/j.yexmp.2005.06.008

37. Enelow RI, Sullivan GW, Carper HT, Mandell GL (1992) Cytokine-induced human multinucleated giant cells have enhanced candidacidal activity and oxidative capacity compared with macrophages. J Infect Dis 166(3):664–668. https://doi.org/10.1093/infdis/166.3.664

38. Zubery Y, Goldlust A, Alves A, Nir E (2007) Ossification of a novel cross-linked porcine collagen barrier in guided bone regeneration in dogs. J Periodontol 78(1):112–121. https://doi.org/10.1902/jop.2007.060055

39. Gautieri A, Redaelli A, Buehler MJ, Vesentini S (2014) Age- and diabetes-related nonenzymatic crosslinks in collagen fibrils: candidate amino acids involved in advanced glycation end-products. Matrix Biol 34:89–95. https://doi.org/10.1016/j.matbio.2013.09.004

40. Bourne JW, Lippell JM, Torzilli PA (2014) Glycation cross-linking induced mechanical-enzymatic cleavage of microscale tendon fibers. Matrix Biol 34:179–184. https://doi.org/10.1016/j.matbio.2013.11.005

41. Rothamel D, Schwarz F, Sculean A, Herten M, Scherbaum W, Becker J (2004) Biocompatibility of various collagen membranes in cultures of human PDL fibroblasts and human osteoblast-like cells. Clin Oral Implants Res 15(4):443–449. https://doi.org/10.1111/j.1600-0501.2004.01039.x

42. Klinger A, Asad R, Shapira L, Zubery Y (2010) In vivo degradation of collagen barrier membranes exposed to the oral cavity. Clin Oral Implants Res 21(8):873–876. https://doi.org/10.1111/j.1600-0501.2010.01921.x

43. Zubery Y, Nir E, Goldlust A (2008) Ossification of a collagen membrane cross-linked by sugar: a human case series. J Periodontol 79(6):1101–1107. https://doi.org/10.1902/jop.2008.070421

Annex IV

Original article published as collaborative project in the scope of ITN-SNAL:

Wend, S., Kubesch, A., Orlowska, A., Al-Maawi, S., Zender, N., **Dias, A.**, Miron, R. J., Sader, R., Booms, P., Kirkpatrick, C. J., Choukroun, J., Ghanaati, S. (2017) Reduction of the relative centrifugal force influences cell number and growth factor release within injectable PRF-based matrices. J Mater Sci Mater Med. 28, 12, 188;

Annex IV

CLINICAL APPLICATIONS OF BIOMATERIALS

Original Research

Reduction of the relative centrifugal force influences cell number and growth factor release within injectable PRF-based matrices

Simon Wend[1] · Alica Kubesch[1] · Anna Orlowska[1] · Sarah Al-Maawi[1] ·
Niklas Zender[1] · Andre Dias[1] · Richard J. Miron[2] · Robert Sader[1] · Patrick Booms[1] ·
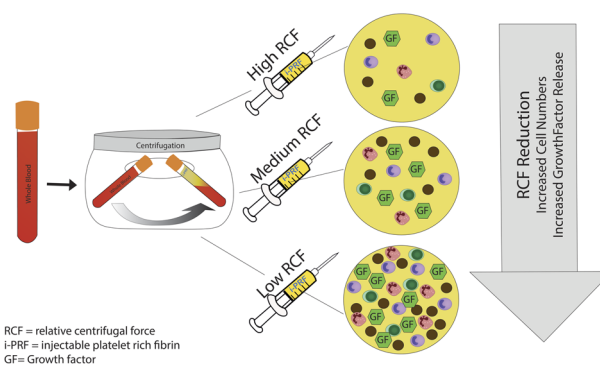C. James Kirkpatrick[1] · Joseph Choukroun[1,3] · Shahram Ghanaati[1]

Abstract Platelet rich fibrin (PRF) is a blood concentrate system obtained by centrifugation of peripheral blood. First PRF matrices exhibited solid fibrin scaffold, more recently liquid PRF-based matrix was developed by reducing the relative centrifugation force and time. The aim of this study was to systematically evaluate the influence of RCF (relative centrifugal force) on cell types and growth factor release within injectable PRF- in the range of 60–966 g using consistent centrifugation time. Numbers of cells was analyzed using automated cell counting (platelets, leukocytes, neutrophils, lymphocytes and monocytes) and histomorphometrically (CD 61, CD- 45, CD-15+, CD-68+, CD-3+ and CD-20). ELISA was utilized to quantify the concentration of growth factors and cytokines including PDGF-BB, TGF-β1, EGF, VEGF and MMP-9. Leukocytes, neutrophils, monocytes and lymphocytes had significantly higher total cell numbers using lower RCF. Whereas, platelets in the low and medium RCF ranges both demonstrated significantly higher values when compared to the high RCF group. Histomorphometrical analysis showed a significantly high number of CD61+, CD-45+ and CD-15+ cells in the low RCF group whereas CD-68+, CD-3+ and CD-20+ demonstrated no statistically significant differences between all groups. Total growth factor release of PDGF-BB, TGF-β1 and EGF had similar values using low and medium RCF, which were both significantly higher than those in the high RCF group. VEGF and MMP-9 were significantly higher in the low RCF group compared to high RCF. These findings support the LSCC (low speed centrifugation concept), which confirms that improved PRF-based matrices may be generated through RCF reduction. The enhanced regenerative potential of PRF-based matrices makes them a potential source to serve as a natural drug delivery system. However, further pre-clinical and clinical studies are required to evaluate the regeneration capacity of this system.

Graphical abstract

Reduction of the relative centrifugal force influences cell number and growth factor release within injectable PRF-based matrices

RCF = relative centrifugal force
i-PRF = injectable platelet rich fibrin
GF= Growth factor

1 Introduction

Platelet rich fibrin (PRF) is a blood concentrate system obtained from the peripheral blood of patients. first protocol

✉ Shahram Ghanaati
shahram.ghanaati@kgu.de

[1] Department for Oral, Cranio-Maxillofacial and Facial Plastic Surgery, FORM (Frankfurt Orofacial Regenerative Medicine) Lab, University Hospital Frankfurt Goethe University, Frankfurt am Main, Theodor-Stern-Kai 7, 60590 Frankfurt am Main, Germany

[2] Department of Periodontology, College of Dental Medicine, Nova Southeastern University, Fort Lauderdale, Florida, USA

[3] Pain Therapy Center, Nice, France

⚡ Springer

of PRF matrices are generated using a one-step centrifugation process without necessitating the use of anticoagulants, known inhibitors of wound healing [1, 2]. Since the introduction of PRF in 2001 as a first platelet concentrate without added anticoagulants[1], the successful applications of PRF in dentistry and medicine has seen a steady and widespread increase in popularity with many clinical indications demonstrating improvements in regenerative outcomes [3]. The composition of the PRF matrix contains various inflammatory cells and growth factors embedded in a specifically structured fibrin network [2]. Platelets act as the primary hemostasis cells shown to release a series of platelet-derived growth factors to recruit inflammatory cells to the impaired region and support tissue regeneration following the physiological phases of wound healing [4]. Additionally, the interaction of platelets with leukocytes, which are also included within PRF-based matrices, further contribute to wound healing [5], and the fibrin network provides a scaffold for inflammatory cells as well as binding sites for growth factors [6, 7].

While PRF has seen tremendous momentum as a regenerative modality in dentistry and medicine, the manufacturing process of the first described PRF scaffolds required a high relative centrifugal force (RCF). This resulted in a fibrin clot with a dense structure, including platelets and leukocytes that were mostly distributed unevenly throughout the scaffold accumulated at the proximal portion of the PRF clot adjacent to the isolated red cell fraction [2]. In order to improve the structure of PRF and enhance their regenerative potential, our group recently demonstrated that by reducing the RCF and modifying the centrifugation time in solid PRF-based matrices, a more porous fibrin structure could be manufactured with more leukocytes and growth factor release when compared to originally designed PRF scaffolds fabricated using high RCF [2, 8, 9].

In addition to solid fibrin clots [2], a clinical need exists to develop an injectable PRF-based matrix for various clinical procedures including direct injections as well as to combine with various biomaterials to improve their angiogenic potential. Previous findings from research conducted by our group with solid PRF-based matrices revealed that the RCF and the centrifugation time were crucial factors for modifying the structure and composition of PRF-based matrices [2, 8]. Moreover, solid physiological clot formation is supported by the glass surface of the collecting tubes used to generate solid PRF matrices. Therefore, the manufacturing of an injectable blood concentrate without the need for anticoagulants was achieved by developing specific plastic tubes favoring the liquid phase after centrifugation. Recently, our group conducted a study to assess the influence of the applied RCF on leukocyte and platelet numbers within three different PRF-based matrices (i-PRF)

with decreasing RCF content. The findings from that study showed that reducing RCF led to a significant enrichment in the i-PRF PRF scaffolds with greater leukocytes, platelets, and growth factor release after 8 min centrifugation time [10]. Based on these results, the low speed centrifugation concept (LSCC) was introduced as a potential tool to modify PRF scaffolds by fine tuning the centrifugation settings [10].

Currently, the clinically-utilized liquid injectable PRF formulation (i-PRF) has been described using a 3 min centrifugation period in order to produce a liquid platelet concentrate containing primarily liquid fibrinogen and thrombin prior to fibrin formation. The aim of the present study was to further analyze the influence of RCF reduction on i-PRF matrices using various centrifugation speeds. Systematic analysis included a wide RCF range (966-60 g-force) and a stepwise decrease of the RCF by halving the revolutions per minute (rpm) from 2800 rpm to 1400 rpm to 700 rpm. Thereby, we questioned whether the so-called LSCC effect would systematically alter these newer centrifugation times, i.e., 3 min. In the present study, the centrifugation time of 3 min was maintained in the three test groups to focus solely on the influence of the RCF. Thus, the goal of this study was a comparative analysis of three different injectable PRF-based matrices generated by systematic decreases in RCF by 4 times and 16 times while maintaining the centrifugation time. The focus was placed on the regenerative properties of the matrices, including the total number and distribution pattern of platelets and leukocytes, including their sub-families along with the release of several growth factors and cytokines within the i-PRF matrices.

2 Materials and Methods

2.1 Injectable platelet-rich fibrin (i-PRF) preparation

Blood was drawn from three healthy volunteers in an age range between 20–60 years without anticoagulant ingestion. The donors provided informed consent for their participation in this study. Injectable PRF matrices were prepared, as previously described [10]. Briefly,10 ml of peripheral blood was collected in sterile plain plastic tubes (i-PRF, Process for PRF, Nice, France) and immediately centrifuged (Duo Centrifuge, PROCESS for PRF, Nice, France). Systematic decreases in RCF were performed in steps as follows:

- High RCF: 10 ml; 2800 rotations per minute (rpm); for 3 min; 966 g.
- Medium RCF: 10 ml; 1400 rotations per minute (rpm); for 3 min; 241 g.
- Low RCF: 10 ml; 700 rotations per minute (rpm); 3 min; 60 g.

After centrifugation, injectable PRF was collected using an ordinary syringe (5 ml Terumo® Syringe, Leuven, Belgium) with a needle (20 G x ½", Terumo®, Leuven, Belgium) through means of aspirating the upper yellowish layer without manipulating the red blood cell fraction.

2.2 PRF-matrices cultivation

The prepared injectable PRF matrices (500 µl per well) were filled in 24-well cell culture plates (CELLSTAR®, Greiner bio-one) and incubated at 37 degrees for one hour until total clotting. Afterwards, 500 µl Dulbecco's Modified Eagle Medium (Biochrom GmbH, Berlin, Germany) was added per well and further incubated at 37 degrees for one hour. Subsequently, the supernatants were collected and frozen at $-80\,°C$ for growth factor and cytokine analysis.

2.3 Enzyme-linked immunosorbent assay (ELISA)

The protein concentrations of vascular epithelial growth factor (VEGF), transforming growth factor (TGF-β1), platelet-derived growth factor (PDGF BB), matrix metallopeptidase 9 (MMP9) and epidermal growth factor (EGF) were quantified using ELISA-kits (Quantikine® ELISA, R&D Systems, Minneapolis, USA) according to the manufacturer's instructions, as follows (Table 1). The optical density was determined using a microplate reader (Infinite® M200, Tecan, Grödig, Austria) set at 450 nanometers. Next, the final concentrations of each sample were calculated using the graphing and statistics software GraphPad Prism 6 (GraphPad Software, Inc., La Jolla, USA). The experiments were performed in triplicate for each blood donor and preparation protocol.

2.4 Automated cell-counting

Automated cell-counting was performed as described before [10]. For each specific experimental condition, the injectable matrices of the three groups were treated with EDTA (BD, New Jersey) for anticoagulation. This intervention was unavoidable for automated cell counting measurements. Subsequently, ADVIA® LabCell® Automation Solution (Siemens, France) analysis was performed at a medical laboratory (Labazur laboratory, Nice, France). The focus of the analyses was detecting the number of leukocytes, neutrophil granulocytes, monocytes, lymphocytes and platelets per microliter in each group.

2.5 Tissue processing and histological preparation

The clotted i-PRF matrices were fixed in 4% formaldehyde solution for 24 h and processed in various solutions as

Table 1 The used ELISA and detection ranges for the different growth factors

Growth factor/cytokine	Catalogue number	Detection range
VEGF	DVE00	15.6–1000 pg/mL
TGF-β1	DB100B	31.2–2000 pg/mL
PDGF BB	DBB00	31.2–2000 pg/mL
EGF	DEG00	3.9–250 pg/mL
MMP 9	DMP900	0.3–20 ng/mL

previously described [2, 11, 12]. Briefly, a dehydration through an alcohol series with various concentrations was performed. Then, the samples were treated with xylene and embedded in paraffin. Three samples per donor and group were cut using a rotary microtome (Leica RM 2255, Wetzlar, Germany) to obtain 6 slices of 2–3 µm thickness. Subsequently, the sections were deparaffinized using xylene and rehydrated by passing through a series of alcohol with decreasing concentrations. One section per donor and group was stained in H.E. for an overview analysis of the structure and cells. Six sections were used for specific immunohistochemistry.

Platelets (CD61), leukocytes (CD 45), T-lymphocytes (CD3), B-lymphocytes (CD20), neutrophil granulocytes (CD15) and monocytes (CD68). Standardized immunohistochemical staining was performed according to standardized methods as previously described [2, 13, 14]. In brief, the deparaffinized and rehydrated sections were placed on slides and treated with citrate buffer (pH 6) at 96 °C for 20 min. Then, the slides were washed and cooled under running trap water. Before transferring the slides to the autostainer (Lab Vision™ Autostainer 360, ThermoScientific), the samples were washed with TBS. Next, the autostainer was loaded with a suitable solution and antibody for each specific cell type (Table 2) according the manufacturer's instruction. Additionally, and UltraVision™ Quanto Detections System HRP AEC was used. After autostaining, the slides were counterstained with hemalum for 30 s and washed with water. Finally covered with Aquatex® (Merck Millipore, Darmstadt, Germany).

2.6 Histological evaluation

Three of the authors were blinded and evaluated the slides independently. Histological analysis was performed using a light microscope (Nikon Eclipse Ni, Tokyo, Japan). Representative histological images were captured with a Nikon DS-Fi1 digital camera and a Nikon Digital sight unit DS-U3 (Nikon, Tokyo, Japan).

UNIVERSITAT ROVIRA I VIRGILI
STUDY OF RBC SHAPE TRANSITIONS INDUCED BY NANOPARTICLES
André Eduardo Carneiro Dias
188 Page 4 of 11

J Mater Sci: Mater Med (2017)28:188

Table 2 The immunohistochemical markers used in this study and their specifications

Antibody	Targeted cell	Epitope demasking	Concentration
CD 61 (Dako)	Platelets	Citrate-buffer, pH 6.0	1:50
CD 45 (Dako)	Leukocytes	Citrate-buffer, pH 6.0	1:100
CD 3 (Thermo Fisher)	T-lymphocytes	Citrate-buffer, pH 6.0	RTU
CD 20 (Thermo Fisher)	B-lymphocytes	Citrate-buffer, pH 6.0	RTU
CD 15 (Thermo Fisher)	Neutrophil Granulocytes	Tris-EDTA, pH 8.0	RTU
CD 68 (Dako)	Monocytes	Citrate-buffer, pH 6.0	1:200
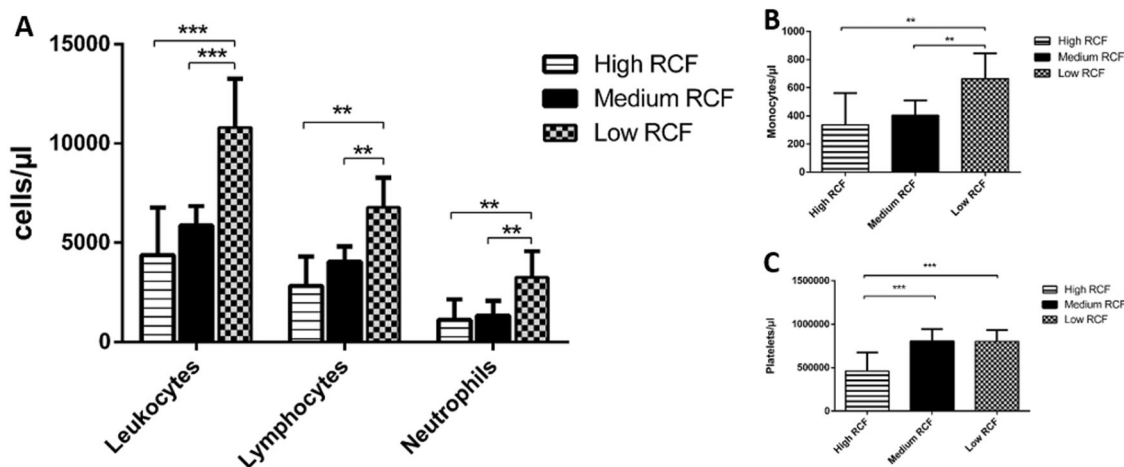
Fig. 1 Comparative diagrams of automated cell counting results. **a** Leukocytes, lymphocytes and neutrophils. **b** Monocytes. **c** Platelets. Statistical analysis showed significant differences at $p < 0.05$ (*) and highly significant differences at $p < 0.01$ (**) and $p < 0.001$ (***)

2.7 Histomorphometrical evaluation

As described before [2], within each group, two immuno-histochemically stained slides for each donor, and cell type were digitalized in a total scan using a Nikon Eclipse 80i microscope in combination with an automatic scanning table (Prior Scientific, Rockland, Maine), which was connected to a Nikon DS-Fi/1 digital camera and a computer with the Nikon NIS − Elements AR software, version 4.0. (Nikon, Tokyo, Japan). The total sample area calculated using the measurement function of NIS-Elements and positive-stained cells were counted manually by a NIS-Elements software counting tool to determine the cell number of each stained cell type per square millimeter.

2.8 Statistical evaluation

Statistical analysis was performed using the graphing and statistics software GraphPad Prism 6 (GraphPad Software, Inc., La Jolla, USA). The measured data are expressed as the mean ± standard deviation (SD). Statistical significance was determined using one-way and two-way analysis of variance (ANOVA) with a Tukey multiple comparisons test ($\alpha = 0.05$). The values were reported as significant at $p < 0.05$ (*) and highly significant at $p < 0.01$ (**) and $p < 0.001$ (***).

3 Results

3.1 Automated cell count

The number of leukocytes and leukocyte subfamilies showed a consistent trend in the examined groups across the cells investigated. In general, a decrease in RCF resulted in an increase in cell numbers. Significantly higher numbers of leukocytes were found in the low RCF group when compared to the high ($p < 0.001$) and medium ($p < 0.001$) RCF groups. No statistically significant differences were observed between the medium and high RCF ranges. Lymphocytes showed a similar trend with significantly higher numbers in the low RCF group when compared to medium RCF ($p < 0.01$) and high RCF groups ($p < 0.01$). Once again, no statistically significant difference was observed between the medium RCF and high RCF groups. The analysis of the total number of neutrophil granulocytes showed significantly higher numbers in the low RCF
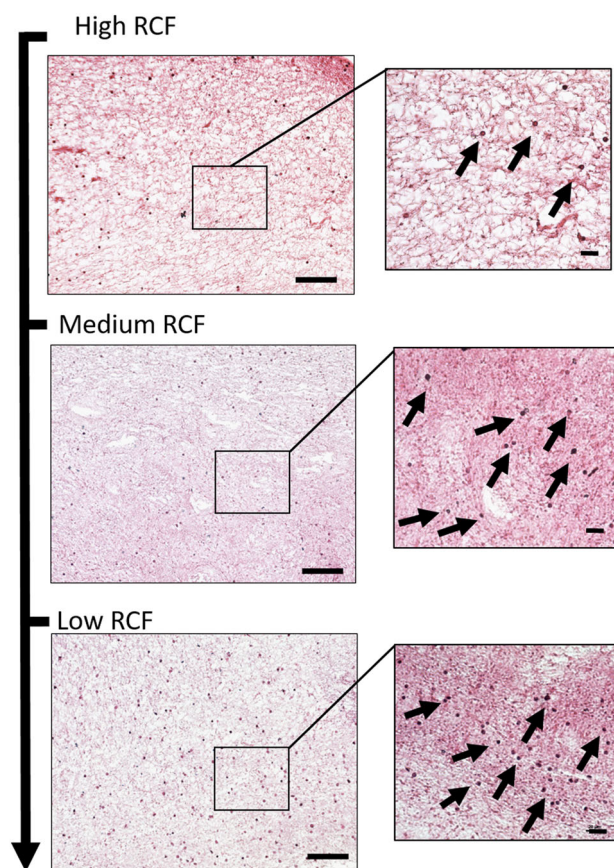
Fig. 2 Representative histological images of the clotted injectable PRF in different RCF ranges (H&E staining; left column × 200 magnification; scale bar = 100 μm; Right column × 600 magnification; scale bar = 20 μm; arrows = cells)

group when compared to the medium ($p < 0.01$) and high ($p < 0.01$) RCF groups, while there was no statistically significant difference between medium RCF and high RCF (Fig. 1a). Similarly, a significantly higher number of monocytes was found in the low RCF group when compared to the medium RCF and high RCF groups ($p < 0.01$) (Fig. 1b). There were also significantly more platelets in both the low RCF and medium RCF groups compared to the high RCF group ($p < 0.001$). No statistically significant differences were detected between the low RCF and medium RCF groups (Fig. 1c).

3.2 Qualitative histological observation

General analysis of the evaluated groups showed that the total number of cells (platelets and leukocytes) was reduced with increased RCF (Fig. 2). The analysis of high RCF group showed a PRF-based matrix consisting mainly of a fibrin network in which single platelets and leukocytes were observable and distributed through the evaluated samples (Fig. 3a1, b1). In the case of medium RCF, more platelets

and leukocytes were found throughout the fibrin scaffold when compared to the high RCF group (Fig. 3a3, b2). Whereas the low RCF group demonstrated a fibrin matrix most evenly and densely populated with platelets and leukocytes compared to the other two tested groups (Fig. 3a3, b3). The findings from these qualitative observations support the findings from the automated cell counting experiments demonstrating that lower RCF resulted in more cells throughout the PRF-based matrices.

### 3.3 Quantitative histomorphometrical analysis

The number of CD-61 positive cells (platelets) was significantly higher in the groups of low and medium RCF ($P < 0.001$ and $P < 0.05$, respectively). Whereas no statistical significant difference was detected between the medium and low RCF groups (Fig. 3c). The histomorphometrical analysis of CD-45 positive cells (leukocytes) showed that a significantly higher number of platelets was found in the low RCF group compared to the medium and high RCF groups ($P < 0.05$). However, no statistical significant difference was found between the medium and high RCF groups (Fig. 3d). The leukocyte subgroup CD-15 positive cells (neutrophil granulocytes) revealed different cell numbers within the three examined injectable PRF matrices. The low RCF group included the highest number of CD-15 cells whereas the medium and high RCF groups showed significantly lower values ($p < 0.001$). No significant difference was observed between the medium and high RCF groups. The analysis of CD-20 positive cells (B-cells) showed comparable values within the three i-PRF matrices. The distribution of CD 68-positive cells (monocytes) within the evaluated matrices showed comparable outcomes between in the low and medium RCF groups, while the high RCF group demonstrated the lowest rate of CD-68-positive cells. Nevertheless, no statistically significant differences were detected between the three groups. Additionally, CD-3 positive cells (T-lymphocytes) were found lowest in the low RCF group whereas medium RCF had the most CD-3 positive cells. Nevertheless, no statistically significant differences were observed (Fig. 4).

3.4 Growth factor and cytokine release

Growth factor release was then quantified by ELISA using the three injectable PRF-matrices at different RCF. The general trend in response to changes in the RCF showed that there was a tendency towards increased growth factor release with lower RCF. PDGF-BB release showed significantly higher values in the low and medium RCF groups when compared to the high RCF group ($p < 0.05$). No statistically significant difference was detected between the low and medium RCF groups. Furthermore, VEGF showed
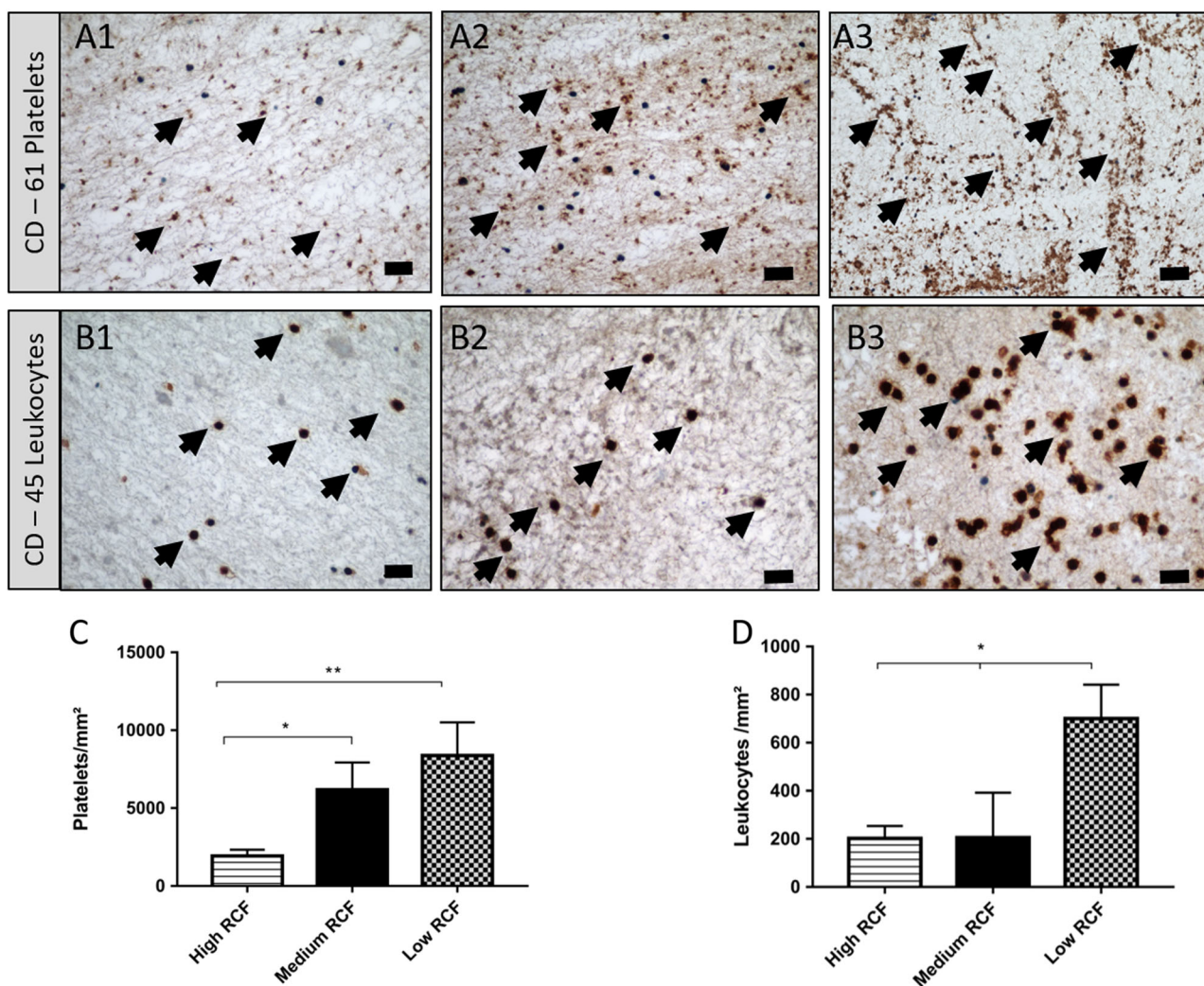
Fig. 3 Histological micrographs of the platelets and leukocytes number in clotted injectable PRF. A1-A3 CD 61 staining, black arrows = CD 61 positive platelets, scale bars = 20 μm. **a1** High RCF range, **a2** medium RCF range **a3** low RCF range. B1-B3 CD 45 staining, black arrows = CD 45 positive leukocytes, scale bars = 20 μm. **b1** High RCF range, **b2** medium RCF range **b3** low RCF range. **c** Statistical analysis of the CD 61-positive evaluated cells. **d** Statistical analysis of the CD 45- positive evaluated cells. Statistical analysis showed significant differences at $p < 0.05$ (*) and highly significant differences at $p < 0.01$ (**) and $p < 0.001$ (***)
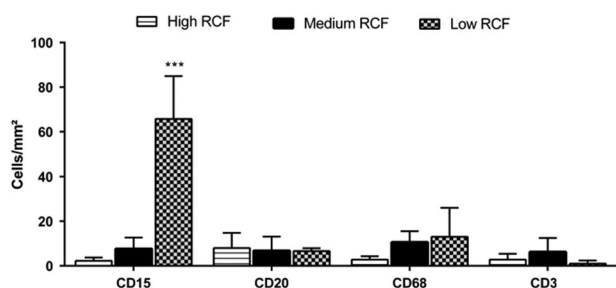
Fig. 4 Statistical analysis of the measured inflammatory cells; CD 15 = neutrophils, CD-20 = B-Lymphocytes, CD-68 = monocytes; CD-3 = T-lymphocytes. There was a statistically significant difference in the amounts of CD-15 positive cells (***$p < 0.001$)

the highest value in the low RCF group, followed by medium RCF and high RCF ($p < 0.01$), with no statistical significance between the low and medium RCF and comparing the medium to the high groups. EGF showed the highest release in the low RCF group, significantly higher when compared to the high RCF group p (<0.05). The medium RCF group also showed a significantly higher rate when compared to the high RCF group (<0.05). Thus, no statistically significant difference was detected between the high RCF and medium RCF groups (Fig. 5a). Similarly, the release of TGF-β1 showed a similar trend whereby the low RCF and medium RCF demonstrated significantly more growth factor release when compared to the high RCF group ($p < 0.001$) and medium RCF was compared to high RCF ($p < 0.001$). In summary, the findings demonstrated that by reducing the RCF, a higher growth factor release of multiple blood-derived growth factors could be observed (Fig. 5b).

Fig. 5 Comparative diagrams for the evaluated growth factor release using ELISA. **a** PDGF-BB, VEGF, EGF. **b** TGF-β1 and MMP-9. Statistical analysis showed significant differences at $p < 0.05$ (*) and highly significant differences at $p < 0.01$ (**) and $p < 0.001$ (***)

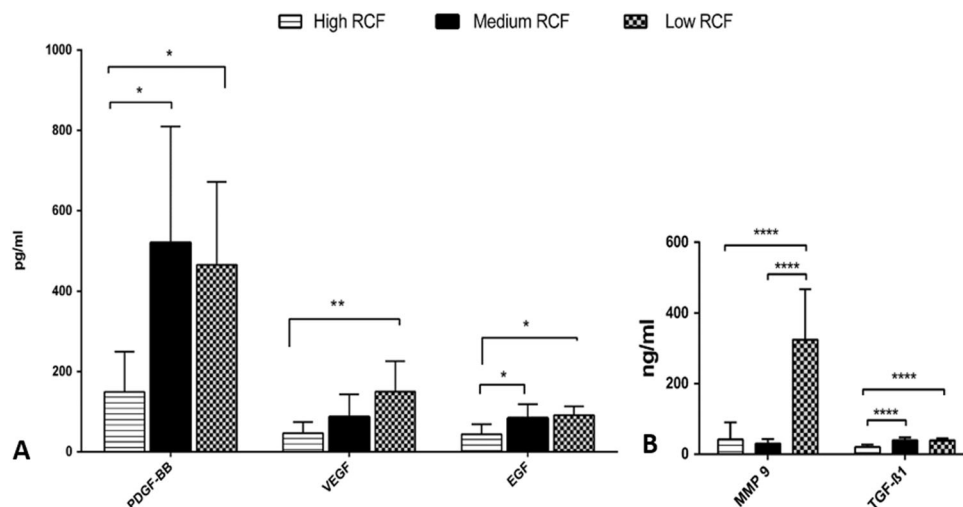## 3.5 Cytokine release

The analysis of MMP 9 showed there was a significantly higher amount within the low RCF group compared to the medium RCF ($p < 0.001$) and high RCF groups ($p < 0.001$). Whereas the medium and high RCF groups had similar values without statistically significant differences. (Fig. 5b).

4 Discussion

The relative centrifugation force and centrifugation time are key elements that could be modified to enhance the structure and composition of PRF-based matrices [2, 8, 10]. Moreover, the introduction of the LSCC (low speed centrifugation concept) showed convincingly that the influence of RCF reduction on injectable and solid PRF-based matrices was responsible for an increase in cell numbers and growth factor release [8, 10]. The present study demonstrated a systematic analysis of the RCF as a consequence of different rpm (revolutions per minute) settings during the preparation of injectable PRF-based matrices. As such, three injectable PRF-based matrices were manufactured following a stepwise decrease in halving the rpm and due to the centrifuge radius of 110 mm, a 4 time RCF decrease (medium RCF) and a 16 time decrease (low RCF) was investigated. We then focused on the number of various inflammatory cells and the release of different growth factors and cytokines within the evaluated PRF-based matrices.

The results from the automated cell counting experiments demonstrated that there was a general trend whereby lower RCF resulted in higher cell numbers. Leukocytes and their subfamilies, i.e., neutrophils and monocytes as well as lymphocytes, were found in significantly higher numbers in the low RCF samples compared to medium and high RCF samples, although no statistically significant differences were observed between the medium and high RCF. Thus, the first RCF reduction produced no significant differences in the mentioned cell types, whereas the second RCF reduction (low RCF) resulted in significantly higher cell numbers within the injectable PRF matrices. This frequently observed phenomenon showed that modification of the RCF had a major impact on the inflammatory cell numbers within the i-PRF matrices. Other than leukocytes and their subfamilies, the influence of RCF on platelets led to significant differences in the first RCF reduction between the high and medium RCF ranges, whereas no statistically significant difference was observed between the medium and low RCF range. These observations indicate that the cellular response to altering the RCF might be sensitive to cell-specific properties, such as weight, size and density. It may be that up to a specific decrease in RCF, the impact on specific inflammatory cells subsides. These findings correlate well with the results of our recent study, which indicated that PRF-based matrices following 8 min of centrifugation prepared with a reduced RCF included a significantly higher number of inflammatory cells compared to a PRF-matrix with a higher RCF application [10]. The results from that study showed sustained significant differences between the high and medium range as well as between the medium and low range regarding leukocytes and platelets. Thus, altering the centrifugation time (from 8 to 3 min) might also have an impact on the included cells within the PRF-based matrices [10]. Therefore, the present results demonstrated that following the LSCC, it was possible to influence the number of specific cells selectively, which might be a promising approach for generating specific PRF-based matrices according to clinical specifications and thus influence cell-cell communication by increasing Leukocytes and platelets that are major players in specific processes associated with wound healing and subsequently improving the regeneration process [15].

General morphological and qualitative histological observations showed that there were obvious differences in the platelets and inflammatory cells. The stepwise decrease in RCF from the high to low RCF range were accompanied by an increased amount of platelets and inflammatory cells. These observations were further confirmed quantitatively using histomorphometry. The results showed a significantly higher rate of platelets and leukocytes in the low RCF groups compared to the high RCF group. In the case of leukocytes, the first step RCF reduction was not associated with significant differences whereas the platelets maintained their number between the high and medium RCF ranges. Additionally, CD-15 positive cells in the case of the low RCF group when compared to the medium and high groups. These results further approve our findings using automated cell count. However, no statistically significant difference was detected between the medium and high RCF groups. In addition, other cells, such as CD-20, CD-3 and CD-68 positive cells showed an increasing trend as RCF decreased but no statistically significant differences were observed between the evaluated groups. In contrast to the histological analysis, there was a major discrepancy in the leukocytes subgroups and lymphocytes results derived from automated cell counting. These observations may be related to the high total number of leukocytes and platelets that is significantly influenced by the RCF reduction. In this case these changes are visible even in a 3–5 μm cross-section of the samples. In addition, due to the comparably small number of each leukocytes subgroup and lymphocytes physiologically existing in healthy blood, these cell groups are affected by the limitations of performing histomorphometric analysis that cannot represent the precise distribution pattern of the whole sample. In contrast, automated cell counting is a more accurate technique that analyzes a defined sample volume and includes all cell numbers representing more precise data, as shown in the results of flow cytometry.

The inflammatory cells evaluated in this study play an essential role in wound healing, which is a common factor in every surgical field [16]. Platelets are involved in primary wound closure and have the capacity to release various signaling molecules, including several growth factors to recruit inflammatory cells to the region of injury [4, 17]. Moreover, leukocytes and their subfamilies, such as neutrophils, monocytes and macrophages, are involved in the regeneration process within different tissue types [18, 19]. Their appearance in the impaired site support angiogenesis and lymphangiogenesis [20]. The cross talk between platelets and leukocytes was previously shown to promote bone regeneration [21]. Furthermore, neutrophils are the main players in the early wound healing phase. They function as phagocytes and release neutrophilic extracellular traps to prevent pathogenic activity and wound infection [22, 23]. The regenerative potential of monocytes in releasing different cytokines and proteins, such as bone morphogenetic protein 2 (BMP-2), has been previously described in the literature [21, 24, 25]. In addition, a recent in vivo study by our group demonstrated that the combination of monocytes isolated from human peripheral blood with bone substitute material resulted in significantly higher vascularization of the implantation bed compared to a pure bone substitute material [14]. Finally, in addition to their immunological role, lymphocytes influence the osteogenic differentiation of mesenchymal stromal cells [26] and release cytokines, such as IL-17, which have a stimulating potential on osteoblasts during new bone formation [27]. Due to the liquid consistency of the injectable PRF, combinations with biomaterials, such as bone substitute granules or collagenous membranes, are possible and might lead to the enrichment of biomaterials with autologous crucial inflammatory cells. Such combinations might be beneficial to enhance the capacity and bioactivity of the applied biomaterials. However, one limitation of the present in vitro study is that it cannot provide any conclusions about functionality of these cells. Thus, further in vivo and clinical studies are needed to demonstrate the extent to which including i-PRF within the wound as well as in combination with biomaterials may influence tissue regeneration [28–33].

The analysis of the growth factors EGF and TGF- β1 revealed the highest growth factor release in the low RCF group that was significantly higher compared to high RCF. However, medium RCF also showed significantly higher growth factor release compared to high RCF. No statistically significant difference was detected between medium and low RCF and similar results were observed for PDGF-BB. These observations made it clear that the decrease in RCF resulted in a higher growth factor release. Therefore, significant differences were only observed when modifying the RCF within a high spectrum field, i.e., from high RCF to medium RCF or high RCF to low RCF. Comparisons between the medium and low RCF range revealed no statistically significant differences. These findings correlated with the prior platelet trend as the RCF amount changed. Therefore, the growth factor release might be related to the number of releasing cells, e.g., platelets. The present results underline the results of our previous in vitro study, which demonstrated that PRF-based matrices prepared according to the LSCC, i.e., reduced RCF release, led to significantly higher values in EGF, TGf-β1 and VEGF over 10 days compared to PRF prepared with a higher RCF [8].

Additionally, VEGF only showed significantly higher values in low RCF compared to high RCF, whereas no statistically significant difference was found between the medium and high range or the medium and low RCF range. In our previous study using an 8 min centrifugation time with various RCFs, more VEGF release was observed at lower RCF ranges when compared to the high RCF range.

In this context, the centrifugation time in combination with a specific RCF range might play a role in growth factor release. The present outcomes made it obvious that for VEGF, modifying the RCF within the high range (i.e., from high to medium) did not influence the VEGF release significantly. In this context, there might be specific RCF ranges in which specific parameters can be influenced selectively to tailor the preparation protocols to the patients' needs and suitable clinical applications. However, further studies are needed to determine this possible postulation. Finally, the cytokine expression of MMP-9 was significantly higher in the low RCF group compared to the other evaluated samples. Thus, no significant differences were found between the high and medium RCF samples.

Growth factors are important signaling molecules in the process of wound healing and tissue regeneration [15]. The enhanced growth factor release within the i-PRF matrices prepared with the LSCC might have the potential to accelerate wound healing and contribute to an improved regeneration pattern in chronic wounds that lack certain growth factors [28]. PDGF is first released from the alpha granules of platelets during the early phases of wound healing and has a high potential to recruit various cells, such as fibroblasts, mesenchymal stem cells and osteoblasts, which emphasizes its vital role in tissue and bone regeneration [29]. During the phases of wound healing, fibroblast migration and collagen synthesis are promoted by TGF-β1, which also has an impact on tissue vascularization [30, 31]. In addition, EGF is involved in supporting cell growth [32], keratinocyte migration [33] and re-epithelialization of wounds [34]. Whereas VEGF is the master regulator for angiogenesis and new vessel formation, which makes it an essential factor for promoting tissue regeneration [35, 36]. For the vascularization process, the required activation and immobilization of VEGF is promoted by matrix metalloproteases, such as MMP-9, which also allow for recruitment of marrow progenitors [37, 38]. In this context, i-PRF-based matrices, especially those prepared according to the LSCC could serve as a reservoir of growth factors and supply the application region with key molecules to support and improve the regeneration process.

The present results showed selective reactions of various growth factors in response to modifying RCF. These findings are probably related to the specific characteristics of particular growth factors and their molecular structure, density and size. Interestingly, platelets exhibited the lowest density compared to other blood-derived inflammatory cells, whereas other cells with a higher density, such as neutrophilic granulocytes, monocytes and lymphocytes, appeared to be significantly influenced additionally in the medium to low RCF spectrum. Due to the composition of the PRF-based matrices and the different included components, it has to be respected that PRF-matrices are a complex system. Therefore, modifying the composition of PRF-based matrices with the LSCC could provide a tool to influence the cell-cell communication by selectively altering a specific growth factor or cell type.

All in all, this systematic approach of RCF decrease demonstrated that using the LSCC, which was demonstrated in different ex vivo, in vitro and in vivo studies, enhanced the regenerative potential by significantly increasing the number of inflammatory cells and growth factor release over time [2, 8, 10]. Thus, PRF-based matrices with enhanced regenerative potential could serve as a drug delivery system and be a useful therapeutic approach in different applications combined with biomaterials in guided bone and tissue regeneration as well as dressing wounds with impaired wound healing. Further in vivo and clinical studies are needed to show the functionality and regenerative potential of this system as well as to explore its impact on wound healing and patient morbidity.

5 Conclusion

The present study showed that decreasing the RCF resulted in a significantly higher number of inflammatory cells, platelets and significantly higher growth factor/cytokine release. However, specific cell types and growth factors were differentially influenced within the different RCF ranges. These findings show that it is possible to modify the components within PRF matrices by selectively modifying the RCF. The liquid consistency of the novel injectable PRF and its improved composition would allow for it to be combined with various biomaterials to increase their biologically activity and potentially enhance the properties of membranes and bone grafts during guided bone and tissue regeneration (GTR/GBR) procedures. Additionally, the results demonstrated that the LSCC (low speed centrifugation concept) led to improved characteristics of PRF-based matrices by reducing the applied RCF. Thus, further preclinical and clinical studies are necessary to investigate whether the application of PRF-matrices generated according to the LSCC will further benefit wound healing.

Compliance with ethical standards

Conflict of interest   The authors declare that they have no competing interests. Joseph Choukroun is the owner of PROCESS. None of the present protocols have been approved yet for clinical application.

References

1. Choukroun J, Adda F, Schoeffler C, Vervelle A. Une opportunité en paro-implantologie: le PRF. Implantodontie 2001; 42:55–62

2. Ghanaati S, Booms P, Orlowska A, Kubesch A, Lorenz J, Rutkowski J, Landes C, Sader R, Kirkpatrick C, Choukroun J. Advanced Platelet-Rich Fibrin: A New Concept for Cell-Based Tissue Engineering by Means of Inflammatory Cells. J Oral Implantol 2014;40:679–89. https://doi.org/10.1563/aaid-joi-D-14-00138

3. Miron RJ, Fujioka-Kobayashi M, Bishara M, Zhang Y, Hernandez M, Choukroun J. Platelet-Rich Fibrin and Soft Tissue Wound Healing: A Systematic Review. Tissue Eng Part B Rev 2017; 23:83–99. https://doi.org/10.1089/ten.TEB.2016.0233

4. Jenne CN, Urrutia R, Kubes P. Platelets: bridging hemostasis, inflammation, and immunity. Int J Lab Hematol 2013;35:254–61. https://doi.org/10.1111/ijlh.12084

5. Schmidt-Bleek K, Kwee BJ, Mooney DJ, Duda GN. Boon and Bane of Inflammation in Bone Tissue Regeneration and Its Link with Angiogenesis. Tissue Eng Part B Rev 2015;21:354–64. https://doi.org/10.1089/ten.TEB.2014.0677

6. Clark Ra. Fibrin and wound healing. Ann N Y Acad Sci 2001; 936:355–67. https://doi.org/10.1111/j.1749-6632.2001.tb03522.x

7. Sahni A, Francis CW. Vascular endothelial growth factor binds to fibrinogen and fibrin and stimulates endothelial cell proliferation. Blood 2000;96:3772–78.

8. El Bagdadi K, Kubesch A, Yu X, Al-Maawi S, Orlowska A, Dias A, Booms P, Dohle E, Sader R, Kirkpatrick CJ, Choukroun J, Ghanaati S. Reduction of relative centrifugal forces increases growth factor release within solid platelet-rich-fibrin (PRF)-based matrices: a proof of concept of LSCC (low speed centrifugation concept), Eur. J Trauma Emerg Surg. 2017. https://doi.org/10.1007/s00068-017-0785-7

9. Miron RJ, Fujioka-Kobayashi M, Hernandez M, Kandalam U, Zhang Y, Ghanaati S, Choukroun J. Injectable platelet rich fibrin (i-PRF): opportunities in regenerative dentistry? Clin Oral Investig 2017. https://doi.org/10.1007/s00784-017-2063-9

10. Choukroun J, Ghanaati S. Reduction of relative centrifugation force within injectable platelet-rich-fibrin (PRF) concentrates advances patients' own inflammatory cells, platelets and growth factors: the first introduction to the low speed centrifugation concept. Eur J Trauma Emerg Surg 2017. https://doi.org/10.1007/s00068-017-0767-9

11. Ghanaati S, Orth C, Unger RE, Barbeck M, Webber MJ, Motta A, Migliaresi C. C. James Kirkpatrick, Fine-tuning scaffolds for tissue regeneration: effects of formic acid processing on tissue reaction to silk fibroin. J Tissue Eng Regen Med 2010;4:464–72. https://doi.org/10.1002/term.257

12. Barbeck M, Lorenz J, Kubesch A, Böhm N, Booms P, Choukroun J, Sader R, Kirkpatrick CJ, Ghanaati S. Porcine Dermis-Derived Collagen Membranes Induce Implantation Bed Vascularization Via Multinucleated Giant Cells: A Physiological Reaction? J Oral Implantol 2015;41:e238–e51. https://doi.org/10.1563/aaid-joi-D-14-00274

13. Barbeck M, Motta A, Migliaresi C, Sader R, Kirkpatrick CJ, Ghanaati S. Heterogeneity of biomaterial-induced multinucleated giant cells: Possible importance for the regeneration process? J Biomed Mater Res—Part A. 2016;104:413–18. https://doi.org/10.1002/jbm.a.35579

14. Barbeck M, Unger RE, Booms P, Dohle E, Sader RA, Kirkpatrick CJ, Ghanaati S, Monocyte preseeding leads to an increased implant bed vascularization of biphasic calcium phosphate bone substitutes via vessel maturation, J Biomed Mater Res—Part A 2016; 1–8. https://doi.org/10.1002/jbm.a.35834

15. Gurtner G, Werner S, Barrandon Y, Longaker M. Wound repair and regeneration. Nature 2008;453:314–21. https://doi.org/10.1038/nature07039

16. Nami N, Feci L, Napoliello L, Giordano A, Lorenzini S, Galeazzi M, Rubegni P, Fimiani M. Crosstalk between platelets and PBMC: New evidence in wound healing. Platelets 2016;27:143–8. https://doi.org/10.3109/09537104.2015.1048216

17. Nurden AT Platelets, inflammation and tissue regeneration, Thromb Haemost; 2011 S13-33. https://doi.org/10.1160/THS10-11-0720

18. Mcnally AK, Anderson JM. Phenotypic expression in human monocyte-derived interleukin-4-induced foreign body giant cells and macrophages in vitro: Dependence on material surface properties. J Biomed Mater Res A 2015;103(4):1380–90. https://doi.org/10.1002/jbm.a.35280

19. Vannella KM, Wynn TA. Mechanisms of Organ Injury and Repair by Macrophages. Annu Rev Physiol 2017;79:593–617. https://doi.org/10.1146/annurev-physiol-022516-034356.

20. Soloviev DA, Hazen SL, Szpak D, Bledzka KM, Ballantyne CM, Plow EF, Pluskota E. Dual Role of the Leukocyte Integrin M 2 in Angiogenesis. J Immunol 2014;193:4712–21. https://doi.org/10.4049/jimmunol.1400202

21. Ekström K, Omar O, Granéli C, Wang X, Vazirisani F, Thomsen P. Monocyte exosomes stimulate the osteogenic gene expression of mesenchymal stem cells. PLoS ONE 2013;8:e75227 https://doi.org/10.1371/journal.pone.0075227

22. Brinkmann V, Reichard U, Goosmann C, Fauler B, Uhlemann Y, Weiss DS, Weinrauch Y, Zychlinsky A. Neutrophil extracellular traps kill bacteria. Science 2004;303:1532–5. https://doi.org/10.1126/science.1092385

23. Mócsai A. Diverse novel functions of neutrophils in immunity, inflammation, and beyond. J Exp Med 2013;210:1283–99. https://doi.org/10.1084/jem.20122220

24. Pirraco RP, Reis RL, Marques AP. Effect of monocytes/macrophages on the early osteogenic differentiation of hBMSCs. J Tissue Eng Regen Med 2013;7:392–400. https://doi.org/10.1002/term.535

25. Omar OM, Granéli C, Ekström K, Karlsson C, Johansson A, Lausmaa J, Wexell CL, Thomsen P. The stimulation of an osteogenic response by classical monocyte activation. Biomaterials 2011;32:8190–204. https://doi.org/10.1016/j.biomaterials.2011.07.055

26. Grassi F, Cattini L, Gambari L, Manferdini C, Piacentini A, Gabusi E, Facchini A, Lisignoli G. T cell subsets differently regulate osteogenic differentiation of human mesenchymal stromal cells in vitro. J Tissue Eng Regen Med 2016;10:305–14. https://doi.org/10.1002/term.1727

27. Croes M, Cumhur Öner F, van Neerven D, Sabir E, Kruyt MC, Blokhuis TJ, Dhert WJ, Alblas J. Proinflammatory T cells and IL-17 stimulate osteoblast differentiation. Bone 2016;84:262–70. https://doi.org/10.1016/j.bone.2016.01.010

28. Kim B-C, Kim HT, Park SH, Cha J-S, Yufit T, Kim S-J, Falanga V. Fibroblasts from chronic wounds show altered TGF-?-signaling and decreased TGF-? Type II Receptor expression. J Cell Physiol 2003;195:331–336. https://doi.org/10.1002/jcp.10301

29. Digiovanni CW, Petricek JM. The Evolution of rhPDGF-BB in Musculoskeletal Repair and its Role in Foot and Ankle Fusion Surgery. Foot Ankle Clin NA. 2010;15:621–640. https://doi.org/10.1016/j.fcl.2010.07.001

30. Lichtman MK, Otero-Vinas M, Falanga V. Transforming growth factor beta (TGF-β) isoforms in wound healing and fibrosis. Wound Repair Regen 2016;24:215–22. https://doi.org/10.1111/wrr.12398

31. Roberts AB, Sporn MB, Assoian RK, Smith JM, Roche NS, Wakefield LM, Heine UI, Liotta LA, Falanga V, Kehrl JH. Transforming growth factor type beta: rapid induction of fibrosis and angiogenesis in vivo and stimulation of collagen formation in vitro. Proc Natl Acad Sci U S A 1986;83:4167–71. http://www.ncbi.nlm.nih.gov/pubmed/2424019 accessed August 19, 2016

32. Alexander PB, Yuan L, Yang P, Sun T, Chen R, Xiang H, Chen J, Wu H, Radiloff DR, Wang X-F. EGF promotes mammalian cell growth by suppressing cellular senescence. Cell Res 2015;25:135–38. https://doi.org/10.1038/cr.2014.141

33. Seeger MA, Paller AS. The Roles of Growth Factors in Keratinocyte Migration. Adv Wound Care 2015;4:213–24. https://doi.org/10.1089/wound.2014.0540

34. Forsberg S, Rollman O. Re-epithelialization from human skin explant cultures is promoted by ligand-activated HER3 receptor. J Dermatol Sci 2010;59:7–15. https://doi.org/10.1016/j.jdermsci.2010.03.017

35. Moens S, Goveia J, Stapor PC, Cantelmo AR, Carmeliet P. The multifaceted activity of VEGF in angiogenesis – Implications for therapy responses. Cytokine Growth Factor Rev 2014;25:473–82. https://doi.org/10.1016/j.cytogfr.2014.07.009

36. Koch S, Claesson-Welsh L. Signal Transduction by Vascular Endothelial Growth Factor Receptors, Cold Spring Harb. Perspect Med 2012;2:a006502–a006502. https://doi.org/10.1101/cshperspect.a006502

37. Carmeliet P, Jain RK. Molecular mechanisms and clinical applications of angiogenesis. Nature 2011;473(7347):298–307. https://doi.org/10.1038/nature10144

38. Heissig B, Nishida C, Tashiro Y, Sato Y, Ishihara M, Ohki M, Gritli I, Rosenkvist J, Hattori K. Role of neutrophil-derived matrix metalloproteinase-9 in tissue regeneration. Histol Histopathol 2010;25:765–70. http://www.ncbi.nlm.nih.gov/pubmed/20376783 accessed September 11, 2016

Annex V

Original article published as collaborative project in the scope of ITN-SNAL:

El Bagdadi, K., Kubesch, A., Yu, X., Al-Maawi, S., Orlowska, A., **Dias, A**., Booms, P., Dohle, E., Sader, R., Kirkpatrick, C. J., Choukroun, J., Ghanaati, S. (2019) Reduction of relative centrifugal forces increases growth factor release within solid platelet-rich-fibrin (PRF)-based matrices: a proof of concept of LSCC (low speed centrifugation concept). Eur J Trauma Emerg Surg. 45, 3, 467-479;

Annex V

CrossMark

ORIGINAL ARTICLE

Reduction of relative centrifugal forces increases growth factor release within solid platelet-rich-fibrin (PRF)-based matrices: a proof of concept of LSCC (low speed centrifugation concept)

K. El Bagdadi[1] · A. Kubesch[1] · X. Yu[2] · S. Al-Maawi[1] · A. Orlowska[1] · A. Dias[1] · P. Booms[1] · E. Dohle[1] · R. Sader[1] · C. J. Kirkpatrick[1] · J. Choukroun[1,3] · S. Ghanaati[1]

Abstract *Purpose* The present study evaluated the platelet distribution pattern and growth factor release (VEGF, TGF-β1 and EGF) within three PRF (platelet-rich-fibrin) matrices (PRF, A-PRF and A-PRF+) that were prepared using different relative centrifugation forces (RCF) and centrifugation times. *Materials and methods* immunohistochemistry was conducted to assess the platelet distribution pattern within three PRF matrices. The growth factor release was measured over 10 days using ELISA. *Results* The VEGF protein content showed the highest release on day 7; A-PRF+ showed a significantly higher rate than A-PRF and PRF. The accumulated release on day 10 was significantly higher in A-PRF+ compared with A-PRF and PRF. TGF-β1 release in A-PRF and A-PRF+ showed significantly higher values on days 7 and 10 compared with PRF. EGF release revealed a maximum at 24 h in all groups. Toward the end of the study, A-PRF+ demonstrated significantly higher EGF release than PRF. The accumulated growth factor releases of TGF-β1 and EGF on day 10 were significantly higher in A-PRF+ and A-PRF than in PRF.

Moreover, platelets were located homogenously throughout the matrix in the A-PRF and A-PRF+ groups, whereas platelets in PRF were primarily observed within the lower portion. *Discussion* the present results show an increase growthfactor release by decreased RCF. However, further studies must be conducted to examine the extent to which enhancing the amount and the rate of released growth factors influence wound healing and biomaterial-based tissue regeneration. *Conclusion* These outcomes accentuate the fact that with a reduction of RCF according to the previously LSCC (described low speed centrifugation concept), growth factor release can be increased in leukocytes and platelets within the solid PRF matrices.

Keywords Inflammation · Leukocytes · Platelets · Platelet-rich-fibrin · Tissue engineering · Vascularization

✉ S. Ghanaati
 shahram.ghanaati@kgu.de

1 FORM (Frankfurt Orofacial Regenerative Medicine) Lab, Department for Oral, Cranio-Maxillofacial and Facial Plastic Surgery, University Hospital Frankfurt Goethe University, Theodor-Stern-Kai 7, 60590 Frankfurt am Main, Germany

2 Department of Orthopedics, West China Hospital/West China School of Medicine, Sichuan University, Chengdu, Sichuan, People's Republic of China

3 Private Practice, Pain Therapy Center, Nice, France

Introduction

Various blood concentrates are used to support tissue regeneration and wound healing in different fields. One of these systems is platelet-rich plasma (PRP), a technique that has been developed for clinical practice and tissue regeneration therapies [1, 2]. PRP is prepared by multiple centrifugation steps using patient blood to which anticoagulants have been added to achieve a platelet-rich concentrate that can be used for different indications [3]. However, seeking to minimize contamination risk, eliminate additional anticoagulants and use the autologous and natural regeneration capacity, a new system, platelet-rich fibrin (PRF), was introduced as the first blood concentrate system without additional anticoagulants [4].

PRF is derived from patient venous blood by means of single-step centrifugation without the further addition of

 Springer

any type of anticoagulants. This system was developed to fulfill clinical needs by being time-saving and easy to use [4]. PRF-based matrices include various inflammatory cells, such as platelets and leukocytes, in combination with various plasma proteins embedded in a fibrin network [5]. The components of PRF-based matrices are known to play an important role during the process of wound healing. Platelets are the first cells to occur in the region of an injury. In addition to their role within hemostasis, platelets have inflammatory potential, including the recruitment of further inflammatory cells, such as neutrophils and macrophages, and promote angiogenesis and tissue repair [6, 7]. In this context, platelets are able to express a series of biologically active signaling molecules and growth factors, such as platelet-derived growth factor (PDGF), vascular endothelial growth factor (VEGF) and transforming growth factor beta (TGF-β). These growth factors are essential for tissue vascularization and new tissue formation [8, 9]. Moreover, platelets contain granules with cytokines, chemokines and other inflammatory mediators that are released after platelet aggregation to enhance hemostasis and activate and recruit cells to the site of inflammation [10, 11]. Leukocytes also contribute to angiogenesis and lymphangiogenesis by participating in cell–cell cross talk and expressing various signaling molecules [12, 13]. The extracellular matrix in the wound bed supports the formation of blood vessels, and fibrin provides a scaffold for the inflammatory cells [14].

The structure and constituents of PRF-based matrices were previously explored by our group. An ex vivo histomorphometrical study showed a dense structure and specific localization of the included inflammatory cells in the lower part of PRF [5]. In addition, a modification of the preparation setting based on the previously LSCC (described low-speed centrifugation concept) is a first step in the reduction of the applied relative centrifugation force (RCF). This step was accompanied by a mild increase of centrifugation time, resulting in a so-called advanced PRF (A-PRF) [5, 15]. Analysis of the structure and composition of A-PRF revealed a more porous structure compared to PRF [5]. In addition, histomorphometrical analysis revealed significantly more neutrophilic granulocytes in the group of A-PRF compared with PRF [5].

While developing PRF-based matrices, the focus was on clot formation, consistency and functional integrity the fibrin clot and the distribution of the included inflammatory cells to generate PRF-based matrices with high functionality and adequate handling. In this study, the applied RCF and centrifugation times are key elements. Further research on PRF-based matrices regarding their structure and composition indicates that adjusting the centrifugation time, i.e., reducing the spinning time and applying the same RCF as in the case of A-PRF, allows the introduction of a new

PRF-based matrix, Advanced-PRF+ (A-PRF+). A previous systematic study demonstrated the influence of the RCF reduction on the leukocyte and platelet numbers as well as their role in growth factor release in fluid PRF-based matrices following the LSCC, which indicates that reducing the RCF enhances the cell number and growth factor release within PRF-based matrices [15]. Based on the LSCC, we examined modifications of the RCF and centrifugation times in solid PRF-based matricesand their influence on the growth factor release within the previously introduced PRF protocols with a solid structure; PRF, A-PRF and A-PRF+. Therefore, the goal of the present study was to determine growth factor release in solid PRF-based matrices, PRF, A-PRF and A-PRF+, at six different time points over a period of 10 days. Additionally, immunohistochemical analysis was conducted to assess the platelet distribution pattern within the various PRF-based matrices.

Materials and methods

PRF preparation

For each protocol, peripheral blood was drawn from four healthy volunteers between 25 and 60 years of age (two females, two males) without a history of anticoagulant usage. Informed consent was obtained from each donor who participated in this study. As previously described [5], the venous blood was collected in 10-ml sterile glass tubes (A-PRF tubes Process for PRF™, Nice, France; Mectron, Cologne, Germany) without external anticoagulants and placed immediately in a centrifuge (Duo centrifuge, Process for PRF™, Nice, France; Mectron, Cologne, Germany). The centrifuge has a fixed angle rotor with a radius of 110 mm and no brake. After centrifugation time, the centrifugation process ends automatically, and the centrifuge stops in 2–5 s. All preparation steps were performed at room temperature according to the established protocols as follows:

- PRF: 10 ml; 2400 rpm; 12 min; 708 g
- A-PRF: 10 ml; 1300 rpm; 14 min; 208 g
- A-PRF+: 10 ml; 1300 rpm; 8 min; 208 g

After centrifugation, all clots were carefully removed from the tubes and separated from the red blood cell fraction with sterile tweezers and scissors.

PRF cultivation

The total clots of PRF, A-PRF and A-PRF+ were placed in separate wells of a 6-well plate (Greiner, Bio-One International) and covered with 5 ml Roswell Park Memorial

Institute medium (RPMI 1640, Gibco Thermo Fischer Scientific) without Fetal Bovine Serum and supplemented with L-glutamine and 1% penicillin/streptomycin. The clots were incubated in a humidified incubator for up to 10 days at 37 °C with 5% CO_2. The supernatants from each well were taken after 6, 24, 48, 72 h, 7 and 10 days and stored as aliquots at −80 °C. At each time point, all of the clots of PRF-based matrices were placed into new wells and covered with 5 ml fresh medium.

Growth factor measurement

The supernatants that were collected from the various PRF-based matrices at different cultivation time points were used for the quantification of different growth factors by enzyme-linked immunosorbent assay (ELISA). All collected supernatants were simultaneously centrifuged (1500 rpm; 5 min.) using a centrifuge (Thermo fisher scientific, Heraeus® Labofuge® 400 R) to exclude possible residue that could affect the photometrical measurement. Before TGF-β1 and EGF ELISA preparation, the supernatants were diluted 1:4 with the same cell culture RPMI medium used for PRF-matrices cultivation. The protein concentrations of human VEGF, TGF-β1 and EGF were determined by the Dou Set ELISA kit (Human VEGF DY293B, R&D Systems, detection range: 2000–31.3 pg/ml), HumanDou Set ELISA kit (Human TGF-β1 DY240, R&D Systems, detection range: 2000–31.3 pg/ml) and the Duo Set DuoSet ELISA kit (human EGF DY236, R&D Systems, detection range: 3.91–250 pg/mL) according to the manufacturer´s instructions. Measurements were conducted using a microplate reader (Infinite® M200, Tecan, Grödig, Austria) set to 450 nm and subtracted at 570 nm from the 450 nm measurements.

Immunohistological analysis

As previously described [5, 16], the PRF clots were collected after 10 days and fixed in Roti®-Histofix 4%, acid free (pH 7), and 4% phosphate-buffered formaldehyde solution (Carl-Roth) for 24 h. The PRF-based matrices were dehydrated in a series of alcohol and xylene through a Tissue Processor (TP1020, Leica Biosystems Nussloch GmbH, Germany) and embedded in paraffin blocks. Afterwards, 3 μm thick sections from each sample were cut by a rotatory microtome (Leica RM2255, Wetzlar, Germany). For immunohistochemistry, the sections were deparaffinized, rehydrated and finally sonicated in citrate buffer (pH 6) at 96 °C for 20 min. The sections were stained with monoclonal mouse anti-human CD61 marker (1:50, Platelet Glycoprotein IIIa/APC, Clone Y2/5, Dako) by means of an autostainer (Lab vision Autostainer 360, Thermo Fisher Scientific). Histological examination was conducted using

a light microscope (Nikon Eclipse 80i, Tokyo, Japan). Three of the authors KE, SA and SG, were independently blinded for the morphological analysis. The microphotographs were prepared with a connected DS-Fi1/Digital camera (Nikon, Tokyo, Japan) and a Digital sight unit DS-L2 (Nikon, Tokyo, Japan).

Statistical evaluation

Data were expressed as the mean ± standard deviation. Statistical analysis was conducted using Prism Version 6 (GraphPad Software Inc., La Jolla, USA). The significance of differences among means of data was analyzed using two-way analysis of variance (ANOVA) with the Tukey multiple comparisons test ($\alpha = 0.05$) of all pairs. The significant differences were regarded as significant if the p values were less than 0.05 ($*p < 0.05$) and highly significant if the p values were less than 0.005 ($**p < 0.005$), 0.0005 ($***p < 0.0005$) or 0.0001 ($****p < 0.0001$).

Results

General observation of fibrin clotting within the three investigated groups

Macroscopic observation demonstrated the formation of three slightly different clots. PRF formed a clot with a fibrin/red blood count (RBC) ratio of 1/1.66, and the clot length was measured as 3.5 cm. A-PRF showed a clot formation with a fibrin/red blood count (RBC) ratio of 1/2. Here the clot length was 3.5 cm. A-PRF+ had a fibrin/red blood count (RBC) ratio of 1/3 and a length of 2.5 cm (Fig. 1). Moreover, while separating the fibrin clot from the RBC, it was observed that in the case of PRF and A-PRF, the adhesion between the two sections, the fibrin clot and RBC, was stronger compared with A-PRF+. Accordingly, the A-PRF+ fibrin clot was much easier to separate.

Growth factor release kinetics from the clots

The present study focused on the determination of the released growth factor kinetics of the three PRF-based matrices, PRF, A-PRF and A-PRF+. The growth factors VEGF, EGF and TGF-β1 were quantified for the released concentrations at each time point (6, 24, 48, 72 h, 7, and 10 days). Additionally, the accumulated growth factor quantities were calculated.

VEGF release

The general trend of the three evaluated groups at each time point was similar. The release of VEGF increased in

PRF   APRF   A-PRF+
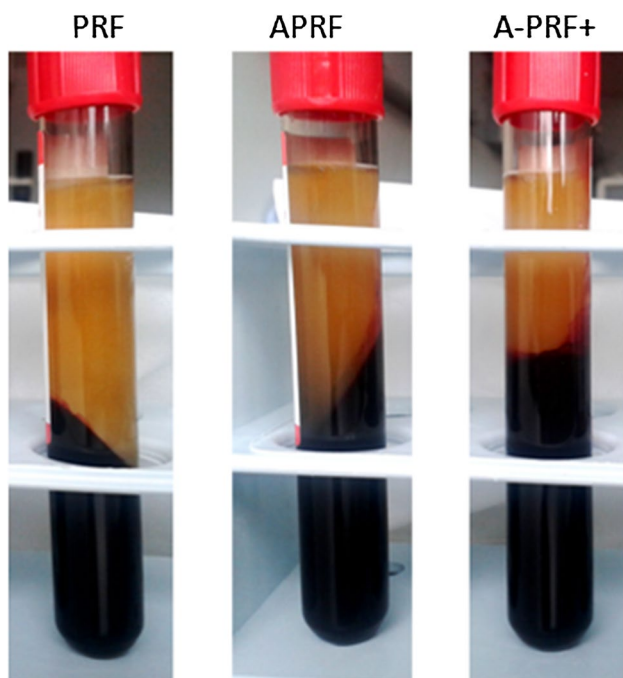
Fig. 1 The PRF-based matrices immediately following centrifugation

the very early phase from 6 to 24 h in all groups. At 48 h, the growth factor release was comparable to the values at 24 h in all groups. From 48 to 72 h, a slight decrease in the release of VEGF was evidenced in all groups. From 72 h to day 7, a highly significant increase in all groups was observed ($p < 0.0005$) in an intra-individual comparison (data not shown). During the 4 days of cultivation between 72 h and day 7, the highest released concentration of VEGF over the study time was measured. Here, A-PRF+ showed the highest concentration when compared with PRF and A-PRF (PRF = 158.5 ± 36.6 pg/ml; A-PRF = 153.6 ± 40.1 pg/ml; A-PRF+ = 242.35 ± 67.9 pg/ml), which was statistically highly significant when compared to PRF and A-PRF ($p < 0.0005$). By contrast, A-PRF showed no statistically significant difference compared to PRF. From day 7 to day 10, all groups showed a decrease in the release of VEGF. This decrease was intra-individually statistically highly significant compared with day 7 (data not shown). Furthermore, after 10 days, A-PRF+ showed the highest VEGF release (PRF = 83.7 ± 28.81 pg/ml; A-PRF = 64.84 ± 15.7 pg/ml; A-PRF+ = 95.5 ± 44.7 pg/ml). At this time point, no significant difference could be identified among the groups (Fig. 2a1).

Concerning the accumulated VEGF concentration, a general trend was also evidenced by a continuous increase in the released VEGF over the study time. In the early phase (6–72 h), the release of VEGF increased in all groups, whereas the groups' concentrations were quite

similar. Moreover, in the late study period (72 h–10 days), a similar tendency was observed in all groups. However, A-PRF+ released the highest concentration on day 10 when compared with PRF and A-PRF (Table 1). This difference was highly significant when comparing A-PRF+ to A-PRF (***$p < 0.0005$) and significant comparing A-PRF+ to PRF (**$p < 0.005$) at this time point (Fig. 2 a2).

TGF-β1 release

Various TGF-β1 release patterns were measured in PRF, A-PRF and A-PRF+. Within the PRF group, a slight increase was observed in the early study time (6–72 h) followed by a dramatic decrease in the late study time (72 h–10 days). At 72 h, PRF already showed the highest concentration over the study period. At this time point, PRF was significantly higher only when compared to A-PRF ($p < 0.0001$), whereas no significant difference was observed compared to A-PRF+ (Fig. 2b1).

The A-PRF group showed a high release value at the first time point (6 h) (PRF = 4.6 ± 1.0 ng/ml; A-PRF = 7.0 ± 1.4 ng/ml; A-PRF+ = 5.8 ± 1.4 ng/ml), the difference between A-PRF and PRF being statistically significant ($p < 0.05$). However, no statistically significant difference was detected regarding A-PRF+. This observation was followed by irregular behavior until 72 h and a significant increase at day 7, when the highest TGF-β1 release of A-PRF was observed. At this time point, A-PRF was significantly higher than PRF ($p < 0.0001$), whereas no significant difference was revealed for the A-PRF+ group.

A-PRF+ showed a mild decrease of the released TGF-β1 at the early study time (6–48 h). However, from 72 h to day 7, an increase in the released TGF-β1 was observed when the highest concentration of TGF-β1 release was reached in the case of A-PRF+. At day 7, a statistically highly significant difference was observed when compared with PRF ($p < 0.0001$), whereas no significant difference was observable compared to A-PRF (PRF = 1.9 ± 1.6 ng/ml; A-PRF = 8.5 ± 0.6 ng/ml; A-PRF+ = 8.6 ± 0.4 ng/ml). From day 7 to day 10, the release of TGF-β1 decreased in all groups. However, A-PRF showed significantly higher values when compared with PRF ($p < 0.0001$). Similarly, A-PRF+ revealed more growth factor release, which was highly significant when compared with PRF ($p < 0.0001$). No statistically significant difference was observed when comparing A-PRF and A-PRF+ at this time point (Fig. 2b1).

The accumulated concentration of TGF-β1 showed an increase in all groups at the early study time (6–72 h). However, at the late study time (72 h–10 days), the growth factor release differed among the various groups. PRF showed a more or less constant concentration of TGF-β1 after 72h, whereas in the case of A-PRF and A-PRF+, an
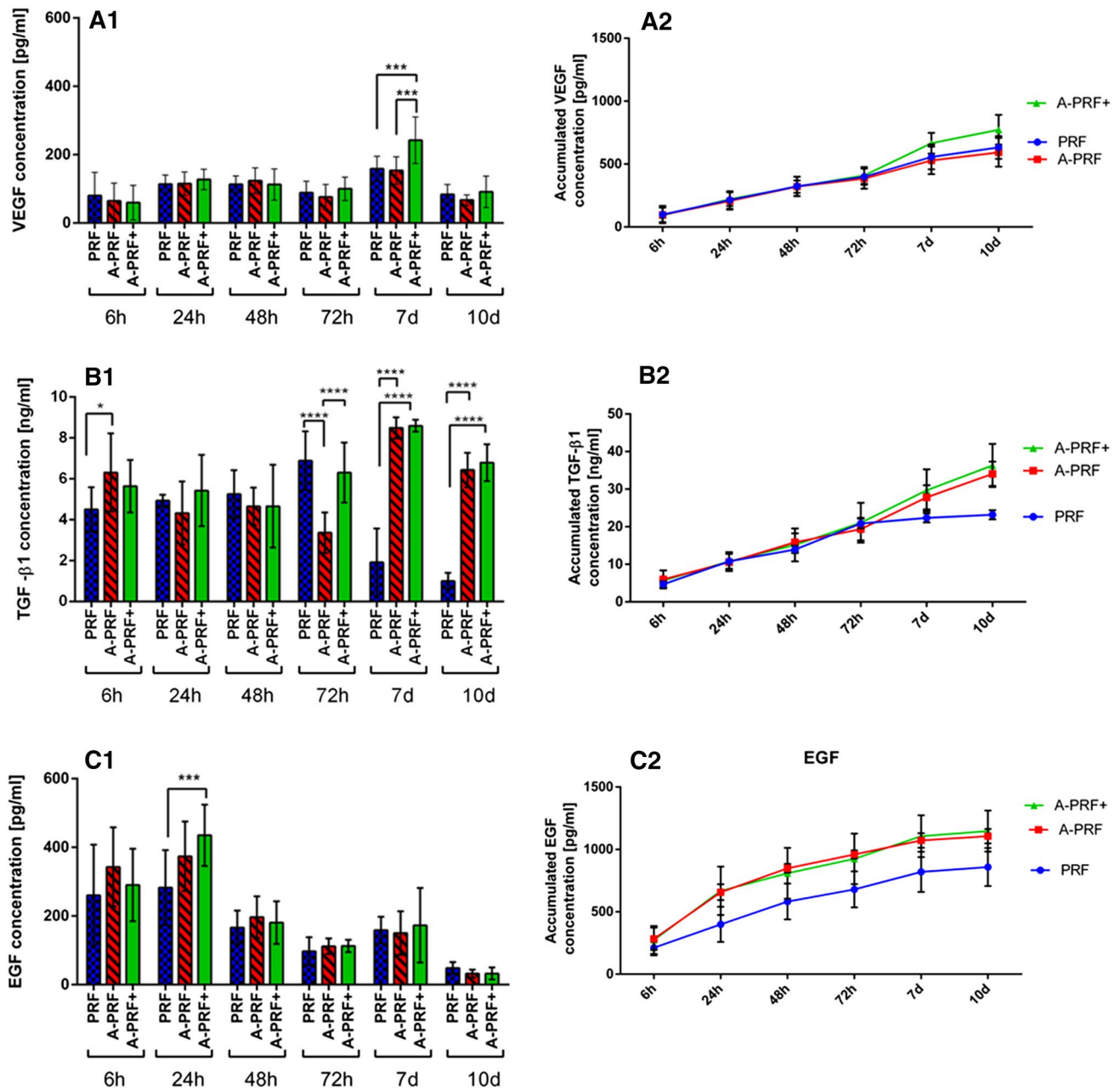
Fig. 2 Statistical analysis of the growth factor releases by time points as the mean ± standard deviation for PRF, A-PRF and A-PRF+. **a1** VEGF, **b1** TGF-β1 release, **c1** EGF release, (*$p < 0.05$), (***$p < 0.0005$), (****$p < 0.0001$). Total accumulated growth factor concentration over 10 days. **a2** VEGF, **b2** TGF-β1, **c2** EGF

Table 1 Accumulated growth factor concentration of PRF, A-PRF and A-PRF+ at day 10 as the mean ± standard deviation. Statistical analysis of A-PRF and A-PRF+ compared with PRF (*$p < 0.05$), (**$p < 0.005$), (***$p < 0.0005$), (****$p < 0.0001$)

Growth factor	PRF	A-PRF	A-PRF+
VEGF (pg/ml)	632.26 ± 90.58	593.15 ± 114.08	773.88 ± 117.66**
TGF β1 (ng/ml)	23.18 ± 1.22	34.081 ± 3.21****	36.29 ± 5.73****
EGF (pg/ml)	858.62 ± 152.90	1106 ± 57.74*	1147.07 ± 164.47**

increased TGF-β1 concentration was observed. These differences on day 10 were statistically significant when comparing A-PRF to PRF ($p < 0.0001$) and A-PRF to PRF ($p < 0.0001$); however, no statistically significant difference was detected when comparing A-PRF to A-PRF+ (Table 1) (Fig. 2b2).

EGF release

A general trend was observed in all three PRF-based matrices. The rate of the released EGF increased quite early in the study time (6–24 h) to reach the highest value in all groups at 24 h. At this time point, A-PRF+ showed the highest value of the released EGF when compared with PRF and A-PRF (PRF $= 282.69 \pm 109.09$ pg/ ml; A-PRF $= 373.75 \pm 101.25$ pg/ml; A-PRF+ $= 435.17 \pm 89.29$ pg/ml), the difference being statistically highly significant when comparing A-PRF+ to PRF (***$p < 0.0005$); no statistical significance was observed when comparing A-PRF to A-PRF+. Subsequently, a course change was observed when a strong reduction of the released EGF occurred in all examined groups until 72 h. After that, on day 7, a slight increase was observed in all groups. Here also, A-PRF+ was the highest (PRF $= 148.28 \pm 48.27$ pg/ml; A-PRF $= 138.70 \pm 61.07$ pg/ ml; A-PRF+ $= 173.50 \pm 98.72$ pg/ml) although no statistically significant difference was detectable. At the last evaluated time point on day 10, all groups showed a significant decrease in the released EGF compared with day 7 (data not shown). However, at this time point, no statistically significant differences were observed among the groups (Fig. 2c1).

The accumulated concentration of the released EGF also exhibited a general trend. All groups showed a similar curve progression in the form of increased EGF release over the study time. A-PRF and A-PRF+ also displayed similar values. Early in the study time, a remarkable increase in released EGF was evidenced in all groups. After 72 h, only a minor increase of the released EGF was observed toward the end of the study on day 10. At these time points (72 h–10 days), A-PRF and A-PRF+ showed statistically significantly higher release values when compared with PRF (A-PRF+ compared with PRF $p < 0.005$; A-PRF compared with PRF $p < 0.05$), whereas no statistically significant differences were revealed when comparing A-PRF to A-PRF+ (Table 1) (Fig. 2c2).

Platelet distribution in the PRF-based matrices

Immunohistochemical staining with CD-61 antibodies against platelets was conducted to determine the platelet distribution in cross sections of the three PRF-based matrices. The platelet distribution was evaluated with regard to the location in the clot. The platelets formed accumulations within all three clots. PRF, which was prepared with a high RCF, showed a different distribution pattern according to the localization. The upper and middle portions of the clot showed only a few platelets, whereas the majority of platelets were distributed in the lower portion of PRF (Fig. 3). By contrast, A-PRF, which was prepared with a reduced RCF, presented a different distribution pattern. Platelets were dispersed all over the clot (Fig. 4). A-PRF+ with a reduced RCF and a reduced centrifugation time also displayed an even platelet distribution pattern in the various locations within the clot (Fig. 5).

Discussion

This study presents the potential of PRF-based matrices (PRF, A-PRF and A-PRF+) for growth factor release as a modest contribution to ongoing discussions regarding the preparation of PRF-based matrices as biological scaffolds and a natural growth factor release system, which is derived from autologous blood. The results revealed continuous growth factor release of VEGF, TGF-β1 and EGF over the study time. However, statistically significant differences among the various preparation protocols, PRF, A-PRF and A-PRF+, were demonstrated.

One of the most potent angiogenesis-stimulating growth factors is VEGF. A-PRF+ released significantly more VEGF than PRF and A-PRF on day 7. Moreover, the accumulated release of VEGF on day 10 was significantly higher in A-PRF+ than in PRF and A-PRF. However, no statistical significance was detected when evaluating A-PRF and PRF. These outcomes are quite likely related to the specific fibrin structure and cellular distribution pattern of A-PRF+. VEGF plays a crucial role in wound healing and tissue regeneration to promote vascularization and new vessel formation [17]. Additionally, previous studies have demonstrated that the sustained release of VEGF promotes epithelialization and enhances collagen tissue deposition in a skin wound healing model in mice [18]. Thus, the sustained and enhanced VEGF release of A-PRF+ could lead to more benefits in regeneration and vascularization and thus provide a nutrient supply to support wound healing and improve the biomaterial-guided regeneration pattern.

The release of TGF-β1 in A-PRF and A-PRF+ indicated the maximal release values on days 7 and 10, which were significantly higher when comparing A-PRF to PRF and A-PRF+ to PRF. However, no statistically significant difference between the TGF-β1 release of A-PRF and A-PRF+ was identified. On day 10, the accumulated TGF-β1 concentration was significantly higher in the A-PRF and A-PRF+ groups than in the PRF group. By contrast, A-PRF and A-PRF+ revealed no statistically
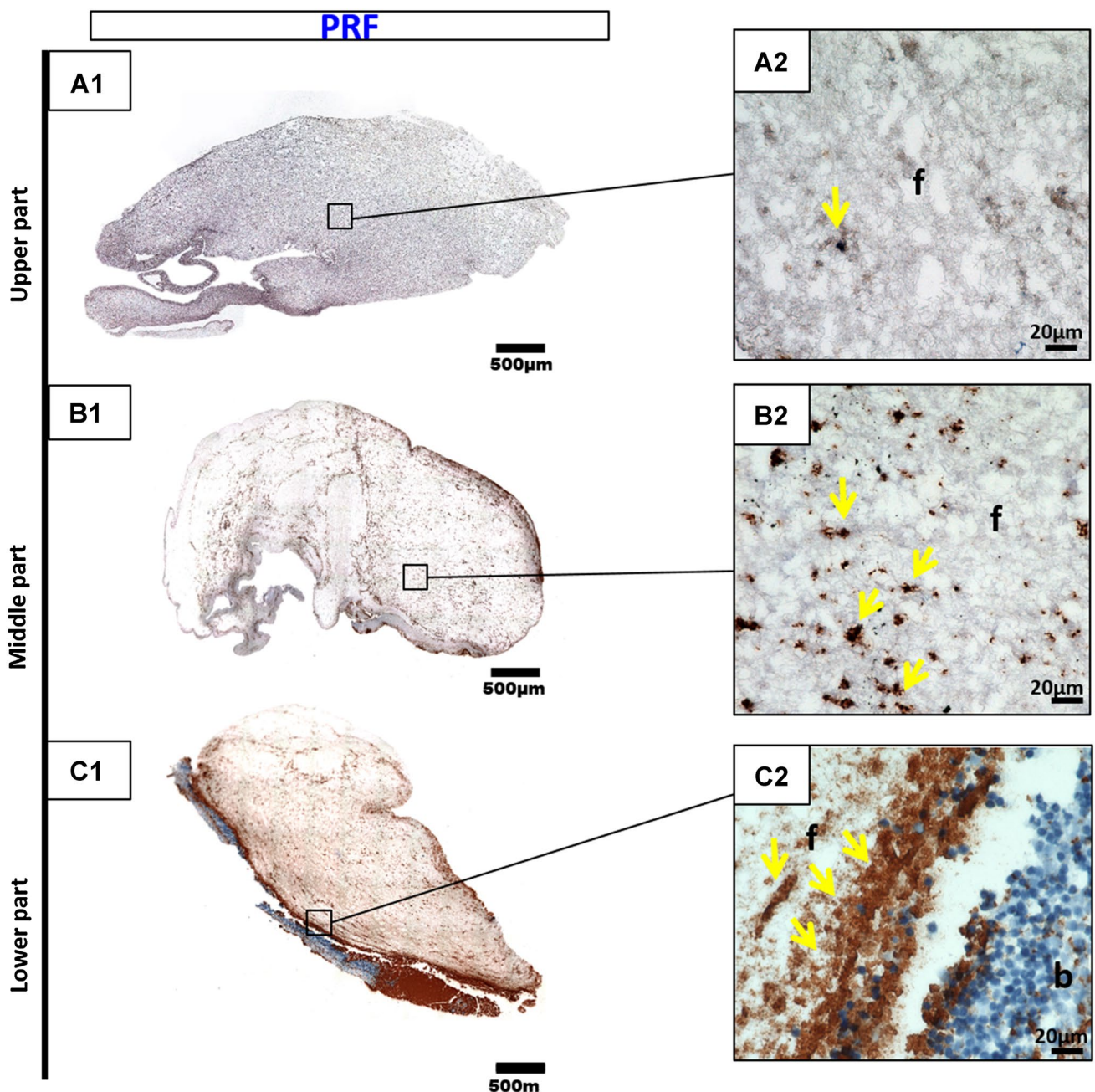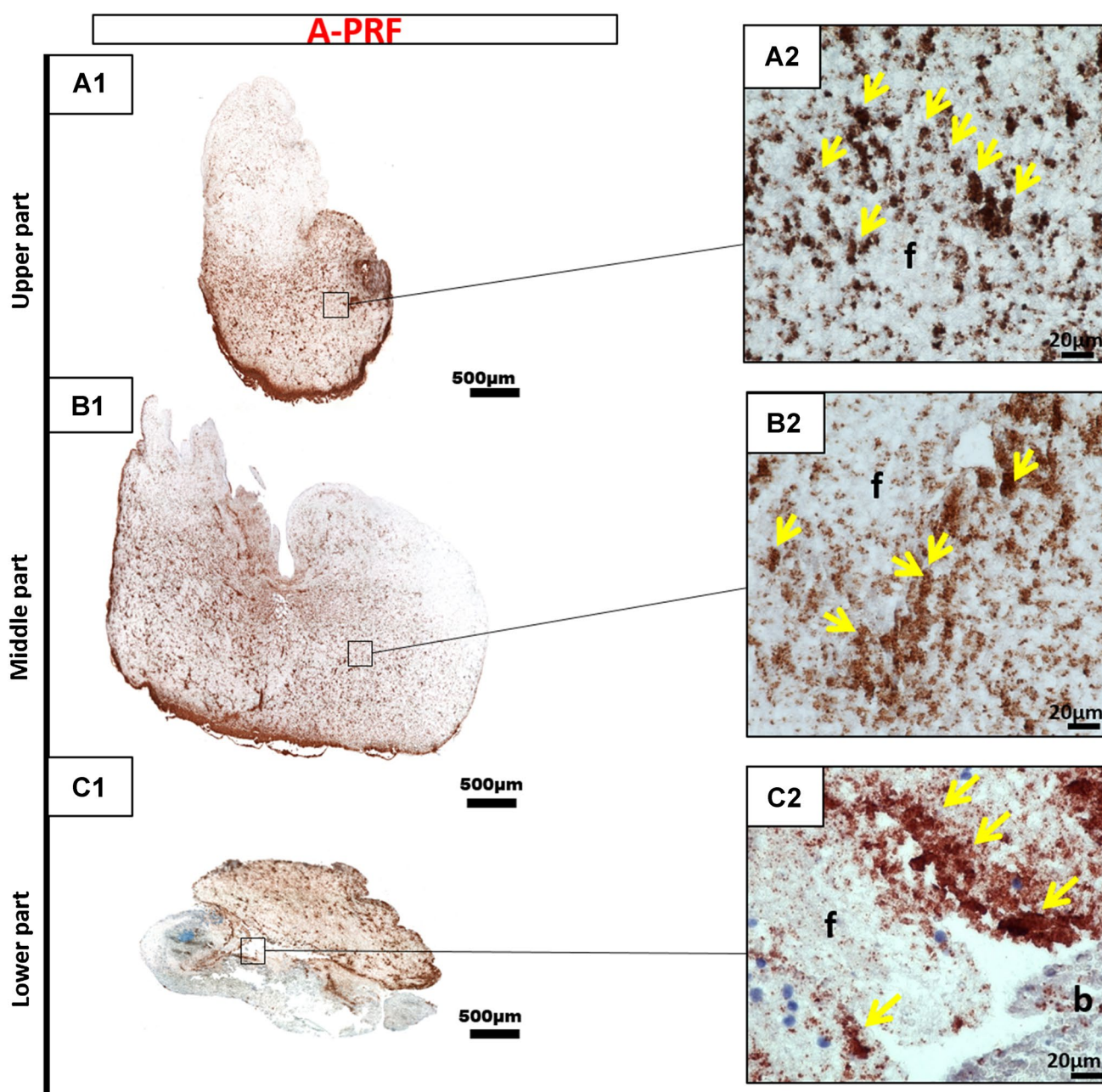
Fig. 3 CD-61 immunohistochemical analysis of PRF according to the different regions. **a1, a2** upper portion; **b1, b2** middle portion; **c1, c2** lower portion (**a1, b1, c1** total scan sections; ×100 magnification, *scale bar* 500 μm). **a2, b2, c2** show the distribution pattern of platelets (*yellow arrows*) in higher magnification (*f* fibrin; *b* buffy coat; ×400 magnification; *scale bar* 20 μm)

significant difference in this case. TGF-β 1 is essential for wound healing [19]. Chronic wounds were observed to have a decreased expression of TGF-β receptors [20]. Thus, PRF matrices with an enhanced release of TGF-β1, as was the case for A-PRF and A-PRF+, could have a major influence on wound healing as a catalyzer of wound repair stages. In addition, this growth factor is known to stimulate fibroblast migration, enhance collagen synthesis and promote angiogenesis [21, 22]. All of the latter characteristics are essential in the biomaterial-based regeneration process. Hence, PRF-based matrices as an additional autologous dose of inflammatory cells and growth factor could be promising in the field of guided bone and tissue regeneration (GTR and GBR), in which biomaterials should provide a scaffold and support the regeneration process in the defect area.
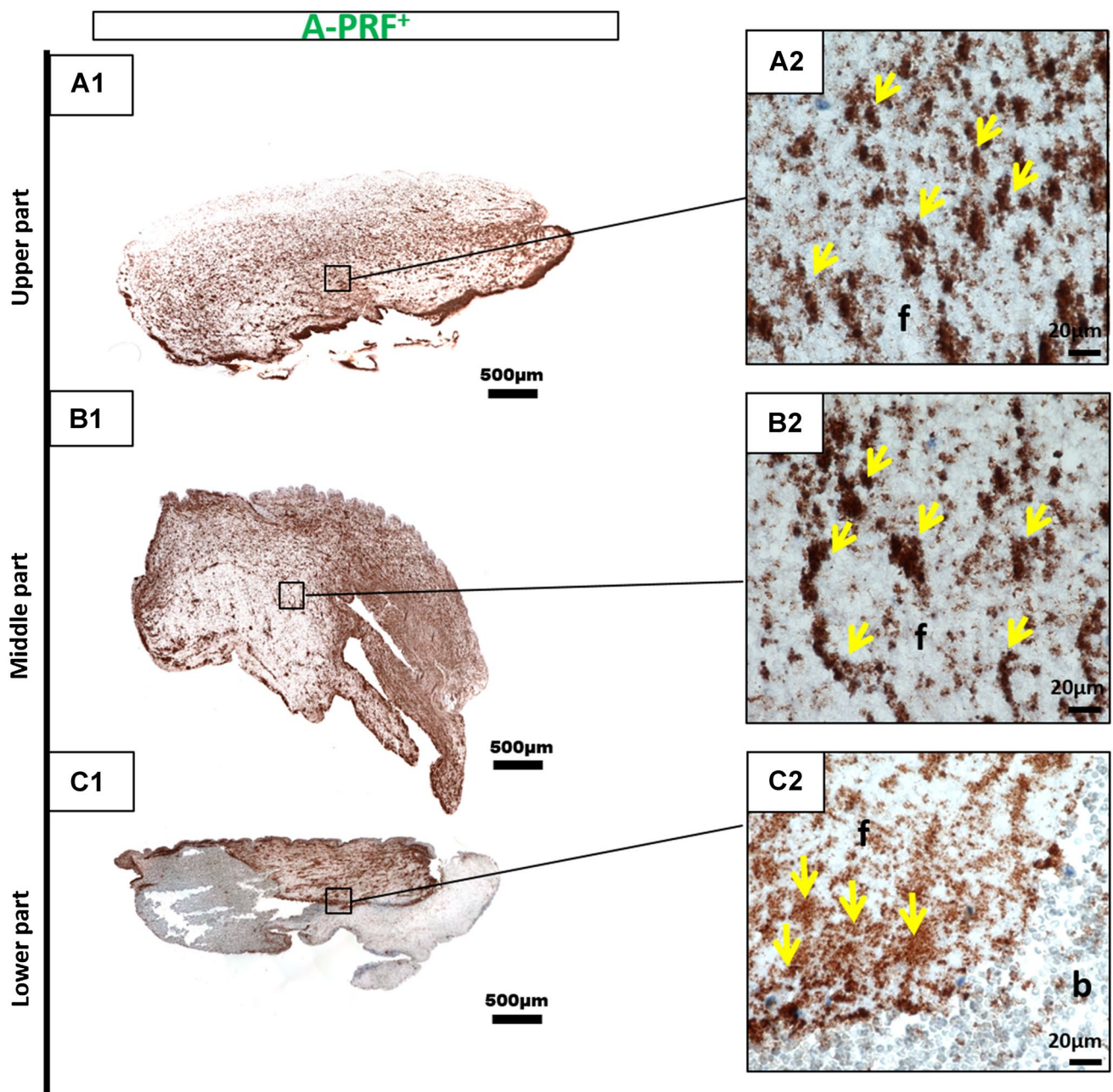
Fig. 4 CD-61 immunohistochemical analysis of A-PRF according to the different regions. **a1, a2** upper portion; **b1, b2** middle portion; **c1, c2** lower portion (**a1, b1, c1** total scan sections; ×100 magnification, scale bar 500 μm). **a2, b2, c2** Show the distribution pattern of platelets (*yellow arrows*) in higher magnification (*f* fibrin; *b* buffy coat; ×400 magnification; *scale bar* 20 μm)

The release of EGF was generally higher in the A-PRF and A-PRF+ groups when compared with PRF. Statistically highly significant differences were detected when comparing A-PRF+ with PRF after 24 h, whereas no significant difference was observed between A-PRF+ and A-PRF. The accumulated EGF release showed significantly higher rates in the case of A-PRF and A-PRF+ compared with PRF at most time points, particularly on day 10. EGF has previously been described as promoting cell growth [21], enhancing keratinocyte migration [23], inhibiting apoptosis under hypoxic conditions [24], and supporting re-epithelization and skin healing [25, 26]. Additionally, EGF supports the healing process of chronic wounds [27], non-healing chronic wounds and ulcers, which are, for example, observed in diabetic patients known to lack the necessary growth factors to maintain the healing process [28, 29]. Thus, such patient groups may benefit from the application of PRF matrices as an autologous drug delivery system.

Fig. 5 CD-61 immunohistochemical analysis of A-PRF+ according to the different regions. **a1, a2** upper portion; **b1, b2** middle portion; **c1, c2** lower portion (**a1, b1, c1** total scan sections; ×100 magnifi-cation, *scale bar* 500 μm). **a2, b2, c2** Show the distribution pattern of platelets (*yellow arrows*) in higher magnification (*f* fibrin; *b* buffy coat; ×400 magnification; *scale bar* 20 μm)

Moreover, immunohistochemical evaluation indicated an equal distribution pattern of platelets in all clot regions in the case of A-PRF and A-PRF+, whereas in PRF, the majority of the platelets were located in the lower portion of the clot. These findings may be related to the LSCC (low speed centrifugation concept), indicating that reducing the applied RCF increases the number inflammatory cells and platelets as well as the growth factor release within the PRF-based matrices [15]. Because the centrifugation process depends on cell weight and density, a higher RCF may be the reason for the sedimentation of the majority of the platelets to the lower portion of the clot according to their density and size, as observed in PRF. Decreasing the RCF allows the platelets to become separated from the red blood cell phase and become equally distributed within the fibrin network. The effectiveness of PRF clots with low platelet counts and uneven platelet distribution may have less influence on clinical outcomes than clots with

evenly distributed and enhanced platelet numbers because the applied clot could have uneven biological activity and thus a reduced growth factor release, as indicated in the present study. However, comparative clinical studies are necessary to evaluate the advanced PRF matrices presented here to demonstrate the extent to which the improved structure, even cellular distribution and enhanced growth factor release may affect clinical outcomes.

These observations highlight the influence of RCF reduction, i.e., from PRF (708 g) to A-PRF and A-PRF+ (208 g) on platelet distribution, thereby correlating with the previously demonstrated automated cell counting that indicated significantly more platelets in PRF matrices prepared with low RCF than with high RCF application [15]. A previous *ex vivo* immunohistochemical study demonstrated the distribution pattern in PRF and A-PRF, which included, in addition to platelets, a wide range of inflammatory cells that physiologically exist within the peripheral blood, such as leukocytes, including neutrophils and monocytes as well as lymphocytes [5]. However, further immunohistochemical studies are required to determine the distribution pattern of the included leukocytes and their subgroups, particularly in A-PRF+. These cells, particularly platelets and neutrophilic granulocytes, contribute to neoangiogenesis and VEGF release [30, 31]. In addition, platelets are the primary secretory cells of EGF and TGF-β1 [32]; thus, their presence within the PRF-based matrices is a possible explanation for the observed growth factor release. These cells are essential for wound healing and tissue regeneration [33, 34]. In the present study, release kinetics displayed an increased growth factor release over the study time and a maximum at day 7 in the case of VEGF and TGF-β1 as well as an increased growth factor release at 24 h in the case of EGF. Based on the growth factor and release kinetics demonstrated here, one may assume that the growth factor release pattern within the various PRF-based matrices is an active release from living cells within the different PRF clots, which most likely experienced apoptosis during the study period if 10 days reflects the reduction in growth factor release at day 10 compared with day 7 in all groups and growth factors.

Additionally, leukocytes and platelet interaction via cellular cross talk have been described in bone regeneration [9]. In this context, the high regeneration potential of advanced PRF-based matrices could be beneficial in various clinical applications, such as enhancing the regeneration pattern of biomaterials in terms of GTR and GBR. Moreover, autologous biologizing biomaterials using PRF-based matrices may improve the regeneration pattern in large-sized, soft and bony defects to catalyze wound healing and regeneration. Ongoing clinical observations in oral- and maxillofacial surgery have demonstrated that various bony defects within the jaw or head can be regenerated by

different clot numbers according to the defect size. Thus, molar sockets are treated with 2–3 clots, whereas larger bony head defects are treated with up to 6 clots. Based on these observations, PRF-based matrices could be a beneficial tool to improve the regeneration of soft and bony defects after orthopedic or trauma surgery. The present study demonstrates that the application of the LSCC (low speed centrifugation concept), by decreasing the RCF from PRF toward A-PRF and A-PRF+, results in a significantly higher release of VEGF, TGF-β1 and EGF. Notably, the accumulated release over 10 days of TGF-β1 and EGF supports the relation between the reduction of RCF and the growth factor release. Hence, A-PRF+ and A-PRF, which were prepared with the same RCF, displayed comparable results that were significantly higher than PRF, which was prepared with more than three times higher RCF. These observations emphasize the fact that the application of the LSCC is valuable in modifying and optimizing solid PRF-based matrices. However, the manipulation of the centrifugation time appeared to influence only certain growth factors, as shown in the case of A-PRF+. The accumulated VEGF release on day 10 showed a significantly higher rate in the group of A-PRF+ compared with A-PRF and PRF. It may be that the application of a low RCF but a longer centrifugation time, as demonstrated in the case of A-PRF, affected the VEGF release capacity, whereas the application of a low RCF and slightly decreased centrifugation time, as in A-PRF+, resulted in a significantly higher VEGF release. Another plausible explanation may be that the specific fibrin clot composition of A-PRF+ allows a highly increased VEGF release and thus a higher accumulated VEGF release on day 10. These data accentuate the fact that the various growth factor concentrations may be a consequence of the various total cell concentrations within the PRF-based matrices.

The various release profiles of the evaluated PRF-based matrices may also be a consequence of the different growth factor binding affinities to fibrin. It has been demonstrated that growth factors, such as VEGF, have a high affinity to bind to fibrinogen and fibrin so that those factors are released in a sustained manner [35]. This information is reflected in the present results by showing significantly enhanced VEGF release on day 7 in the case of A-PRF+. By contrast, EGF is released in a high concentration level at the very early time point of 24 h. One explanation for this observation may be the low binding affinity of EGF to fibrin and fibrinogen [36]. Another factor may be the structure of the PRF-based matrices. A-PRF and A-PRF+ exhibit a more porous structure than the densely structured PRF [5]. The physical properties of the clot and the specific fibrin structure related to the manufacturing protocol [5] may also influence the binding affinity and the sustained release of the various

growth factors. It is possible that a more porous structure, as shown in A-PRF and A-PRF+, is one reason for an enhanced growth factor release [5]. Thus, it remains questionable whether the growth factor release is related to the specific physical properties of the fibrin network or to the included inflammatory cells and platelets, or perhaps a combination of both. Therefore, further study is required to understand this specific complex system.

The release kinetics of growth factors in the PRF-based matrices have previously been reported in several studies [37, 38]. Direct comparisons of these studies are limited because of the various preparation protocols in terms of RCF, centrifugation time, blood volume and the techniques used to generate the PRF-based matrices. However, one in vitro study analyzed the growth factor release in PRF-based matrices compared with PRP [39]. Correlations were demonstrated in the case of the accumulated TGF-β1 and EGF, for which both studies presented a significantly higher growth factor release in PRF matrices prepared with a low RCF application compared with PRF matrices with high RCF exposure. This accentuates the fact that reduction of the RCF enhances the release of these growth factors. Notably, the later study also showed that PRP released higher growth factor concentrations (EGF, VEGF and TGF-β1) at the very early time points, whereas PRF-based matrices showed a continuous and higher growth factor concentration over a period of 10 days [39]. Moreover, this group demonstrated further evaluation of the growth factors in PRF, A-PRF and A-PRF+ [40]. The results of the accumulated growth factor release on day 10 are consistent with the present findings with regard to A-PRF+ concerning TGF β1 and EGF. Both studies presented a significantly higher release of these growth factors within A-PRF+ when compared with PRF. By contrast to Kobayashi et al. (2016), the present study reveals no significant differences between A-PRF and A-PRF+ with regard to TGF β1 and EGF. Additionally, the present outcomes indicate significantly higher accumulated VEGF release on day 10 in the group of A-PRF+ compared with A-PRF and PRF, whereas Kobayashi et al. (2016) showed no statistically significant differences between the examined groups on day 10. At this point, it must be stressed that the two studies were of different designs. Kobayashi et al. (2016) evaluated different time points from the time points investigated in the present study. In addition, Kobayashi et al. (2016) used a shaking incubator before performing the ELISA evaluation, whereas our group incubated the PRF-based matrices without further manipulation, which can also be a reason for the discrepancies revealed in the results. It is evident that detection of the specific growth factors is dependent on the specific methods employed. Thus, further studies in this field are necessary to develop and evaluate PRF-based matrices generated according to LSCC.

The present experimental design regarding the preparation and cultivation of PRF-based matrices may offer advantages because the PRF clots were not compressed or manipulated but nevertheless yielded the large amount of growth factors in the PRF clot. Furthermore, the clots were incubated in a cell culture environment to provide adequate gas exchange and optimal conditions for cells. The primary limitation of this study is the in vitro system issue. A comparison with clinical results is difficult because of the discrepancy of comparing the physiological environment in vivo. Thus, the cellular crosstalk and enzymatic degradation of the fibrin network would be different in vivo. Further in vivo studies are required to determine the influence of the growth factors on the regeneration pattern of PRF-based matrices, particularly those matrices that are prepared according to the LSCC. This is necessary to identify out whether the observed inflammatory cell and growth factor enhancement will contribute to an improved regeneration potential in vivo. Moreover, the optimal release of growth factors required in wound healing and regeneration processes remains unclear, as is whether enhancing the amount released will indeed lead to improved performance. Thus, controlled clinical studies are essential to evaluate the regeneration potential of A-PRF and A-PRF+ and to establish the extent to which homogeneously distributed platelets and an enhanced growth factor release in addition to the porous structure will contribute to improved wound healing.

Less is known regarding the interaction of the PRF-based matrices with biomaterials with a view to improving biomaterial-based regeneration. In addition, little attention has been focused on the composition of PRF-based matrices obtained from patients undergoing pharmacologic treatments and whether the growth factor release will be influenced by medication. In addition, the regeneration potential of the PRF-based matrices may also be related to the age of the donor. Therefore, it may be that as the age of donors increases, less growth factor is released and vice versa. If this scenario is true, PRF-based matrices with enhanced growth factor release may be beneficial in these specific cases. In this respect, the determination of mononuclear cell growth in PRF and penetration into the PRF-based matrices as a simulation of the regeneration process in vitro would be of interest in understanding the role of PRF-based matrices in biomaterials and tissue engineering. Hence, further studies of the PRF-based matrices as a complex system that influences cell growth and differentiation and provides a growth factor reservoir remain necessary.

Additionally, the current PRF-based matrices were prepared according to specific protocols with a defined amount of blood. However, it would be interesting to determine how increasing or decreasing the blood volume influences the composition of the prepared PRF-based matrices, their

regenerative potential and their growth factor release. These questions are current investigation topics of our research group as we seek to enhance wound healing and tissue regeneration to decrease patient morbidity. Hence, the outcomes of this study could provide new clinical approaches in tissue and bone regeneration in terms of a combination of biomaterials with PRF-based matrices. Nevertheless, further studies, particularly clinical studies, are required to develop optimized, standardized and tailored preparation protocols for various clinical applications and to demonstrate their advantages now and in the future.

Conclusion

The present study demonstrates the influence of RCF reduction on the growth factor release and platelet distribution in solid PRF-based matrices. A-PRF+, prepared with a reduced RCF, displayed significantly higher VEGF concentration over the study period of 10 days than A-PRF and PRF, which exhibited no statistically significant difference. EGF and TGF-β1 were comparable in A-PRF and A-PRF+, which were significantly higher than PRF. Additionally, the platelet distribution pattern appeared to be equivalent in all regions concerning A-PRF and A-PRF+, whereas PRF showed the largest accumulation of platelets in the lower portion of the clot. Long-term, sustained and slow release of growth factors from all of the PRF groups may support cell migration and cell proliferation as well as offer advantages in the wound healing process. However, the significantly enhanced release in A-PRF and A-PRF+ may render these matrices superior to PRF in specific clinical indications. These promising findings offer an excellent handling efficiency and new approaches to the clinical application of wound healing as well as soft and bone tissue regeneration. Nevertheless, further clinical studies must demonstrate the extent to which the application of LSCC to generate A-PRF and A-PRF+ will benefit clinical outcomes.

Compliance with ethical standards

References

1. Albanese A, Licata ME, Polizzi B, Campisi G. Platelet-rich plasma (PRP) in dental and oral surgery: from the wound healing to bone regeneration. Immun Ageing. 2013;10:23. doi:10.1186/1742-4933-10-23.
2. Intini G. The use of platelet-rich plasma in bone reconstruction therapy. Biomaterials. 2009;30:4956–4966. doi:10.1016/j.biomaterials.2009.05.055.
3. Textor J. Platelet-rich plasma (PRP) as a therapeutic agent: platelet biology, growth factors and a review of the literature, in: platelet-rich plasma. Regen Med Sport Med Orthop Recover Musculoskelet Inj. 2013;61–94. doi:10.1007/978-3-642-40117-6_2.
4. Choukroun J, Adda F, Schoeffler C, Vervelle A. An opportunity in paro-implantology: PRF (in French). Implantodontie. 2001;42:55–62.
5. Ghanaati S, Booms P, Orlowska A, Kubesch A, Lorenz J, Rutkowski J, Landes C, Sader R, Kirkpatrick C, Choukroun J. Advanced platelet-rich fibrin: a new concept for cell-based tissue engineering by means of inflammatory cells. J Oral Implantol. 2014;40:679–89. doi:10.1563/aaid-joi-D-14-00138.
6. Nurden AT. Platelets, inflammation and tissue regeneration. Thromb Haemost. 2011:S13–33. doi:10.1160/THS10-11-0720.
7. Rivera FJ, Kazanis I, Ghevaert C, Aigner L. Beyond clotting: a role of platelets in cns repair? Front Cell Neurosci. 2015;9:511. doi:10.3389/fncel.2015.00511.
8. Schär MO, Diaz-Romero J, Kohl S, a Zumstein M, Nesic D. Platelet-rich concentrates differentially release growth factors and induce cell migration in vitro. Clin Orthop Relat Res. 2015;473:1635–43. doi:10.1007/s11999-015-4192-2.
9. Nami N, Feci L, Napoliello L, Giordano A, Lorenzini S, Galeazzi M, Rubegni P, Fimiani M. Crosstalk between platelets and PBMC: new evidence in wound healing. Platelets. 2016;27:143–8. doi:10.3109/09537104.2015.1048216.
10. Everts PM, Knape JT, Weibrich G, Schönberger JPAM, Hoffmann J, Overdevest EP, Box HAM, van Zundert A. Platelet-rich plasma and platelet gel: a review. J Extra Corpor Technol. 2006;38:174–87.
11. Jenne CN, Urrutia R, Kubes P. Platelets: bridging hemostasis, inflammation, and immunity. Int J Lab Hematol. 2013;35:254–61. doi:10.1111/ijlh.12084.
12. Soloviev DA, Hazen SL, Szpak D, Bledzka KM, Ballantyne CM, Plow EF, Pluskota E. Dual role of the leukocyte integrin M2 in angiogenesis. J Immunol. 2014;193:4712–21. doi:10.4049/jimmunol.1400202.
13. Ekström K, Omar O, Granéli C, Wang X, Vazirisani F, Thomsen P. Monocyte exosomes stimulate the osteogenic gene expression of mesenchymal stem cells. PLoS One. 2013;8:e75227. doi:10.1371/journal.pone.0075227.
14. Rybarczyk BJ, Lawrence SO, Simpson-Haidaris PJ. Matrix-fibrinogen enhances wound closure by increasing both cell proliferation and migration. Blood. 2003;102:4035–43. doi:10.1182/blood-2003-03-0822.
15. Choukroun J, Ghanaati S. Reduction of relative centrifugation force within injectable PRF-(Platelet-Rich-Fibrin) concentrates advances patients' own inflammatory cells, platelets and growth factors: First introduction of the low speed centrifugation concept (LSCC). Eur J Trauma Emerg Surg. 2017. doi:10.1007/s00068-017-0767-9.

16. M. Barbeck, A. Motta, C. Migliaresi, R. Sader, C.J. Kirkpatrick, S. Ghanaati. Heterogeneity of biomaterial-induced multinucleated giant cells: possible importance for the regeneration process? J Biomed Mater Res Part A 2016;104:413–8. doi:10.1002/jbm.a.35579.

17. Ozaki H, Hayashi H, Vinores SA, Moromizato Y, Campochiaro PA, Oshima K. Intravitreal sustained release of VEGF causes retinal neovascularization in rabbits and breakdown of the blood-retinal barrier in rabbits and primates. Exp Eye Res. 1997;64:505–17.

18. Brem H, Kodra A, Golinko MS, Entero H, Stojadinovic O, Wang VM, Sheahan CM, Weinberg AD, S.L.C. Woo, Ehrlich HP, Tomic-Canic M. Mechanism of sustained release of vascular endothelial growth factor in accelerating experimental diabetic healing. J Investig Dermatol. 2009;129:2275–87. doi:10.1038/jid.2009.26.

19. Lichtman MK, Otero-Vinas M, Falanga V. Transforming growth factor beta (TGF-β) isoforms in wound healing and fibrosis. Wound Repair Regen. 2016;24:215–22. doi:10.1111/wrr.12398.

20. Kim B-C, Kim HT, Park SH, Cha J-S, Yufit T, Kim S-J, Falanga V. Fibroblasts from chronic wounds show altered TGF-?-signaling and decreased TGF-? Type II Receptor expression. J Cell Physiol 2003;195:331–6. doi:10.1002/jcp.10301.

21. Alexander PB, Yuan L, Yang P, Sun T, Chen R, Xiang H, Chen J, Wu H, Radiloff DR, Wang X-F. EGF promotes mammalian cell growth by suppressing cellular senescence. Cell Res. 2015;25:135–8. doi:10.1038/cr.2014.141.

22. W. Fan, M. Yang, C. Zhang, R. Xue, W. Zhang, H. Qin. Effects of Choukroun's platelet-rich fibrin on human gingival fibroblasts proliferation, migration and type I collagen secretion. Zhonghua Kou Qiang Yi Xue Za Zhi. 2013;48:72–6.

23. M.A. Seeger, A.S. Paller. The roles of growth factors in keratinocyte migration. Adv Wound Care. 2015;4:213–24. doi:10.1089/wound.2014.0540.

24. Arda-Pirincci P, Bolkent S. The role of epidermal growth factor in prevention of oxidative injury and apoptosis induced by intestinal ischemia/reperfusion in rats. Acta Histochem. 2014;116:167–75. doi:10.1016/j.acthis.2013.07.005.

25. S. Forsberg, O. Rollman. Re-epithelialization from human skin explant cultures is promoted by ligand-activated HER3 receptor. doi:10.1016/j.jdermsci.2010.03.017.

26. Hong JP, Kim YW, Lee SK, Kim SH, Min KH. The effect of continuous release of recombinant human epidermal growth factor (rh-EGF) in chitosan film on full thickness excisional porcine wounds. Ann Plast Surg. 2008;61:457–62. doi:10.1097/SAP.0b013e31815bfeac.

27. Johnson NR, Wang Y. Coacervate delivery of HB-EGF accelerates healing of type 2 diabetic wounds. Wound Repair Regen. 2015;23:591–600. doi:10.1111/wrr.12319.

28. L. Heuch, J. Streak Gomersall. Effectiveness of offloading methods in preventing primary diabetic foot ulcers in adults with diabetes: a systematic review. JBI Database Syst Rev Implement Reports. 2016;14:236–65. doi:10.11124/JBISRIR-2016-003013.

29. B.D. Pence, J.A. Woods, Exercise, obesity, and cutaneous wound healing: evidence from rodent and human studies. Adv Wound Care. 2014;3:71–9. doi:10.1089/wound.2012.0377.

30. Tan KW, Chong SZ, F.H.S. Wong, Evrard M, S.M.-L. Tan, Keeble J, Kemeny DM, Ng LG, Abastado J-P, Angeli V. Neutrophils contribute to inflammatory lymphangiogenesis by increasing VEGF-A bioavailability and secreting VEGF-D. Blood. 2013;122:3666–77. doi:10.1182/blood-2012-11-466532.

31. Walsh TG, Metharom P, Berndt MC. The functional role of platelets in the regulation of angiogenesis. Platelets. 2015;26:199–211. doi:10.3109/09537104.2014.909022.

32. Barrientos S, Stojadinovic O, Golinko MS, Brem H, Tomic-Canic M, Perspective article. Growth factors and cytokines in wound healing. Wound Repair Regen. 2008;16:585–601. doi:10.1111/j.1524-475X.2008.00410.x.

33. Kolaczkowska E, Kubes P. Neutrophil recruitment and function in health and inflammation. Nat Rev Immunol. 2013;13:159–75. doi:10.1038/nri3399.

34. Gurtner G, Werner S, Barrandon Y, Longaker M. Wound repair and regeneration. Nature. 2008;453:314–21. doi:10.1038/nature07039.

35. Sahni A, Francis CW. Vascular endothelial growth factor binds to fibrinogen and fibrin and stimulates endothelial cell proliferation. Blood. 2000;96:3772–8.

36. Martino MM, Briquez PS, Ranga A, Lutolf MP, Hubbell JA. Heparin-binding domain of fibrin(ogen) binds growth factors and promotes tissue repair when incorporated within a synthetic matrix. Proc Natl Acad Sci USA. 2013;110:4563–8. doi:10.1073/pnas.1221602110.

37. M. a. Zumstein, A. Rumian, V. Lesbats, M. Schaer, P. Boileau. Increased vascularization during early healing after biologic augmentation in repair of chronic rotator cuff tears using autologous leukocyte- and platelet-rich fibrin (L-PRF): a prospective randomized controlled pilot trial. J Shoulder Elb Surg. 2014;23:3–12. doi:10.1016/j.jse.2013.08.017.

38. Visser LC, Arnoczky SP, Caballero O, Egerbacher M. Platelet-rich fibrin constructs elute higher concentrations of transforming growth factor-β1 and increase tendon cell proliferation over time when compared to blood clots: a comparative in vitro analysis. Vet Surg. 2010;39:811–7. doi:10.1111/j.1532-950X.2010.00739.x.

39. E. Kobayashi, L. Flückiger, M. Fujioka-Kobayashi, K. Sawada, A. Sculean, B. Schaller, R.J. Miron. Comparative release of growth factors from PRP, PRF, and advanced-PRF. Clin Oral Investig. 2016;20(9):2353–60. doi:10.1007/s00784-016-1719-1.

40. M. Fujioka-Kobayashi, R.J. Miron, M. Hernandez, U. Kandalam, Y. Zhang, J. Choukroun, Optimized platelet rich fibrin with the low speed concept: growth factor release, biocompatibility and cellular response. J Periodontol. 2017;88(1):112–21. doi:10.1902/jop.2016.160443.